ELECTRIC TAXIING

INVESTIGATION OF SYSTEM REQUIREMENTS AND DESIGN OF AN AXIAL FLUX PERMANENT MAGNET MACHINE FOR AN ELECTRIC TAXIING SYSTEM FOR A COMMERCIAL MIDSIZE AIRCRAFT

By FABIAN KELCH, B.Sc.

A Thesis Submitted to the School of Graduate Studies in Partial Fulfilment of the Requirements for the Degree Master of Applied Science

McMaster University
Hamilton, Ontario, Canada

McMaster University MASTER OF APPLIED SCIENCE (2015) Hamilton, Ontario (Mechanical Engineering)

TITLE: Investigation of System Requirements and Design of an Axial Flux Permanent Magnet Machine for an Electric Taxiing System for a Commercial Midsize Aircraft

AUTHOR: Fabian Kelch, B.Sc. (McMaster University)

SUPERVISOR: Professor Dr. Ali Emadi

NUMBER OF PAGES: xi, 123

Abstract

Driven by the gradually increasing electrification of the transportation industry, in particular the aviation sector, the future's electrified aircraft requires not only an improvement of the flight operation, but also an enhancement of the movement on ground. One very promising concept to improve the taxiing operation is the integration of an electric propulsion system into the aircraft's undercarriage, also called "Electric Taxiing". This yields a decrease of the overall fuel consumption, reduction of emissions, and improvement of aircraft maneuverability to help reducing operating times on ground. In this thesis, the performance requirements for an electric taxiing system are investigated by using self-recorded real-life aircraft taxiing drive cycle data. Based upon the system requirements, the powertrain for the electric propulsion system is sized for a commercial midsize aircraft to achieve a similar driving performance to conventional taxiing maneuvers. The sized powertrain, including the determined electric motor characteristics, is evaluated using a developed simulation model which allows testing the proposed electric taxiing system given the attained drive cycles. For the electric machine which is implemented into the wheel of the aircraft's main landing gear, an axial flux permanent magnet (AFPM) motor with segmented stator windings is selected due to its very compact structure while providing high torque capabilities. The AFPM motor is designed and evaluated by using analytical models and three-dimensional finite element analysis (3D FEA) to fulfill the specified motor characteristics required for the electric propulsion unit. Finally, suggestions for potential improvements and future work are discussed.

Acknowledgement

This research was undertaken, in part, thanks to funding from the Canada Excellence Research Chairs (CERC) Program.

I would like to thank my supervisor Dr. Ali Emadi for giving me the opportunity to pursue this research and making my graduate studies so enriching.

I am grateful to my colleagues and fellow researchers at the McMaster Automotive Resource Centre (MARC) for their comments and suggestions related to this work. Special thanks are due to Dr. Pierre Magne and Dr. Berker Bilgin for their valuable guidance and support throughout the project. I am also grateful to Dr. Yinye Yang, Dr. Nigel Schofield, Earl Fairall, Weisheng (James) Jiang and Dan Manolescu for their important assistance.

I would like to express my gratitude to my friends and fellow students at the McMaster Formula Hybrid Team/ McMaster Engineering EcoCAR 3 Team, in particular Cody Rhebergen, Joel Roeleveld, Ephrem Chemali, Kamran Arshad-Ali and William Long who made my graduate studies unforgettable.

I am indebted to my fellow student, project partner and close friend Maximilian Heinrich without whom this research and my time in Canada would not have been so successful and exciting.

My deepest gratitude goes to my parents, Anita and Thomas, as well as my sisters Alexandra, Annika and Alina, and my brother Maximilian, who gave me the encouragement, motivation and love I needed to accomplish this work. I am also very grateful to Christine and Christian who always supported me and helped to make my studies so enjoyable.

Table of Contents

List of Figures

List of Tables

Abbreviations

AFPM	Axial Flux Permanent Magnet (Motor)
APU	Auxiliary Power Unit
ESS	Energy Storage System
ETS	Electric Taxiing System
eTaxi	Electric Taxiing (System)
FEA	Finite Element Analysis
FG	Front Gear
FOD	Foreign Object Damage
LTO	Landing and Takeoff
MLG	Main Landing Gear
NG	Nose Gear
RFPM	Radial Flux Permanent Magnet (Motor)
RMS	Root Mean Square

1 INTRODUCTION TO ELECTRIC TAXIING

1.1 More Electric Aircraft

Air transportation developed fast over the past years and is expected to grow even further in the upcoming years. In the future, the aviation sector will have to face both economic and environmental challenges. About 2-3% of the worldwide total fossil fuels are consumed in the aviation sector which corresponds to 13 % of the total fossil fuel usage in transportation. Hence, the aerospace industry has a significant influence on the worldwide pollution - noise pollution and air pollution - impacting air quality and global climate [1], [2], [3].

In the era of climate change and limited resources, current and future regulations for the transportation industry target the increase of crafts efficiencies, decrease of fuel consumption, and the continuous reduction of emissions (greenhouse gases and noise) as well as improved reliability in order to ensure environmental sustainability. In this context, transportation electrification is becoming ever more important [4], [5], [6], [7].

In particular, new standards and guidelines have been introduced in regard to the air transportation sector by international organizations such as the "International Civil Aviation Organization" (ICAO) which set a goal in 2009 to improve the annual fuel efficiency by 2 % through the year 2050 and thereby reducing the global $C0_2$ emissions. This and even more ambitious goals are planned by the ICAO and other organizations for the upcoming years for aviation's contribution to climate change [8].

Within the past years tremendous progress has been made in the aircraft manufacturing industry in the efforts to move towards the direction of a more electric aircraft (MEA) following the ultimate goal of a fully electric aircraft,

which requires a replacement of existing power sources and devices aboard an aircraft by electrical systems. Aiming an improvement of the operational performance, new technologies and alternative power concepts have been investigated and developed that help reducing the fuel consumption and noise pollution as well as decreasing the overall costs including production, operation and maintenance costs [2], [4], [9], [10].

Today's investigations of aircraft efficiency improvements and emission reductions are not only focused on the flight operation, but also the on-ground operations of the aircraft gained more attention. On-ground movements such a as taxiing and aircraft towing have a significant potential for reducing fuel consumption and emissions [2], [3], [11], [12].

This thesis aims an improvement of the taxiing operation by using an electric taxiing system that helps reducing the overall fuel consumption and emissions including greenhouse gases and noise.

On-Ground Operation "Taxiing"

The process that is being investigated in this study is the on-ground movement of an aircraft between the terminal and the runway. This movement is also known as "Taxiing" and is performed on the taxiways on an airport.

Taxiing can be described by subdividing the overall landing and takeoff (LTO) cycle into different phases. Following the definitions of the Internal Civil Aviation Organization (ICAO), every LTO cycle for a commercial jet engine aircraft can be classified into the following different operation modes [1].

- Takeoff
- Climb
- Approach
- Taxiing

Taxiing can further be classified into taxi-out and taxi-in phases, depending on whether the aircraft is moving from the terminal to the runway or vice versa. The term taxi-out is used when the aircraft is leaving the airport. Prior to the taxi-out mode the main engines need to be started in order to ensure the warm-up of the jet engines. This warm-up process is required for bringing the propulsion system including the oil system up to temperature before running at high power. The engine warm-up usually takes about 3-5 minutes [13]. The taxi-out process starts with a pushback that is realized by an external tractor that pushes the aircraft onto the respective taxiway. After decoupling the tractor, the aircraft is ready to begin the self-propelled taxiing process towards the runway. The taxi-out mode is completed when the takeoff brakes are released and the jet engines are switched from idle to full throttle, initiating the takeoff.

In the takeoff phase the aircraft accelerates up to high speed until the aircraft gets airborne during the liftoff, followed by a climb phase in which a required flight height of 3000 feet (0.91 km) is reached which indicates the beginning of the flight phase [1].

The arrival at the destination airport begins with an approach phase which indicates the descending from 3000 feet flight height down to the touchdown and rolling out on the runway. At the end of the rollout when the aircraft is decelerated down to respective on-ground speed the taxi-in mode is initiated maneuvering the aircraft to the final parking position at the terminal where the aircraft comes to a stop and the engines are shut off.

Since neither the flight phase nor the climb or approach phase are considered in this thesis it is solely focused on the taxiing process, i.e. the aircraft's motion between the terminal and the runaway including taxi-in and taxi-out. Figure 1-1 illustrates the different phases of a typical LTO cycle.

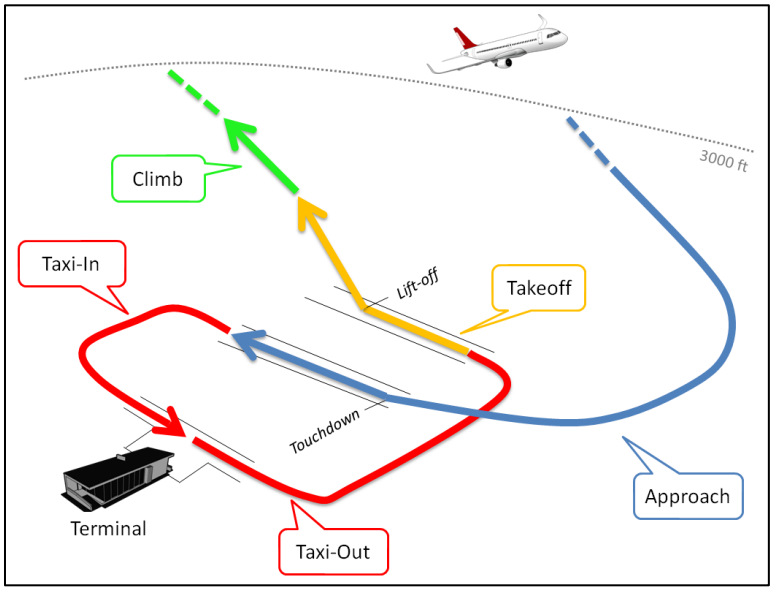

Figure 1-1 – Landing and Takeoff (LTO) Cycle

1.1.1 Conventional Taxiing and its Drawbacks

The propulsion of a conventional commercial jet engine aircraft for the travel between the terminal and the runway is realized by the jet engines since no additional on-board technology or propulsion system is available aboard the aircraft performing to perform the on-ground movement. Hence, the aircraft is required to use idle thrust of the engines which is very fuel inefficient in this condition resulting in high fuel waste and emission as well as noise production. The reason for this is that the engines are mainly sized for the flight phase rather than for powering the aircraft on-ground. During the most demanding phase, the takeoff mode, 100 % of the full thrust is required, whereas while taxiing and ground idle the engines are operated with merely 7 % of the full thrust [3]. Only if accelerations from standstill are required on the taxiway the engines might be spooled up for a short time. Thus, during the taxiing procedure between runway and terminal an extremely high amount of fuel is burned very inefficiently. Due to an incomplete combustion at idle the jet engines generate large amounts of carbon

monoxide (CO). In terms of nitrogen oxide (NOx) emissions, the ground operations contribute a large percentage to the overall emissions. For instance, at the London Heathrow airport in 2002 about 56 % were induced during on-ground movements [3]. Optimization strategies such as driving one engine only, aiming an improvement of the taxiing process, exist. However, since at least one main engine has to be started, the conventional propulsion during taxiing always suffers from high fuel consumption and pollution. This impacts the performance of short-haul aircrafts in particular, where the taxiing operation is relatively long compared to the flight mission. Additionally, the use of the friction brakes for braking procedures during on-ground movements causes unnecessary brake wear [3].

Beside these problems conventional taxiing suffers from further drawbacks such as logistical cost and time. As described previously, the taxi-out phase begins with a pushback from the gate onto the respective taxiway which cannot be realized by using the main engines itself. Nowadays, this is completed by external towing vehicles such as diesel-powered tractors causing crucial time delays due to coupling and decoupling procedures. Furthermore, this leads to high congestion in the airport area. Besides, the jet engines are running already before and during the pushback to ensure the required warm-up time so that they can be used directly after completion of the pushback. Hence, this warm-up time contributes to the overall taxiing duration as well.

In summary, the ineffective use of the main engines for propulsion during taxiing suffers from major problems that need to be overcome in order to improve the on-ground movements in the airport area. Thus, the objective is the creation of a more efficient solution by implementing an additional electric propulsion system that allows driving the aircraft without running the engines.

1.2 Electric Taxiing Concepts

More and more research has been done aiming a development and implementation of new technologies in order to improve the taxiing process. Nowadays, many companies and institutions are heavily working on various concepts for more electrified taxiing and aircraft towing. The idea behind these advanced solutions is the creation of a more efficient system for taxiing yielding a reduction of the overall fuel consumption, pollution and operation time for on-ground movements. In order to achieve these goals the highest degree of electrification possible is aimed for propulsion during on-ground movements. The objective is a taxiing process without running the jet engines at all. Various concepts are possible following the two potential approaches:

- External systems (off-board systems)
- On-board systems

Integrated systems aboard the aircraft, i.e. on-board drive units, are generally advantageous since they offer a high degree of flexibility since no external systems are required for the on-ground movement. However, such solutions require a retrofitting or redesign of the aircraft which can be avoided when invloving external systems such as tugs or other towing concepts. Moreover, on-board systems have to be carried during the flight phase, contributing to the fuel consumption during the flight phase, which has to be considered as well. Thus, electrified taxiing systems have to be selected carefully based on the respective requirements and available boundary conditions.

In this section, the most advanced technologies developed in the past years that focus on the electrification of on-ground movements in airport areas are introduced and their advantages and drawbacks are discussed.

1.2.1 External Systems (Off-Board Systems)

The most obvious solution of maneuvering the aircraft on-ground with an external system is the use of towing vehicles similar to the conventional diesel-tractors that perform the pushback during today's taxiing procedure. After coupling with the front gear the tractor would not only complete the pushback but also tow the aircraft along the taxiways. An internal combustion engine driven tractor completing the entire on-ground movement of the aircraft would make the taxiing process distinctly more efficient than the conventional solution. Preventing the operation of the jet engines at idle would allow reducing the fuel consumption as well as pollution and noise. More advanced solutions include electrified external towing systems such as hybrid-electric or fully electric tractors. Companies have been working heavily on electrified external systems with sufficient power in order to achieve similar driving performances as jet engine propelled maneuvers, aiming a more efficient on-ground movement as well as time savings in the overall LTO cycle.

One of these systems is "*TaxiBot"*, a semi-robotic towing system developed by Israel Aerospace Industries (IAI) along with its partner TLD in cooperation Lufthansa LEOS, a subsidiary of the Lufthansa Group, and the aircraft manufacturers Airbus and Boeing (Figure 1-2). This solution which is a hybrid-electric tug almost prevents the use of the main engines during the entire taxiing process by moving the airplane along the taxiways close to the runway, allowing taxiing speeds of up to 23 knots (42.6 km/h). After warming up the jet engines and prior to takeoff the system needs to be decoupled from the aircraft. Although a driver is located in the tractor for completion of the pushback, the system can be controlled by the pilot sitting in the cockpit. The system provides the pilot with similar handling characteristics to conventional taxiing, which is ensured by a special cradle that holds the aircraft's nose gear wheel assembly. Different to conventional towbar tractors this method is able to sustain the high

loads generated during high taxiing speeds. The all-wheel-drive system leads to improved traction which is important when moving on wet or icy surfaces. The TaxiBot was developed in two different models. The "Narrow-Body" TaxiBot is suitable for single-aisle aircrafts such as Airbus models A318 to A321 and Boeing B737 to B757, whereas the "Wide-Body" version is designed for twin-aisle aircrafts such as A330 to A380 and B767 to B747 models [14], [15].

Figure 1-2 – TaxiBot [16]

The "*Hybrid eSchlepper"* from Lufthansa LEOS in partnership with Kalmar Motor AB from Sweden is an all-wheel drive hybrid electric vehicle which primarily will be used for long distances such as hangar towing and repositioning operations (Figure 1-3). Different to current towbar based diesel powered tugs the eSchlepper aims the reduction of fuel burn and pollution by running purely electric. The integrated diesel-engine functions solely as a range extender by charging the on-board lithium-ion batteries if needed. As the only product in its power class, the system is able to move heavy long-haul aircrafts with a maximum take-off weight of up to 600 tonnes over distances of up to seven kilometers [17].

Figure 1-3 – Hybrid eSchlepper [17]

Another ground vehicle, called *"Taxiing Vehicle"*, is a concept introduced by Airbus S.A.S. that allows towing an aircraft without any human intervention (Figure 1-4). The taxiing vehicle aims performing the taxi-out as well as the taxi-in maneuver of the aircraft. When the aircraft comes to a short stop on the tarmac after decelerating during touchdown, the system is coupled with the aircraft's nose gear. The taxi-in procedure can then be initiated. Different steering strategies of the towing vehicle could be realized such as integrated tracks with electromagnetic currents that flow through the runway and taxiways or wireless high power solutions through which the aircraft could be controlled acting as a conduit [17].

Figure 1-4 – Airbus Taxiing Vehicle [18]

Considering the fact that off-board towing systems such as “TaxiBot”, “Hybrid eSchlepper” can be implemented without any modifications of the aircraft or the airport infrastructure itself, these concepts represent suitable alternative solutions for today’s jet engine powered on-ground movements. These systems can help the aviation industry improving the overall flight mission in order to meet defined standards and guidelines regarding fuel consumption and emission targets. Particularly with regard to short-term improvements in the next years, off-ground electric taxiing systems are a suitable solution.

More advanced concepts without human intervention, such as the Taxiing Vehicle by Airbus, require expansions or modifications of existing airports. These may include additional connections or data transfer (e.g. wireless solutions or integrated tracks in the runway) to realize driverless steering and controlling strategies. Under these circumstances, driverless solutions might be more suitable for future airport developments and long-term considerations.

Overall, each of the introduced towing systems has great potential in terms of on-ground propulsion improvements. However, additional vehicles operating in the airport area lead to further congestion and time delays due to coupling and decoupling procedures. Since time is a major influence factor in the public transportation sector, in particular in the aviation industry, electric on-board propulsion systems preventing the needed assistance by further towing vehicles, yielding a high degree of flexibility, are gaining more importance.

1.2.2 On-Board Systems

An advanced concept to improve the taxiing operation is the integration of electric motors into the rims of the aircraft’s main landing or front gear wheels. These motors can be powered by the aircrafts Auxiliary Power Unit (APU) and/ or any other electrical sources within the aircraft. The general idea behind such on-board systems is the improved flexibility due to the gained independence on

external towing systems. This leads to a reduction of the on-ground operation time compared to off-board taxiing concepts. Solutions with an electrically powered landing gear for taxiing procedures aim a reduction, or complete avoidance if possible, of external ground vehicles and ground personnel. In general, electrically powered on-board systems are also known as “Electric Taxiing”, “eTaxi” or “Green Taxiing”.

As described previously, the system can be powered by various power supplies such as batteries, ultra-capacitors, fuel cells, fly wheels or any other energy storage systems which needs to be located on-board as well. An alternative method to additional energy storage systems is the use of the APU which is used for on-board electronics (air conditioning, lights etc.) during the terminal operation in conventional jet engine aircrafts. If the APU could be realized as power source for on-ground movements without major modifications of the device itself, it would be a favourable solution because other energy storage systems causing additional weight could be eliminated.

For on-board taxiing systems, the electrical drive unit must be integrated into the undercarriage. Here, two locations are possible options: the main landing gear (MLG) in the rear of the aircraft or the nose gear (NG), also called front gear (FG), in the front of the aircraft. In general, the integration into the front gear is advantageous in terms of space limitations and simplicity [11]. For instance, reasons for that are the absence of interference with the braking system located in the MLG and shorter cable runs leading to an easier and quicker installation. Besides, a lighter system can be created since only one drive unit is added to one wheel assembly in the front gear. On the other hand, main landing gear systems are favoured because they provide optimal traction since the MLG sustains about 90 % of the aircraft weight. However, adding another system to the MLG leads to mechanical complexity. Major challenges are the added weight and potential conflicts with the brake system in terms of heat dissipation and other influences.

Several concepts with different configurations have been developed in recent years. The most advanced solutions and prototypes are discussed in the following.

1.2.2.1 Existing Electric Taxiing (On-Board) Systems

The first electric taxiing system developed and implemented in an aircraft was developed by the UK based company *WheelTug*. The system is integrated into the front gear of the aircraft (Figure 1-5). The two twin induction machines from the company Chorus Motors are connected to a planetary gear system and powered by the APU. The company expects a time reduction of around 20 min and up to $2,000 per flight cycle by using the electric drive system leading to over $3 million of cost savings per aircraft per year. The crucial time savings are not only realized during taxiing itself, but also during the terminal operation. By moving the aircraft with stopped engines the aircraft is able to park parallel to the terminal allowing the use of both the back and front doors for boarding and deplaning passengers. Due to safety reasons this is not possible with running jet engines. After a first proof of concept test in 2005 and ground tests on snow and slush in 2010, the improved in-wheel motor design was successfully tested at Prague airport in 2012 using a Germania 737-700. Influenced by these feasibility demonstrations other competitors including Delos Aerospace, Messier-Bugatti-Dowty and the German Aerospace Center started the development of their own electrified taxiing system. The beginning of a series production of the WheelTug propulsion system for commercial aircrafts is planned for 2016 [11], [19].

Delos Aerospace announced the invention of a fully electric in-wheel electric motor system for on-ground movements in 2007. In this concept, the conventional friction disc technology is replaced by axial flux disc motors/ generators offering increased braking and maneuvering capabilities. A great advantage of such a technology is the elimination of the high heat dissipation

created by the friction-based brakes. The company foresees reduced costs of 3.8 to 4.2 million USD per year per commercial aircraft [20], [21].

Figure 1-5 – WheelTug [19]

Another electric taxiing system has been developed and built by the *German Aerospace Center* (DLR) in cooperation with Airbus and Lufthansa Technik. The prototype of their nose gear system which houses two in-wheel hub motors with integrated two-stage planetary gear reduction has been tested and demonstrated in a passenger aircraft Airbus A320 in 2011 in Hamburg, Germany. A peak torque of 450 Nm is delivered by the two PM synchronous motors that are each connected to a 12:1 planetary gear reduction. A nose gear system with a redesigned wheel rim was selected in order to fit the electric motors including the integrated planetary gear. The DLR green taxiing propulsion unit is powered by a hydrogen fuel cell system. The system is designed for taxiing speeds of up to 25km/h. A clutch mechanism is foreseen to actuate with different gear ratios. Enabling the available direct drive mode allows spinning up the wheels prior to touchdown in order to reduce tire wear. Although the total output power of the drive unit is relatively low with 50 kW, the system provides 44 tons of potential

kerosene savings per day for an Airbus A320 leading to a reduction in emissions of up to 17 to 19 % for on-ground movements [22], [23].

In 2008, the "*Green Taxiing"* was launched by Messier-Bugatti-Dowty (former Messier-Bugatti), a subsidiary of Safran, aiming a series production in 2016 of the developed prototype of an electric taxiing system implemented into the MLG. The company targets the installation on new and retrofitted aircrafts such as Airbus A320 and Boeing 737 families. The prototype was developed within a project called "CleanSky Joint Technology Initiative" in which Safran, Airbus, the German Aerospace Center and the University of Nottingham participated. The feasibility of implementing the proposed direct-drive in-wheel actuator unit was presented in [24]. In this study, different motor variants have been designed by GE in partnership with the University of Nottingham for different possible envelopes within the rim of an aircraft of the size of an Airbus A320. A thermal analysis for potential direct-drive in-wheel PM machines was conducted in [25].

In 2011, *EGTS International*, a joint venture between Honeywell Aerospace and Safran was founded in order to develop a new "Electric Green Taxiing System" (EGTS) for new and existing aircrafts. The propulsion system which drives the aircraft powered by the APU generator is implemented into the MLG. Each of the two MLG wheel assemblies houses an electric motor coupled to a gear reduction. The system can be switched on and controlled by the pilot over a user interface that is located in the cockpit. The Wheel Actuator Controller Unit (WACU), integrated into the aircraft fuselage, converts the current coming from the APU generator powering the in-wheel motors based on the pilot's commands in the cockpit. The system was officially demonstrated in 2013. Here, an Airbus A320, equipped with the electric propulsion system, landed at the Paris Air Show and completed several maneuvers with the engine stopped, including turning and reverse taxiing. The physical implementation of the drive unit located

in the main landing gear is shown in Figure 1-6. By using the EGTS, the pushback time can be reduced by 60 %. The system also offers carbon emission reductions of up to 75 % and up to 50 % reduction in NOx emissions during ground operations [11], [26].

Figure 1-6 – EGTS Implementation into MLG [27]

Lastly, a non-engine taxiing systems has been developed by *L-3 Communications* in their Magnet Motor division in partnership with Lufthansa German Airlines, Lufthansa Technik and Fraport. The green taxiing system has been installed into an Airbus A320 in cooperation with Lufthansa German Airlines. Containing four separate drive units with electric in-hub PM synchronous motors from "Magnet Motor", the system has been implemented into the main landing gear of this midsize aircraft. The propulsion system is powered by the aircraft APU. In 2011, it was successfully tested, including gate pushbacks, ramp maneuvers, forward and reverse taxiing at different speeds on an Airbus

A320 in Frankfurt, Germany. Due to space limitations within the initial design, the carbon brakes in the MLG wheels had to be removed for the demonstration in Frankfurt. However, by testing various duty cycles the developers were able to gather important data for future motor designs [11], [28].

1.2.2.2 Summary

In summary, all of the presented on-board taxiing systems target short-to medium-haul aircrafts where the taxiing operation has a greater percentage of the overall flight cycle than long-haul aircrafts. This promises major improvements such as fuel and cost savings although a complex system with extra weight is added to the aircraft.

The EGTS by Honeywell and Safran in particular is a very promising concept since it provides the highest taxiing speeds among the existing systems with about 37 km/h (20 knots) whereas other systems developed by L3 Communications or the German Aerospace Center aim on-ground velocities of 30 km/h or 25 km/h, respectively [19], [22], [28]. In comparison, the WheelTug front gear propulsion unit allows only taxiing speeds between 7 and 10 knots (13-18.5 km/h) leading to performance losses in terms of maximum available on-ground speeds.

Besides, MLG systems such as EGTS and GreenTaxi by L3 Communications are advantageous over front gear systems since higher traction can be transmitted to the ground. Front gear systems such as WheelTug suffer from less performance on bad road conditions, and are therefore not suitable for degraded environmental conditions (for instance wet or icy taxiways). The aft center of gravity of the aircraft would not allow a system integrated into the nose gear to ensure enough traction. Here, MLG systems stand out due to agile taxiing in any weather or runway condition [22], [29].

Although less advanced systems in terms of top speeds and transmittable propulsion forces like WheelTug are not able to provide similar driving performances as conventional taxi procedures, they are rather a very cost effective alternative which still enable tremendous time savings compared to today's tug assisted on-ground operations [29].

1.2.3 Advantages and Drawbacks of Electric Taxiing Systems

Both off-ground and on-ground electric taxiing systems target a replacement of the conventional method of propelling the aircraft by the inefficient use of the jet engines. If implemented in existing, retrofitted or new aircrafts or airports, respectively, both approaches and their respective technologies lead to major improvements of on-ground movements and the overall LTO cycle. Beside cost reductions due to reduced fuel consumptions, a much healthier and safer environment can be expected.

Summarizing, electrifying the taxi operation between terminal and runway including the pushback and the movement along the taxiways on the airport delivers the following advantages [30]:

- Reduced fuel consumption (reduction of up to 4 % of total block fuel consumption for short-haul aircrafts, leading to yearly cost savings of around 200,000 USD of fuel per aircraft)
- Reduced pollution, i.e. greenhouse gas emissions (reduction of up to 75% in $C0_2$ and up to 50% in NOx emissions)
- Reduced noise
- Reduced foreign object damage (FOD)
- Reduced engine maintenance
- Reduced friction brake wear

- Improved on-ground safety for ground personnel (no engines running)

1.2.3.1 Comparison of On-Board Systems and External Systems

As described previously, integrated electric power units in either the MLG or the FG wheel assembly are challenging due to space limitations and the interference with other structural components in the undercarriage. Besides, by adding a complex drive assembly the total weight of the aircraft will be increased influencing the fuel consumption during flight phase. This has to be considered when developing such a system.

On the other hand, electrically powered landing gear systems are advantageous over off-board systems due to their high degree of flexibility since no external vehicles of any kind are needed anymore for the taxiing procedure. With an integrated system, the airplane is able to maneuver between terminal and runway independently, giving the pilot the complete control from inside the cockpit during taxiing mode.

The selection of the respective technology is influenced by the needs of the aircraft manufacturer, the customer (i.e. passenger), the airport operator and public transportation regulations. Thus, the optimal solution has to be chosen carefully based on the given requirements and restrictions.

Summarizing, on-board propulsion systems provide the following advantages over tug-based off-board concepts [28], [30]:

- Reduced taxiing times (elimination of coupling and decoupling with towing vehicles)
- Reduced tug capital and overall cost of operation
- Reduced congestion (less ground vehicles)

- Increased performance (high flexibility and maneuverability)
- Less ground personnel needed (e.g. tug drivers)
- Reduced tire wear (spinning of wheels prior to touchdown)
- Use of regenerative braking (leading to energy savings and reduced friction brake wear)
- No modification to airport infrastructure required

Considering the presented advantages, electric taxiing systems implemented aboard the aircraft can be assumed to be even more advanced than their external opponents. However, integrating an additional complex system to the aircraft causes further drawbacks as follows:

- Increased weight of aircraft (impact on fuel consumption during flight phase)
- Modification of aircraft required (e.g. undercarriage, power supply)
- High complexity and potential interference with other sub-systems, in particular in MLG with neighboring friction brakes (e.g. challenges with heat removal)

1.3 Objective

In this thesis an electric taxiing system is developed targeting an improvement of the taxiing process in terms of operation cost, time and environmental pollution. Based on the advantages presented previously, an on-board propulsion system is selected to prevent any external assistance causing potential time delays and logistical costs. In particular, an implementation into the main landing gear is chosen. In order to achieve the maximum possible time savings during the entire LTO cycle a similar driving behaviour as conventional taxiing is aimed, realizing the least losses and limitations in taxiing performance.

This study investigates the system requirements that are needed for achieving these performance goals. The needed powertrain including all system components is sized for a state-of-the-art commercial single-aisle midsize aircraft. Self-recorded real-time taxiing data including taxi-out as well as taxi-in drive cycles is analyzed and used for testing the developed system in comparison with conventional on-ground movements. Based on the interaction between the wheels and the tarmac of the aircraft a simulation model is developed and simulated with various drive cycles in order to evaluate and characterize system requirements such as power and energy rating of the traction system for different taxiing scenarios. This allows determining the required powertrain component specifications for electric motors, potential gear boxes, energy storage system and power electronics for given performance targets. The energy used to power the aircraft while taxiing is assumed to be delivered by a unique bidirectional energy source. This can be the combination of the aircraft's APU, a battery, an ultra-capacitor, a fuel cell and/ or other energy storage devices, providing the necessary power and energy during on-ground propulsion. However, the exact nature of the energy storage system is not further specified as this thesis focuses mainly on the electric machine design. The assumptions and powertrain component specifications implemented into the simulation model, particularly the electric motor parameters, are confirmed by the simulation results.

On the basis of the determined motor specifications, the electric machine is designed to show the feasibility of the proposed propulsion system. Due to the size constraints in the wheel of the main landing gear an axial flux permanent magnet (AFPM) machine with yokeless and segmented armature is selected, offering high compactness while providing high torque and power capabilities. According to the given space limitations and restrictions in the undercarriage, the electric machine is designed by using analytical models and three-dimensional finite element analysis (3D FEA).

In this thesis, the following chapters, representing the development and design process of the AFPM motor, will be covered. Firstly, the performance requirements of an electrified taxiing system are investigated, resulting in the definition of required motor specifications (section 2). Secondly, the fundamentals of AFPM machines are presented followed by the selection of the final motor topology (section 3). Subsequently, the design procedure and the analysis of the proposed AFPM motor including analytical models and 3D FEA are shown (section 4). Lastly, conclusions and suggestions for improvements and future work are discussed (section 5).

2 INVESTIGATION OF ELECTRIC TAXIING SYSTEM REQUIREMENTS

In this section the system requirements for an electric taxiing system will be investigated. This is done in different stages. At first, taxiing performance parameters are determined and analysed. Conventional jet engine propelled taxiing procedures are used as a benchmark when defining system performance requirements. According to these requirements a system and the respective powertrain components are developed and sized. Finally, the system is tested and analyzed by using a developed simulation model. Thus, the analysis process is structured into the following steps:

- Taxiing performance analysis
- Definition of system requirements
- Electric taxiing system sizing
- Modeling and evaluation

The investigation of system requirements for the electric taxiing system was conducted in cooperation with Mr. Maximilian Heinrich within a shared

research project at the McMaster Automotive Resource Centre which also can be found in [31].

2.1 Taxiing Performance Analysis

2.1.1 Drive Cycle Data Acquisition

Conventional taxiing performance data is required for a realistic analysis of the on-ground movement during taxi mode. Drive cycles, i.e. velocity over time profiles, have been self-recorded by the use of GPS devices for multiple commercial taxiing operations, including takeoff (taxi-out) as well as landing (taxi-in) cycles. These drive speed profiles have been logged across various international airports, in Europe and North America in particular, from those 20 very accurate ones, in total 10 taxi-out and 10 taxi-in cycles, are selected for this study as presented in the following. These drive cycles can be used as a benchmark when defining the performance requirements of the developed eTaxi system in comparison with conventional driving behavior. The available drive cycles, i.e. the locations of the respective airports, are listed in Table 2-1.

2.1.2 Drive Cycle Evaluation

An analysis of the obtained GPS data shows that the recorded taxiing speed profiles provide sufficient accuracy for approximating and evaluating real taxiing behavior in order to investigate electric taxiing system requirements.

Four examples of the chosen drive cycles representing two different taxi-out and two taxi-in cycles are illustrated in Figures 2-1 to 2-8. Figures 2-1 to 2-4 show the taxi-out drive cycles along with their GPS tracking from a satellite perspective recorded on Berlin Tegel Airport in Germany and the Hamilton International Airport in Canada, whereas the two taxi-in cycles recorded on Dallas/ Fort Worth International Airport in the US and on Munich Airport in Germany can be seen in Figures 2-5 to 2-8.

Taxi-out procedures are characterized by a pushback phase at the beginning initializing the taxiing process from the initial parking position. Thus, the acceleration with low speeds present in the speed profile in reality is performed in reverse. In the Hamilton drive cycle, which represents a typical takeoff taxiing speed profile, the pushback can be seen between 40s and 120s (Figure 2-3). Since conventionally this pushback is conducted by a tug, a waiting time can be noticed until a time of 245s which is required for decoupling and removing the towing vehicle. At this point the actual jet engine powered on-ground movement on the taxiways begins targeting the airport's runway. Another short stop can be seen in the Hamilton cycle after a time of 460s indicating another aircraft passing or other commands given by the tower obligating the pilot to wait for a respective time slot until the aircraft can continue the taxiing process in order to leave the airport. Maximum speeds of almost 55 km/h are reached during the entire operation. Since this study focuses on the taxiing process rather than the entire LTO cycle, the takeoff as well as its prior high acceleration are not shown in the taxi-out profile. This needs to be realized by the jet engines and does not belong to the taxiing process. In the Hamilton example this occurs beyond a time of 750s where an immediate transition from taxiing to takeoff mode was experienced. The position where the GPS recording was started or stopped during the drive cycle, respectively, is indicated in the respective satellite picture with a yellow star.

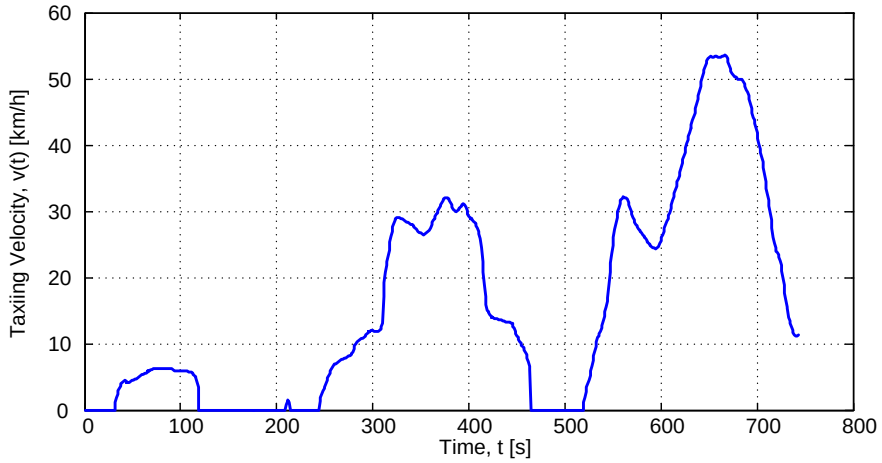

Figure 2-1 – Hamilton (YHM) – Taxi-Out

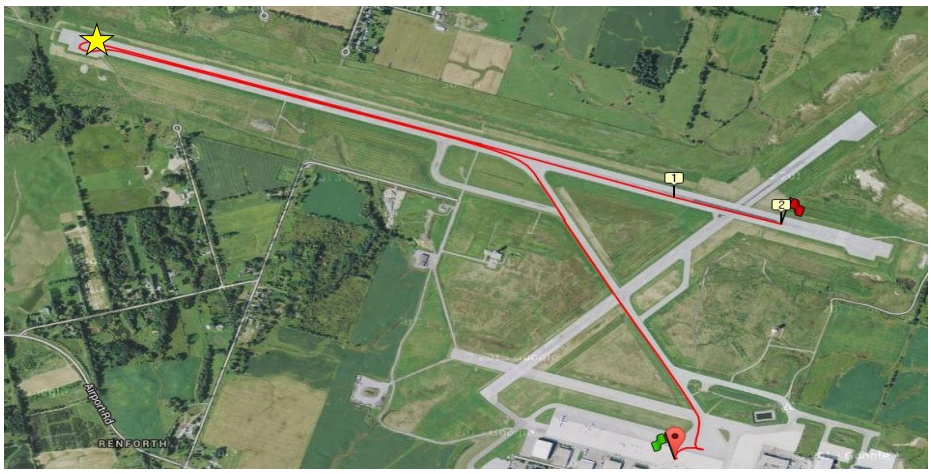

Figure 2-2 – Hamilton (YHM) – Takeoff (GPS Tracking)

The Berlin drive cycle shows a similar taxi-out behavior (Figure 2-3). However, besides one stop after the initial pushback, the aircraft taxis to the runway without any further stops. In this case, the pilot is able to proceed unrestricted to the runway initiating the takeoff process unaffected by other aircrafts or disruptions.

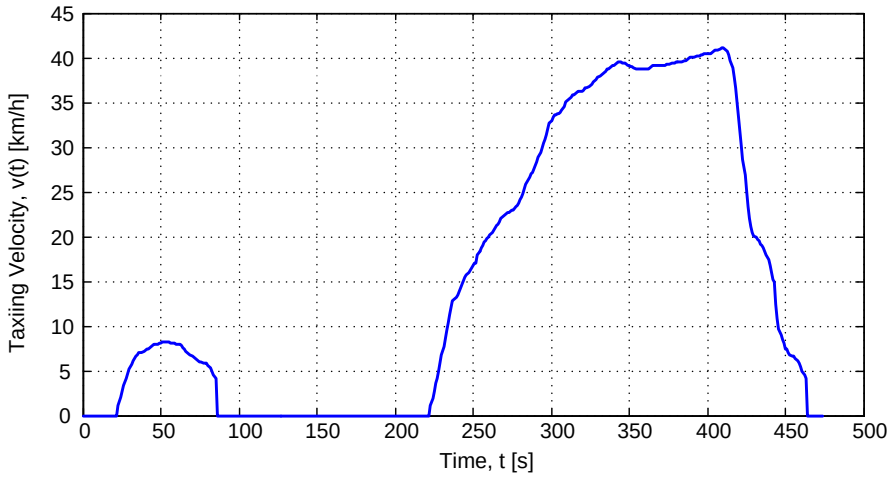

Figure 2-3 – Berlin Tegel (TXL) – Taxi-Out

Figure 2-4 – Berlin Tegel (TXL) – Taxi-Out (GPS Tracking)

Two different taxi-in maneuvers are shown in Figures 2-5 to 2-8. The recording is started after completing the touchdown and decelerating down to taxiing speeds.

A typical landing drive cycle was recorded on Munich Airport (Figure 2-5). It can be seen that there are no high accelerations and no stops between the roll out and the arrival at the final parking position, leading to a relatively smooth

taxiing cycle. On the other hand, the Dallas/ Fortworth speed profile shows several stops potentially caused by interfering airplanes on the tarmac. The diagrams also show that maximum speeds of over 60 km/h are reached during taxiing.

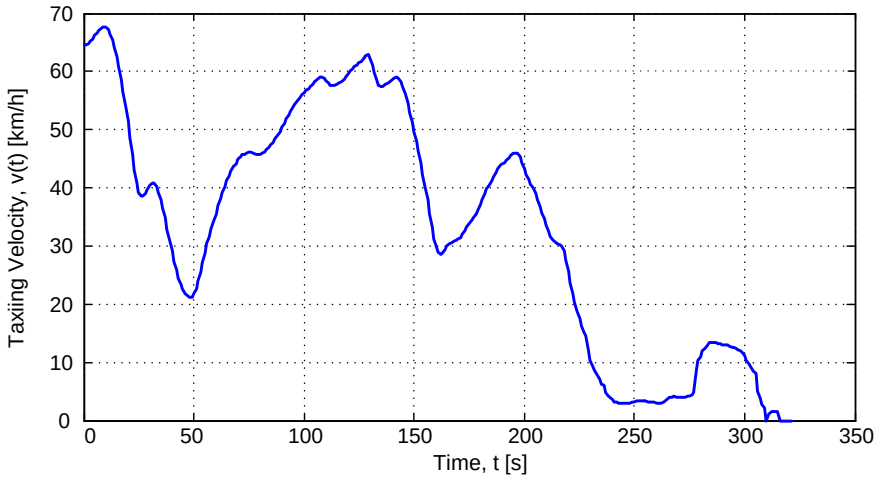

Figure 2-5 – Munich (MUC) – Taxi-In

Figure 2-6 – Munich (MUC) – Taxi-In (GPS Tracking)

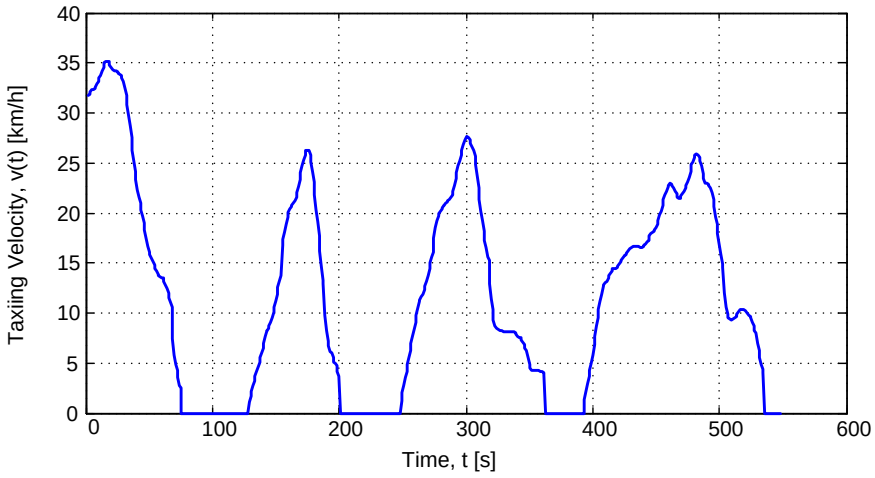

Figure 2-7 – Dallas/ Fort Worth (DFW) – Taxi-In

Figure 2-8 – Dallas/ Fort Worth (DFW) – Taxi-In

In general, taxi-out procedures are more demanding due to potential stops when moving towards the runway, high and frequent accelerations and longer operating times. Landing cycles are commonly shorter because an immediate movement back to the final parking position at the gate after the roll out is often unaffected by other interferences. However, it was found that the taxiing process can vary a lot depending on influencing factors such as operation time, location

and traffic conditions on the airport, which makes the taxiing process unpredictable.

The available drive cycles (Table 2-1) represent an appropriate compilation of different taxi speed profiles that can be used to conduct a detailed performance analysis of conventional taxiing. Performance parameters can be directly derived from these profiles. This allows the definition of component specifications when sizing the electric taxiing system.

Table 2-1 – Available Drive Cycles

Airports for Taxi-Out Drive Cycles	**Airports for Landing Drive Cycles**
Hamilton (YHM), Canada	Munich (MUC), Germany
Frankfurt Main (FRA), Germany	Frankfurt Main (FRA), Germany (2 different drive cycles)
Berlin Tegel (TXL), Germany (2 different drive cycles)	Berlin-Tegel (TXL), Germany
London Heathrow (LHR), UK (2 different drive cycles)	London Heathrow (LHR), UK
Toronto Pearson (YYZ), Canada (2 different drive cycles)	Toronto Pearson (YYZ), Canada
Dallas/Fort Worth (DFW), USA (2 different cycles)	Dallas/Fort Worth (DFW), USA (2 different drive cycles)
	Calgary (YYC), Canada
	Vancouver (YVR), Canada

2.1.3 Kinematic Drive Cycle Analysis

Since a similar on-ground performance to conventional taxiing is targeted, the recorded drive cycles are used to determine system parameters that the sized system needs to meet during the taxiing process. From the speed profiles the following parameters can be derived:

- Total Taxiing distance (d_{total})
- Maximum taxiing speed (v_{max})
- Maximum acceleration (a_{max})
- Maximum traction force ($F_{tr.max}$)
- Maximum traction/ propulsion power ($P_{tr.max}$)

These performance parameters are determined for each of the available drive cycles by the use of a developed Matlab/Simulink simulation model which is described later in section 2.4.1.

Whereas solely kinematic parameters such as distance, speed and acceleration can be determined directly from the drive cycles, the traction force F_{tr} and the traction power P_{tr} are dependent on the design of the taxiing system. In particular, these parameters are influenced by the aircraft's inertial mass m_i (eqn. (14)) which also changes with varying performance parameters, making the system sizing an iterative process. The calculation of traction force and traction power in detail is presented in section 2.3.5.2.

The obtained performance parameters based on the used real-time taxiing data for taxi-out as well as taxi-in operations are summarized in Table 2-2. These parameters represent the peak values among the different speed profiles during conventional taxiing. These peak values are important when sizing the electric taxiing system. Further results of the kinematic drive cycle analysis, i.e. the performance parameters for each individual drive cycle are listed in the Appendix (Tables A-1 and A-2).

Table 2-2 – Kinematic Drive Cycle Analysis Results

Parameter	**Taxi-Out**	**Taxi-In**
Max. Taxiing Velocity (v_{max})	61.8 km/h (Dallas)	67.6 km/h (Munich)
Max. Acceleration (a_{max})	1.14 m/s² (Hamilton)	1.08 m/s² (Munich)
Max. Traction Force $(F_{tr.max})$	104 kN (Hamilton)	98.84 kN (Munich)
Max. Traction Power $(P_{tr.max})$	584.5 kW (Frankfurt)	499.2 kW (Frankfurt)

2.2 Definition of System Requirements

Based on the kinematic drive cycle analysis an electric taxiing system can be developed with equivalent performance parameters as presented in Table 2-2. This would result in an "ideal" electric taxiing system with the exact same on-ground performance as it was seen in conventional taxiing, ensuring that the propulsion system matches perfectly with every of the presented drive cycles.

Since the aim of this thesis is the development of a system with similar driving performance as conventional taxiing, it is aimed to meet the performance parameters of the ideal solution in order to reduce on-ground operation times as much as possible. However, it can also be seen that the selected drive cycles vary a lot since on-ground movements in the airport area are always different and never predictable. Whereas some of the speed profiles show a relatively low performance, others feature a more aggressive taxiing behavior, resulting in high peak performance parameters such as the ones listed in Table 2-2.

The recorded GPS data is assumed to be accurate enough for the purpose of evaluating taxiing speed profiles. However, it cannot be guaranteed that the obtained data does not contain any minor signal errors causing higher velocity or acceleration recordings. Hence, the aim is to avoid oversizing the system based on high performance parameters that potentially are influenced by GPS errors and GPS device tolerances. Due to challenging space limitations in the aircraft, in the

undercarriage in particular, the system requirements need to be defined carefully in order to ensure the feasibility of the developed system.

Based on the present boundary conditions it has been decided to select the 85% quantiles [1] for each of the computed performance parameters. This allows an appropriate taxiing performance considering every single drive cycle without oversizing the system for rare occurring maximal performance maneuvers such as peak velocities or peak accelerations. The 85% quantiles for maximum velocity, acceleration, traction force and power for all available takeoff and landing driving profiles are summarized in Table 2-3.

Table 2-3 – Kinematic Drive Cycle Analysis Results – 85 % Quantiles

Parameter 85% Quantile	**Taxi-Out**	**Taxi-In**
Taxiing Velocity $(v_{0.85})$	51.78 km/h	57.93 km/h
Acceleration $(a_{0.85})$	0.96 m/s²	0.9 m/s²
Traction Force $(F_{tr.0.85})$	87.5 kN	81.78 kN
Traction power $(P_{tr.0.85})$	438.65 kW	365.06 kW

The system requirements for the electric taxiing system are directly derived from the 85% quantiles. Aiming an effective solution for both taxi-out and taxi-in maneuvers the system needs to meet the maximum value for each performance parameter (Table 2-3). The taxiing system performance parameters required at the wheel of the aircraft are defined as listed in Table 2-4.

[1] 85% of the computed performance parameters for each of the proposed drive cycles are below this value.

Table 2-4 – Performance Requirements Electric Taxiing System

Parameter	**Value**
Max. Velocity at the Wheel $(v_{w.max})$	58 km/h
Max. Acceleration at the Wheel $(a_{w.max})$	0.96 m/s²
Max. Traction Force at the Wheel $(F_{w.tr.max})$	88 kN
Max. Wheel Traction Power at the Wheel $(F_{w.tr.max})$	439 kW

2.3 Electric Taxiing System Sizing

The defined system requirements (Table 2-4) need to be satisfied in order to achieve an appropriate on-ground performance similar to conventional taxiing. These performance parameters need to be available at the wheels, i.e. transmitted to the ground. Thus, an electric taxiing system needs to be sized that is able to provide these "net" values to the road, compensating all powertrain losses and motion resistances.

In this section the powertrain development and the electric taxiing system sizing process for a selected midsize commercial aircraft will be presented.

2.3.1 Powertrain Concept

The powertrain that is responsible for propelling the aircraft wheels works according to the following principle: The required energy or power is provided by the on-board power supply which is assumed as a bidirectional energy source, allowing energy supply for propulsion as well as energy recuperation during braking situations. This can be the combination of a battery, the aircraft APU, an ultra-capacitor, a fuel cell and/ or other energy storage devices. The demanded electrical energy is controlled by the power electronics (i.e. inverter, motor controller) and send from the energy storage device to the electric motor or vice versa. A potential gearbox system between the motor and the wheel ensures the

functionality of the system by increasing the torque and decreasing the speed coming from the motor with respective gear reduction, and finally transmitting the requested torque or power respectively to the wheel. The powertrain of the electric taxiing system (ETS) is visualized in Figure 2-9.

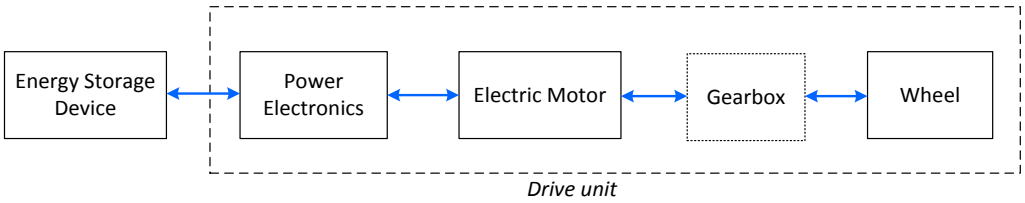

Figure 2-9 – ETS Powertrain Concept

The number of drive units including electric motor and gearbox at the wheel, can be modified based on the total system force and power demands, which will be analyzed subsequently in section 2.3.5.4.

2.3.2 Aircraft Type Selection

As described earlier, electric taxiing systems are not beneficial for every flight operation. This is due to the extra mass that is added to the overall weight of the aircraft influencing the flight operation in terms of fuel consumption. The longer the flight phase, the greater is the effect on the fuel consumption. Thus, aiming maximal possible fuel savings during the overall flight mission, the optimum trade-off between reduced fuel consumption through electrified taxiing and adding weight to the aircraft needs to be found. Studies show that on-board electric taxiing systems are more beneficial for short range operations, rather than for long range operations [3], [13], [32]. Thus, this thesis focuses on the development of a taxiing system for a short haul midsize aircraft. For the powertrain sizing an Airbus A321, a commercial single-aisle commercial aircraft, is selected.

2.3.3 Electric Taxiing System Weight Estimation

For an accurate powertrain sizing and system evaluation not only the weight of the conventional aircraft but also the mass of the added taxiing system needs to be considered. Therefor the system is divided into two main subsystems contributing to the system weight: the energy storage system (ESS) and the drive unit including electric motor and gearbox. The weight estimation of the system is an iterative process since it depends on the final powertrain components. For an approximation of the ESS mass the power density of 0.75 kW/ kg for state-of-the-art Lithium Ion batteries is applied along with the ESS peak power indicated in eqn. (31) [33]. Although the type of the ESS is not specified for the proposed system, the mass of a Lithium Ion for the given power requirement can be used as an appropriate benchmark for the weight estimation. The mass of the drive unit is calculated for the peak power indicated in eqn. (30) with 1.2 kW/ kg based on the technical targets for Electric Traction Drive Systems in 2015 [34]. This gives an estimated weight of 595 kg for the ESS and 435 kg for the drive unit, resulting in a total weight of 1030 kg. For a conservative design, a weight of 1100 kg is assumed. This leads to an increase of the total aircraft ramp weight of the Airbus A321 from 89.4 tonnes to 90.5 tonnes (Table 2-5). This value is used for the subsequent powertrain sizing and system evaluations.

Table 2-5 – Weight Analysis - Airbus A321 with Electric Taxiing System

Aircraft Type	Airbus A321
Max. Ramp Weight [35]	89.4 t
Electric Taxiing System Weight Estimation	1.1 t
Aircraft Total Weight (including system mass)	90.5 t

A weight sensitivity analysis in [36] has shown that varying the weight of the electric taxiing system has only minor effects on the powertrain component sizing since it is only a small percentage of the total aircraft mass.

2.3.4 Rolling Friction and Traction Analysis

The concept for the developed electric taxiing system is an integration of the electric motors into the wheels of the aircraft's undercarriage. Thus, an analysis of the rolling friction and maximum traction between the wheels and the tarmac is conducted in the following.

2.3.4.1 Minimum Traction Force

During the on-ground movement the aircraft's motion is caused by the traction (or tractive) force F_{tr} that is transmitted from the drive unit through the wheels to the ground. While moving a rolling resistance F_{rr} which is induced by the contact between the wheel tire and the tarmac counteracting the tractive force needs to be overcome. As a consequence, for moving the aircraft equation (1) needs to be satisfied.

$$F_{tr} > F_{rr} \tag{1}$$

The minimum traction force which is equal to the rolling resistance needs to be overcome when initiating rolling of the aircraft on the tarmac from standstill. Thus, this force is also known as breakaway force or resistance [37].

$$F_{tr.min} = F_{rr} \tag{2}$$

The rolling resistance is dependent on the aircraft's weight force F_W and the rolling friction coefficient c_{rr}.

$$F_{rr} = F_W \cdot c_{rr} = m_{tot} \cdot g \cdot c_{rr} \tag{3}$$

With the assumed total mass of an Airbus A321 and a rolling friction coefficient of 0.009 for tires on dry asphalt [1], this results in the minimum traction force.

$$F_{tr.min} = 7.99\ kN \tag{4}$$

Thus, an on-ground movement cannot be expected if the available traction force is lower than the calculated breakaway force. However, this calculation regards to dry conditions between tire and asphalt. Further investigations for different ground or environmental conditions can be conducted by adjusting the rolling coefficient of friction.

2.3.4.2 Maximum Traction Force

After determining the required breakaway force, it needs to be investigated how much force can be transmitted to the ground. The maximum traction force characterizes the point where the traction force overcomes the adhesion force F_{adh}, also known as static friction force. At this point the tires begin to skid due to lacking adhesion between tire and ground. Hence, tire skid is expected when

$$F_{tr} > F_{adh}\ . \tag{5}$$

In order to ensure that the system works appropriately, the applied traction force needs to be lower than the static friction force:

$$F_{tr} \leq F_{tr.max} = F_{adh} \tag{6}$$

The static friction force can be determined by

$$F_{adh} = \mu \cdot F_w \cdot WD \tag{7}$$

where μ expresses the coefficient of friction and WD the weight distribution of the aircraft.

The static friction force is distinctly dependent on the location of the propulsion system. Hence, placing the motor units in the MLG will lead to a completely different dynamic behaviour than a placement in the FG. For the selected aircraft type the weight distribution is about 0.9, i.e. 90 % of the total aircraft weight is supported by the MLG and 10 % by the FG [32]. Another influencing factor is the number of wheels available in the respective undercarriage. Whereas the MLG of an Airbus A321 is composed of two wheel assemblies with two wheels each, the front gear contains only two wheels in total.

With the coefficient of friction $\mu = 0.8$ [32] for tires on asphalt under dry conditions, the maximum traction force can be calculated for an electric taxiing system implemented into the MLG.

$$F_{tr.max.MLG} = \mu \cdot F_w \cdot 0.9 = 639.22\ kN \tag{8}$$

Distributing the total force to the four wheels in the MLG the maximum tractive force for a single tire can be obtained.

$$F_{tr.max.MLG.tire} = \frac{639.22\ kN}{4} = 159.805\ kN \tag{9}$$

In a similar manner, the maximum tractive force for a FG system $F_{tr.max.FG}$ and the force for a single tire within the FG $F_{tr.max.FG.tire}$ can be calculated.

$$F_{tr.max.FG} = \mu \cdot F_w \cdot 0.1 = 71.02\ kN \tag{10}$$

$$F_{tr.max.FG.tire} = \frac{71.02\ kN}{2} = 35.51\ kN \tag{11}$$

2.3.4.3 Selection of the Electric Taxiing System Location

The maximum traction investigation shows that the aircraft weight distribution has a great impact on the maximum traction available at the wheels, limiting the force or torque that can be transmitted from the wheels to the ground. Due to the high weight concentration in the aft of the aircraft a much higher traction is expected when placing the propulsion unit in the MLG. The maximum traction force that can be transmitted through a single tire to the ground before the tires begin to skid is about 4.5 times larger than with a FG propulsion system.

Thus, an implementation of the electric propulsion unit into the MLG allows applying much higher traction forces when propelling the aircraft. The lack of traction within a FG causing tire slip can have a crucial impact on the overall taxiing performance, in particular under degraded ground or weather conditions such as rain or snow on the taxiway. By analyzing the impact of different road conditions, i.e. maximum traction evaluation with varying coefficients of friction, it has been found that only a MLG system is able to provide the required traction force at any time, which has also been concluded in a study in [32].

In order to allow the highest power capabilities and provide the best possible on-ground driving performance an electric taxiing system integrated into the MLG is selected preventing the risk of lacking traction.

2.3.5 Torque and Power Analysis for Driving the Main Landing Gear

2.3.5.1 Traction Effort and Resistances at the Wheels

The required system traction force and traction power presented in Table 2-4 represent the net performance parameters required at the wheels. Since the aircraft has to overcome resistances while moving on-ground the system needs to be sized in order to compensate these resistances, providing the required traction

output. The acting resistances during taxiing include rolling, aerodynamic and grade resistances.

The total force the system needs to deliver is called gross force and takes into account all present resistances while moving. Thus, the gross traction force $\hat{F}_{tr}$ can be computed as the sum of the net traction force and the existing resistances acting on the aircraft [38].

$$\hat{F}_{tr} = F_{tr} + R_{rr} + R_{aero} + R_{grade} \tag{12}$$

where $F_{tr} = m_i \cdot a$ represents the current traction force to the road, R_{rr} is the rolling resistance according to eqn. (3), R_{aero} the aerodynamic resistance and R_{grade} the grade resistance. All forces acting on the aircraft are visualized in Figure 2-10.

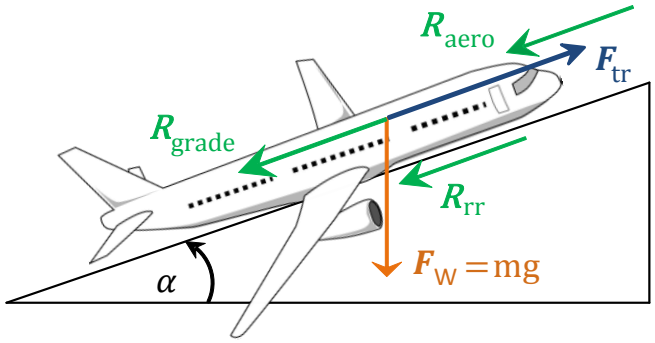

Figure 2-10 – Simplified Dynamics during On-Ground Motion

The traction force F_{tr} is defined as the product of inertial mass m_i and instantaneous acceleration a.

$$F_{tr} = m_i \cdot a \tag{13}$$

Consequently, the maximum available traction force $F_{tr.max}$ can be determined at maximum acceleration a_{max}.

The inertial mass m_i includes the aircraft's total mass m_{tot} as well as the equivalent mass of all rotating parts with the respective inertias rotating parts available in the propulsion system δ. Here, the equivalent mass δ is dependent on the final electric taxiing system design since it considers certain parameters such as number of electric motors, motor shaft inertia and inertia of the gearbox or gearboxes respectively. The calculation of δ involves the wheel mass moments of inertia in the MLG and FG which are influenced by parameters such as number of wheels, wheel dimensions, tire and rim mass [36], [39].

For the final powertrain, implemented into an Airbus A321, the inertial mass results in

$$m_i = 1.01 \cdot m_{tot} \,. \tag{14}$$

With the highest acceleration a_{max} obtained from the respective drive cycle one obtains the maximum traction force at the wheels (see Table 2-2).

$$F_{tr.max} = m_i \cdot a_{max} \tag{15}$$

As introduced previously, the rolling resistance R_{rr} (or F_{rr}) indicates the required breakaway force when initiating a rolling motion from standstill (eqn. (3)), and is dependent on the aircraft mass and the rolling friction coefficient.

The aerodynamic resistance, also known as drag, is heavily dependent on the taxiing speed of the aircraft [36].

$$R_{aero} = \frac{1}{2} \cdot \rho_{air} \cdot c_D \cdot A_{ref} \cdot v^2 \tag{16}$$

In order to determine the maximum required traction force, the highest speed during taxiing is considered, resulting in the maximum available drag $R_{aero.max}$. With an air density of $\rho_{air} = 1.2\ kg/m^3$ at $20\ °C$ [36], and

$c_D \cdot A_{ref} = 2.6\, m^2$ (coefficient of drag times active frontal area) for an Airbus A321 [40] and $v_{max} = 58\ km/h$ (Table 2-2) this results in

$$R_{aero.max} = 404.926\ N\ . \tag{17}$$

The grade resistance R_{grade} is dependent on the aircraft's weight force and the existing grade available on the airport [12].

$$R_{grade} = \sin[\tan^{-1}(g_{max})] \cdot F_w \tag{18}$$

where g_{max} stands for the grade on the ground. The maximum grade allowed on airports is 1.5 % [41]. This means that high grades are not expected for the on-ground motion during taxiing. Thus, the grade resistance is neglected for the powertrain sizing. The grade resistance for different ramp grades was analyzed in [12].

Considering the net traction force $F_{w.tr.max}$ (Table 2-4) and the counteracting resistances, one obtains the maximum gross traction force which needs to be delivered by the electric taxiing system at the wheels.

$$\hat{F}_{tr.max} = F_{w.tr.max} + R_{rr} + R_{aero.max} = 96.4\ kN \tag{19}$$

2.3.5.2 Maximum Torque and Power Calculation

In consideration of the force acting at all wheels in the MLG, the applied tractive torque can be calculated based on the wheel dimensions. With a tire radius of $r_w = 622.5\ mm$ for an Airbus A321 MLG wheel [40], the required maximum mechanical torque of the electric taxiing system delivered to the wheels can be computed.

$$\hat{T}_{tr.max} = \hat{F}_{tr.max} \cdot r_{tire} = 60\ kNm \tag{20}$$

The gross power at the wheels $\hat{P}_{tr}$ is the product of the gross traction force $\hat{F}_{tr}$ and the current taxiing velocity v.

$$\hat{P}_{tr} = \hat{F}_{tr} \cdot v \tag{21}$$

Since the maximum traction force is not necessarily present at the highest velocity, it is required to investigate the instantaneous traction power along the drive cycle. By doing so, the actual maximum traction power for the respective drive cycle can be obtained. This procedure was performed with the simulation model during the kinematic drive cycle analysis resulting in the maximum gross traction power as listed in Table 2-6. The maximum gross tractive power, i.e. power to the wheels, therefore results in:

$$\hat{P}_{tr} = 476\ kW\ . \tag{22}$$

Table 2-6 – Kinematic Drive Cycle Analysis Results: Peak Gross Tractive Power

Parameter	**Taxi-Out Drive Cycles**	**Taxi-In Drive Cycles**
Peak Gross Tractive Power ($\hat{P}_{tr}$)	476.14 kW	441.97 kW

2.3.5.3 Gear Reduction

Due to the high torque requirements a gear reduction is considered as mandatory for the developed system. Even if the total system torque is distributed across four individual electric motors located in the four separated wheels of the Airbus A321, there are no electric motors available on market providing the necessary torque for a direct drive option.

In order to ensure the required system torque a gear reduction is chosen for the proposed electric taxiing system. In particular, a planetary gearbox is select due to the given size constraints in the rim of the Airbus A321 MLG

wheels. Planetary gear reductions are characterized by their small size, low weight for high gear ratios and high efficiencies.

The gear ratio G is defined as [42]

$$G = \frac{n_{in}}{n_{out}} = \frac{T_{out}}{T_{in}}. \tag{23}$$

For a single-stage planetary gearbox, gear ratios of up to 13 are possible [43]. For a conservative design, a gear ratio $G = 12$ is chosen in this thesis.

2.3.5.4 Calculation of Motor Parameters for Various Numbers of Drive Units

Based on eqn. (23), the required maximum motor speed $n_{M.max}$ can be determined as product of the maximum available speed at the wheel $n_{w.max}$ and the selected gear ratio.

$$n_{M.max} = n_{w.max} \cdot G \tag{24}$$

where $n_{w.max}$ is the maximum available rotational speed at the wheel which is dependent on the linear velocity at the wheel $v_{w.max}$ and the tire radius of an Airbus A321 MLG wheel.

$$n_{w.max} = \frac{v_{w.max}}{2\pi \cdot r_w} \tag{25}$$

Here, the linear velocity at the wheel equals the maximum taxiing speed $v_{w.max} = 58\ km/h$ (Table 2-4). Thus, the required rotational speed at the wheel and the rotational speed of the motor can be calculated.

$$n_{w.max} = 247.15\ rpm \tag{26}$$

$$n_{M.max} = 2965.78\ rpm \tag{27}$$

The total maximum motor output torque of the system $T_{system.M.max}$ can be calculated based on the maximum traction torque for the selected gear ratio.

$$T_{system.M.max} = \frac{\hat{T}_{tr.max}}{G} = 5000.5\ Nm = 5\ kNm \tag{28}$$

The total motor output power of the system $P_{system.M.max}$ is dependent on the maximum gross traction power at the wheels and the efficiency of the gearbox η_{GB}.

$$P_{system.M.max} = \frac{\hat{P}_{tr}}{\eta_{GB}} \tag{29}$$

With an assumed constant efficiency for the planetary gearbox of 96 % (see Table 2-10) the system power results in

$$P_{system.M.max} = 495.83\ kW\ . \tag{30}$$

Due to the high motor torque and power requirements despite the chosen high gear ratio (eqns. (28) and (30)), it is necessary to consider more than one drive unit (electric motor) to ensure that the needed torque and power can be achieved. During a market research it has been found that there is no electric motor available providing the required specifications (2970 rpm rotational speed, 496 kW peak power and 5000 Nm peak torque) within the small space available in the MLG wheel.

Besides, an electric taxiing system with only one drive unit is not recommended due to a lack of driving performance which occurs when only one MLG undercarriage is propelled. With such a configuration it is not possible to control each of the two MLG wheel assemblies independently which would influence the taxiing behavior, in particular when performing turns.

When using several propulsion units, the motor parameters can be reduced by distributing both torque and power on the different individual motors. Hence, a comparison between various numbers of drive units is conducted to find the optimal powertrain topology for the electric taxiing system. Since there are four wheels in total available within the MLG, three different solutions are investigated: a system with one motor, two motors and four motors, respectively. Table 2-7 shows the varying motor requirements when increasing the number of drive units.

Table 2-7 – Motor Specifications for Various Numbers of Drive Units

Parameter	**System with 1 Motor**	**System with 2 Motors**	**System with 4 Motors**
Motor Max. Torque $T_{M.max}$	5000 Nm	2500 Nm	1250 Nm
Motor Max. Power $P_{M.max}$	496 kW	248 kW	124 kW
Max. Motor Rotational Speed $n_{M.max}$	2970 rpm	2970 rpm	2970 rpm

2.3.5.5 Selection of Final Powertrain Architecture

Four electric motors are chosen to guaranty that the motor requirements of the entire system can be achieved (Table 2-7) in order to satisfy the system performance requirements obtained from the drive cycle analysis (Table 2-4). Thus, an electric taxiing system with four drive units, i.e. electric motor plus gearbox, implemented in each of the four MLG wheels of the Airbus A132, is proposed. A schematic of the final powertrain architecture is visualized in Figure 2-11.

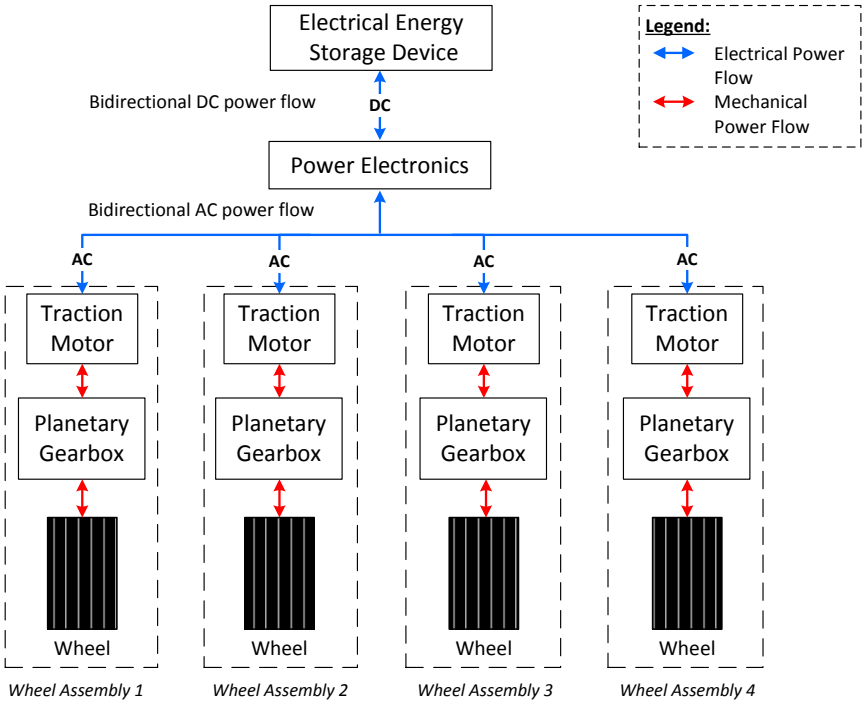

Figure 2-11 – Powertrain Architecture with Four Drive Units

2.3.5.6 Required Motor Specifications

The final motor specifications of the identical electric motors that are implemented into the wheels in the MLG are summarized in Table 2-8. Here, the continuous power and torque values used for the simulation model (in section 2.4) are assumed as 50 % of the respective peak parameters.

Note: For the powertrain sizing, in particular the motor sizing, it is assumed that in generating mode, i.e. during regenerative braking, the electric motors are able to provide equal torque and power values as during motoring mode.

Table 2-8 – Final Motor Specifications

Parameter	**Value**
Peak Torque	1250 Nm
Continuous Torque [2]	625 Nm
Peak Power	124 kW
Continuous Power [3]	62 kW
Maximum Speed	2970 rpm
Rated Speed [4]	947 rpm

An intensive market research has shown that there are no electric motors available providing the torque and power parameters with small outer dimensions to be able to fit into the limited space of a MLG wheel. Not even high performance motors such as the ones by the company YASA, that develops axial flux permanent magnet (AFPM) motors, provide the required performance parameters, particularly the high peak torque. The characteristics of their most powerful motor are listed in Table 2-9.

Table 2-9 – "YASA-750" Motor Specifications

Parameter	**Value [Unit]**
Peak Torque	790 Nm
Continuous Torque	400 Nm
Peak Power (at 350 V)	100 kW
Continuous Power	75 kW
Maximum Speed	3250 rpm

[2] The continuous torque is assumed as approximately 50 % of the peak torque.
[3] The continuous power is assumed as 50 % of the peak power.
[4] The rated speed is calculated based on peak torque and peak power.

Thus, an electric motor, an AFPM motor in particular, based on the defined performance specifications for the electric taxiing system for an Airbus A321 will be designed in section 4.

2.3.5.7 Clutch Mechanism

An additional clutch mechanism is required since the electric motors are only sized for the maximum available taxiing speed of 58 km/h. However, during takeoff and landing the aircraft reaches much higher speeds (up to 250 km/h during touchdown). Since the drive units, in particular the electric motors are limited in terms of maximum rotational speeds, a clutch mechanism between electric motor and wheel is foreseen to disengage the motor from the drivetrain during high speed operations. Thus, no regenerative braking can be expected for the proposed taxiing system during the landing phase due to the required clutch mechanism.

2.3.5.8 Energy Source

An additional energy source is selected to power the electric propulsion system. The bidirectional energy source that is capable of providing traction energy as well as regenerating energy during braking is not specified in this thesis. This can be a battery, ultra-capacitor, or any other energy storage system (ESS). The peak power of the energy source $P_{ESS.max}$ is assumed to be equal to the peak system power $P_{system.M.max}$ (eqn. (30)) divided by the motor and inverter efficiency η_M and η_I according to Table 2-10 to ensure that all of the four electric motors can run at their peak power.

$$P_{ESS.max} = \frac{P_{system.M.max}}{\eta_M \cdot \eta_I} = 579.51\ kW \tag{31}$$

The power of the energy storage device is important for estimating the total weight of the electric taxiing system (see section 2.3.3).

2.4 Modeling and Evaluation of the Electric Taxiing System

2.4.1 Electric Taxiing Simulation Model

The developed powertrain of the electric taxiing system is modeled in Matlab/ Simulink [44]. By using the simulation model the sized powertrain can be validated and tested on the available taxi-out and taxi-in drive cycles. Besides, further investigations can be performed regarding traction effort and resistances for various ground or environmental condition, energy consumption and regenerative braking capabilities during taxiing.

The simulation model including different subsystems based on the proposed powertrain configuration including the different subsystems is developed as follows: Four drive units (motor plus gearbox), are connected to the wheels in the MLG to propel the aircraft during on-ground movements. In the simulation model this is realized with four individual motor subsystems connected through a respective gearbox system to a "Vehicle Dynamics" model which calculates traction effort and resistances between the wheel and the tarmac. Each of the motor models is powered by the energy source. The energy storage system is modeled as a bidirectional energy source which is able to provide energy to the motors during traction mode as well as recuperation of energy during regenerative braking. Here, the power flow is controlled by the "Power Electronics" (Inverter) subsystem. The drive cycles are imported as a simulation input defining the desired taxiing speed profile. The "pilot" subsystem which is based on a PID controller compares the current velocity of the simulation model and the given taxiing speed profile and generates acceleration or braking commands, respectively. In case of braking, it is differed between regenerative braking and friction braking, depending on the amount of regenerative braking power the electric motors are able to provide during generating mode. The control strategy

of the "Regenerative Braking Control" subsystem follows the attempt of recuperating energy whenever the braking power demand coming from the pilot model is within the limits of the maximum power of the electric motors. Hence, friction braking is performed when the motors cannot provide the required braking power anymore. This ensures that each braking command is satisfied during taxiing. Figure 2-12 illustrates the simplified signal and power flow between the subsystems of the circuit-based simulation model.

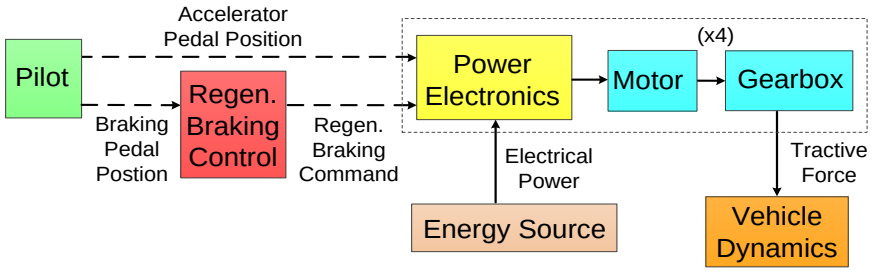

Figure 2-12 – Electric Taxiing Simulink Model [36]

For a conservative design, constant efficiencies are assumed in this analysis. However, if available the simulation model could be improved by implementing efficiency maps such as electric motor or inverter efficiency maps in order to increase the fidelity of the developed electric taxiing system model [45]. The selected efficiencies for the powertrain components are listed in Table 2-10.

Table 2-10 – Efficiencies for Powertrain Components in the Simulation Model

Powertrain Component	**Efficiency**
Motor	92 %
Inverter	94 %
Energy Source	90 %
Gearbox	96 %

2.4.2 Simulation Results

During the preliminary kinematic drive cycle analysis the various drive cycles have been already analyzed in order to define system performance requirements. In this section an evaluation of the proposed powertrain is performed. A simulation of the sized powertrain with the available drive cycles will show the performance of the electric taxiing system in comparison with conventional taxiing.

2.4.2.1 Taxiing Performance Evaluation

The driving behavior of the system is investigated for all available taxi-out and taxi-in speed profiles. Figures 2-13 and 2-14 show the system evaluation for two very demanding drive cycles. Both drive cycles are characterized by high taxiing velocities and accelerations leading to high torque and power demands. Despite high performance challenges on both the Hamilton taxi-out cycle (Figure 2-13) and the taxi-in procedure on Munich airport (Figure 2-14), it can be seen that the system is able to follow the recorded speed profiles very well. Only in the Munich drive cycle it is noticeable that the system is not able to reach the top speed during taxiing. However, this is expected because the unusual high peak velocity velocity of 67.6 km/h was recorded in that particular cycle but the system was sized for 58 km/h only.

Thus, it can be concluded that the electric taxiing system is able to meet the defined performance requirements. Besides demonstrating the feasibility of the proposed powertrain, the simulation results show that there is nearly no loss in performance compared to conventional taxi operations. This helps ensuring time savings compared to existing electric taxiing systems with relatively low taxiing velocities as introduced previously.

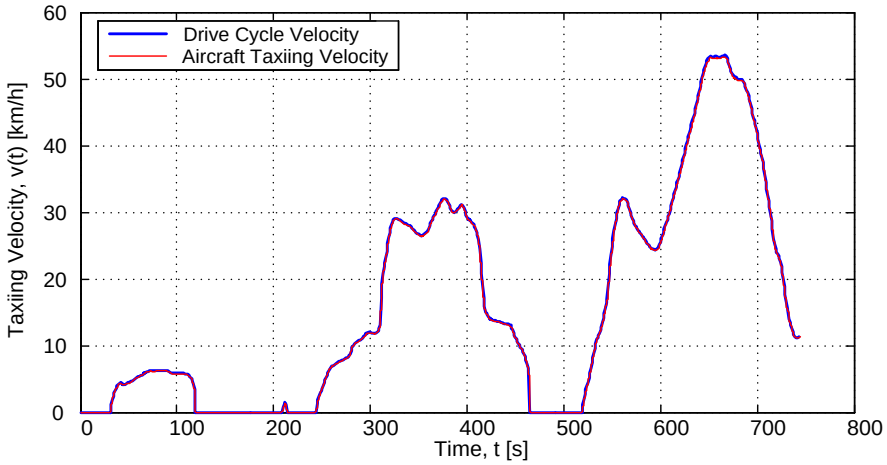

Figure 2-13 – Hamilton (YHM), Canada – Taxi-Out Drive Cycle Match

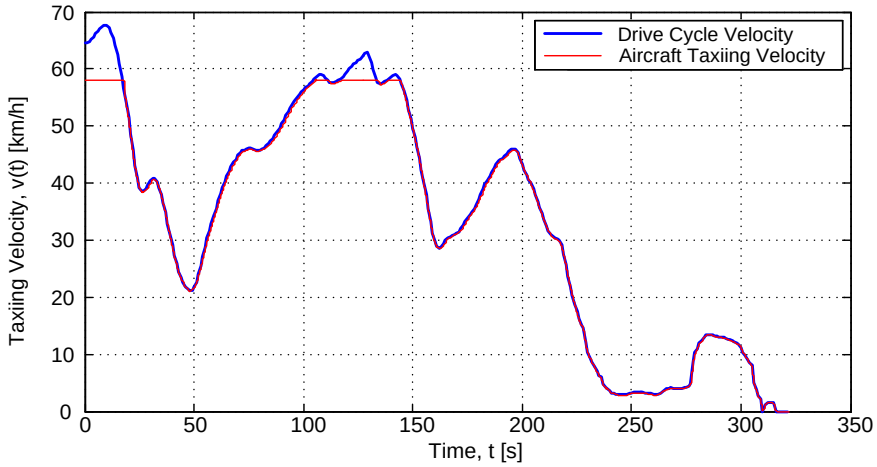

Figure 2-14 – Munich (MUC), Germany – Taxi-In Drive Cycle Match

Since the recorded drive cycles represent a wide variety of diverse taxiing maneuvers on international airports it can be assumed that the proposed system would show a similar performance on every other airport worldwide, making it a suitable alternative for conventional taxiing.

2.4.2.2 Analysis of Electric Motor Operation

Since the electric taxiing system powertrain including the electric motors is sized for the most demanding drive cycles it is expected that the maximum potential of the motors is not utilized in all of the available drive cycles. This means that the maximum power and torque output during taxiing will be lower than the specified peak parameters listed in Table 2-8. The simulation results show that the motors operate more frequently within the continuous power threshold (62 kW), not only during low demanding drive cycles but also in high challenging speed profiles, for instance in the taxi-in procedure on Munich Airport (Figure 2-15). Whereas the motors are rated for 124 kW peak power, the average power of each single motor during the Munich landing cycle is 40.34 kW. The average motor power averaged for all drive cycles is merely 14.61 kW. This is relatively low compared to the required peak power (Table 2-11).

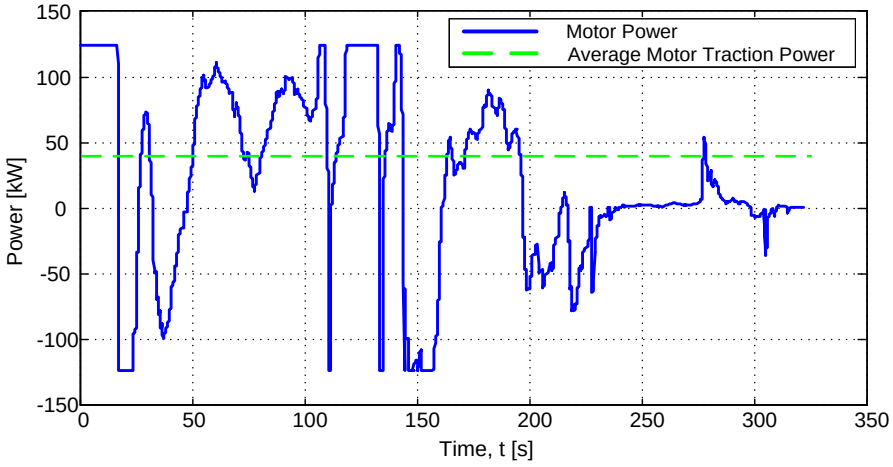

Figure 2-15 – Munich (MUC) – Taxi-In – Motor Power

Similarly, the motor output torque of each motor operates within low torque regions, e.g. in Munich the rms torque is only 327.42 Nm. Only during short, challenging acceleration procedures high torque demands can be found

(Figure 2-16). Overall it can be seen that during operation the limiting torque-speed curve is reached in short time periods only (Figure 2-17) and in some drive cycles not at all. An example of a very low demanding drive cycle where the maximum torque-speed curve is never reached is shown in Figure 2-18.

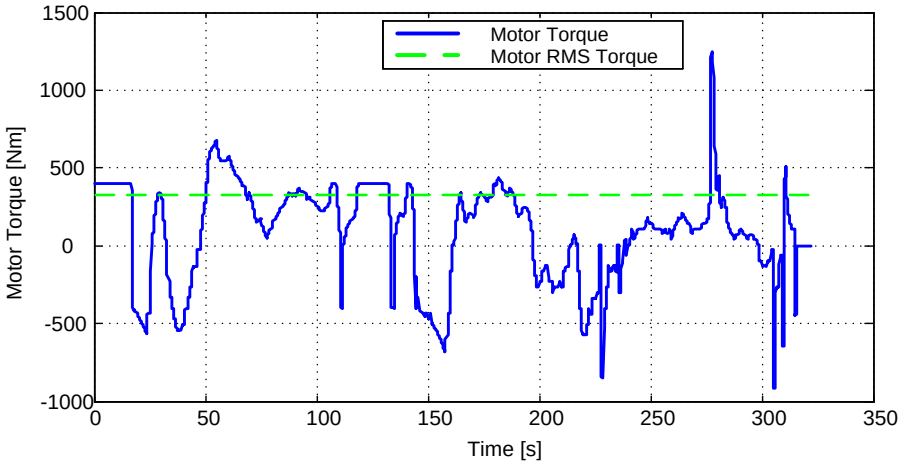

Figure 2-16 – Munich (MUC) – Taxi-In – Motor Torque

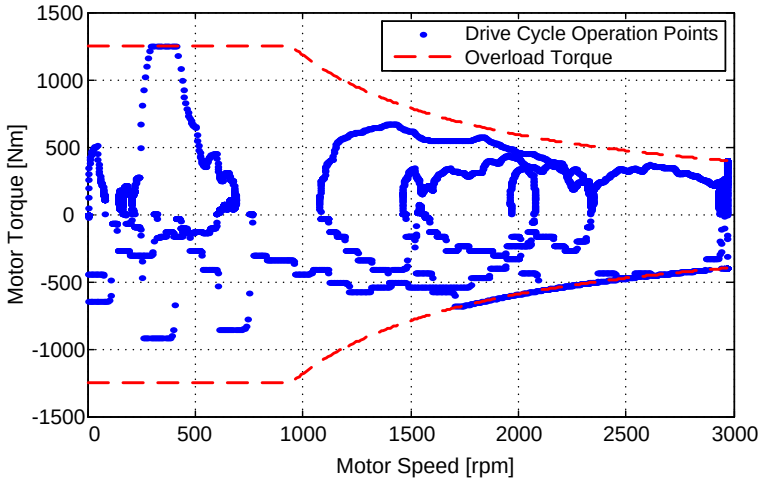

Figure 2-17 – Munich (MUC) – Taxi-In – Motor Torque vs. Speed

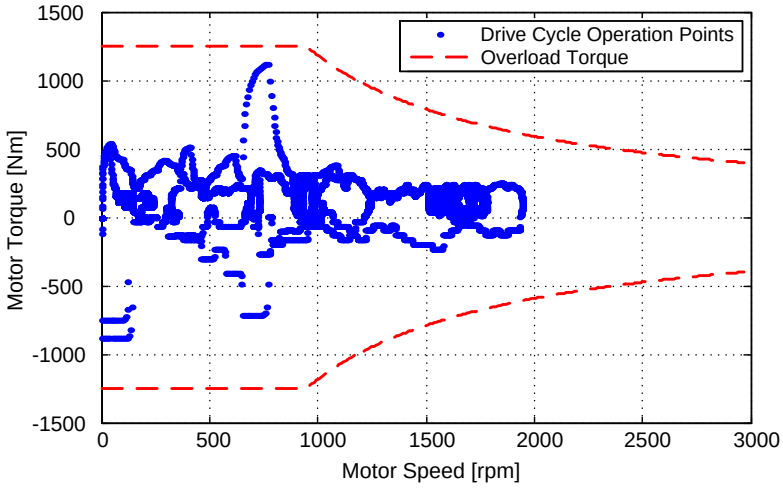

Figure 2-18 – Dallas/Fort (DFW) – Taxi-Out – Motor Torque vs. Speed

However, aiming a similar driving behavior to conventional taxiing the selected motor performance parameters are required to follow each of the various drive cycles.

Table 2-11 summarizes the average motor power and average torque for all evaluated takeoff and landing drive cycles.

Table 2-11 – Motor Performance Analysis Results

Parameter [unit]	Munich Taxi-In	Dallas/ Fort Worth Taxi-Out	Average of Taxi-Out Cycles	Average of Taxi-In Cycles	Average of all drive cycles
Average Motor Traction Power [kW]	40.344	8.955	12.276	16.94	14.608
Motor RMS Torque	327.42	140.476	194.533	221.937	208.235

Since the main contribution of this thesis is the investigation of electric taxiing system requirements in order to design an electric machine based on the proposed performance specifications, an analysis of the energy consumption and the investigation of regenerative braking capabilities are not addressed in this

thesis. These investigations for a similar electric taxiing system are presented in [12] and [36].

3 FUNDAMENTALS OF AXIAL FLUX PERMANENT MAGNET (AFPM) MOTORS

3.1 Features of AFPM Motors

3.1.1 Working principle

The working principle of axial flux permanent magnet (AFPM) motors is similar to their radial flux PM (RFPM) counterparts. The main difference is that the torque is generated by electromagnetic forces between the stator and the rotor, where the magnetic field is created in axial direction rather than in radial direction. AFPM machines are characterized by their compact disc-shape, which makes them an alternative solution to cylindrical RFPM machines. Due to the large diameter to length ratio this machine type is also called disc-type or pancake motor. The feature of having compact disc-shape stators and rotors also allows designing geometries with various numbers of air gaps since rotors and stators can be stacked up in single-stage or multi-stage design variants [5], [46].

3.1.2 Advantages of AFPM Motors

In general, AFPM machines are superior to their radial flux counterparts due to a compact size and a high torque-to-weight ratio because less core material is required. In particular when the available axial length is short and the diameter is large a higher electromagnetic torque and torque density can be increased by using an AFPM machine. Besides, in a disc-type machine the number of modules, i.e. stator and rotor discs can be adjusted based on the given torque and power requirements. Excellent low speed performance and high torque generating

capacity can be realized since a large number of poles can be placed in the rotor. They also provide a planar and easily adjustable air gap. Furthermore, lower noise and vibration can be expected for AFPM machines [46], [47].

3.2 Topologies and Geometries

AFPM motors can have various structures. An important topology parameter is the number of stators and rotors. The disc-shaped stator and rotor modules can be varied based on performance and space requirements. In general, AFPM machines can be grouped into the following topologies [46]:

- Single-sided AFPM machines
- Double-sided AFPM machines
- Multi-stage (multi-disc) AFPM machines

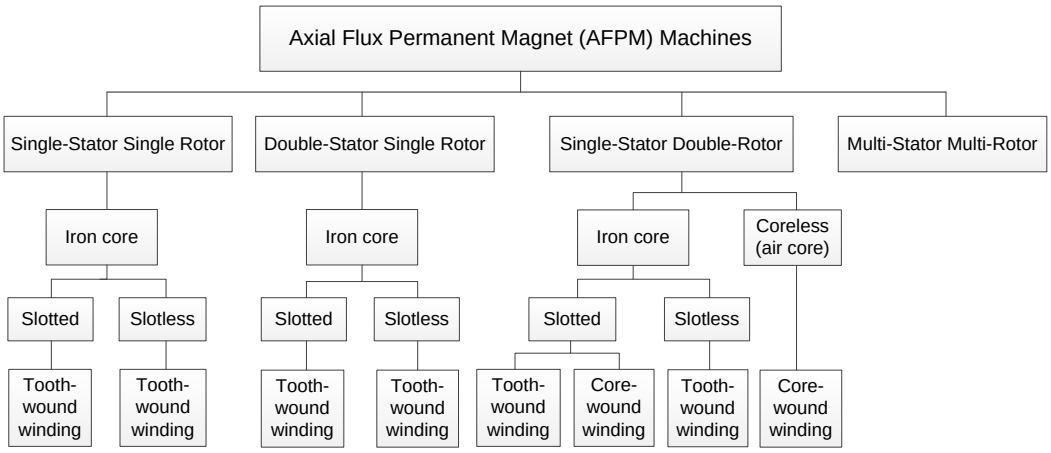

Figure 3-1 – Classification of AFPM Machines

Additionally, each of these topologies can accommodate cored or coreless and slotted or slotless stators. The stator windings can be classified as drum windings (tooth-wound windings) or ring windings (core-wound windings). Besides, the rotor can be realized with interior or surface mounted permanent magnets. Figure 3-1 displays a general classification of AFPM machines. The

schematics of the basic topologies of AFPM motors are illustrated in Figures 3-2 and 3-3.

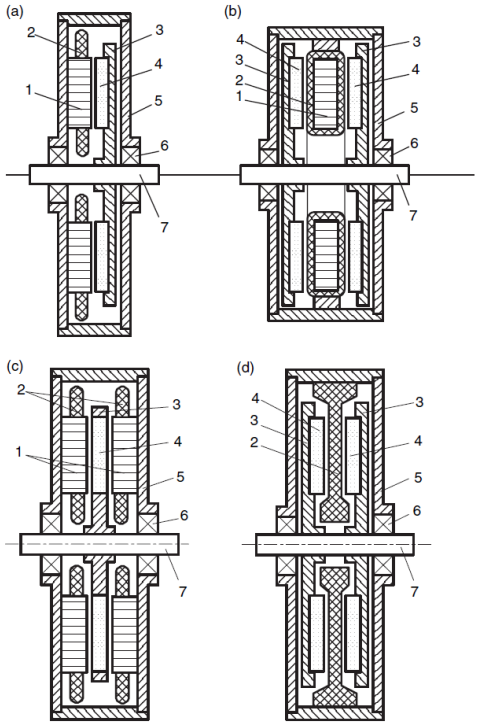

Figure 3-2 – Basic Topologies of AFPM Topologies: a) single-sided with slotted stator, b) double-sided with internal slotless stator and double rotor, c) double-sided with slotted stators and internal rotor, d) double-sided with coreless internal stator; 1–stator core, 2–stator winding, 3–rotor, 4–PM, 5-frame, 6–bearing, 7–shaft [46]

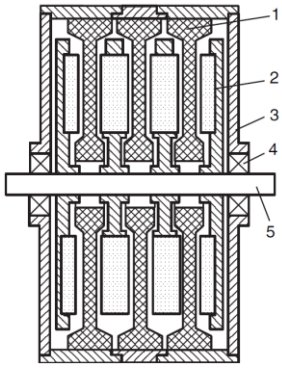

Figure 3-3 – Multidisc AFPM Machine with Coreless Stator: 1–stator winding, 2–rotor, 3–frame, 4–bearing, 5–shaft [46]

3.2.1 Single-sided AFPM machines

The simplest type of AFPM machines is the single-stator single-rotor structure, also called single-sided machine. Here, the electromagnetic torque is generated by the interaction of one stator and one rotor. It is differentiated between conventional distributed windings or concentrated windings. The greatest advantage of the single-sided structure is the compact shape since the axial length is very short. The drawback of this machine type are the developed axial attracting forces that are significantly imbalanced [47]. Besides, the achievable torque capabilities are lower than with double-sided machines [46].

3.2.2 Double-sided AFPM machines

Compared to the single-sided machine structure, double-sided AFPM machines accommodate two air gaps instead of one. This can be realized by adding a rotor or a stator, respectively. It is differentiated between two different types:

- Double-stator single-rotor AFPM machines
- Single-stator double-rotor AFPM machines

In the first variant an internal rotor disc is located between two external stators. The windings are wound around each stator core. The windings can be connected both in series and in parallel. In general, a series connection is preferred in order to balance the axial attracting forces. A rotor disc with surface-mounted PMs or with interior PMs are both possible solutions for single-stator double-rotor AFPM machines [46]. The external cored stators can either be slotted or slotless stators. The single-stator double-rotor topology contains a slotted or slotless stator that is located between two rotating discs with PMs. The internal stator can be cored or coreless and furthermore slotted or slotless.

In general, double-sided machines are advantageous towards single-sided structures due to the higher torque capabilities and their balanced attracting forces.

3.2.3 Multi-stage AFPM machines

Based on the given torque requirements the topology of an AFPM machine can be extended to multi-stator multi-rotor (multi-stage) machines. The structure is similar to double-stator single-rotor or single-stator double-rotor topologies. The difference here is the number of modules, i.e. stators and rotors, which can be adjusted in order to satisfy the performance requirements. Hence, the torque capability can be increased without enlarging the machine diameter. This can be very important since the size of each disc is limited by several factors, for instance axial forces acting on the bearings or stiffness of the individual modules [46].

3.3 Topology Selection

A very compact AFPM motor topology delivering high torque capability is required in order to satisfy the requirements of the electric taxiing system. Hence, a double-sided machine structure is selected in order to satisfy these requirements and provide balanced axial forces.

In particular, a yokeless single-stator double-rotor topology with segmented stator windings is selected (Figure 3-4). This machine type is also called modular stator construction since the individual pre-wound stator teeth/ segments are combined to form a solid stator structure. This allows a high torque and power density and efficiency due to shortened end windings. This also results in a high copper slot fill factor and simplifies the winding process. Furthermore, no stator yoke is required for this topology. This leads to a decrease of the stator core, which results in a lighter machine weight [48]. Since this structure reduces

the mutual inductance between the winding phases it also allows for fault tolerance [48].

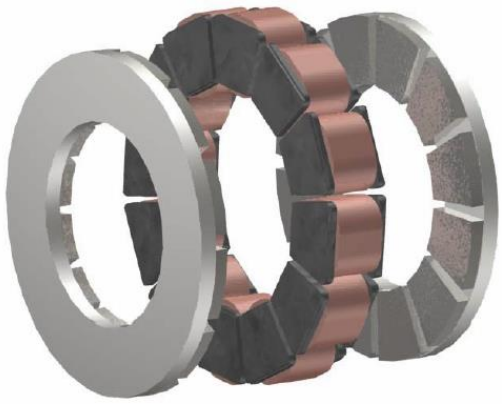

Figure 3-4 – Yokeless AFPM Machine with Segmented Armature [49]

The tooth wound stator windings are realized as fractional-slot (fractional number of slot of slots per pole per phase) windings, which provides a low cogging torque and torque ripple [50], [51]. Besides, fractional-slot concentrated windings (non-overlapping windings) provide a high copper slot fill factor particularly when combined with a segmented stator topology [52]. A drawback of fractional-slot windings are the magnetomotive force (MMF) space harmonic components which increases the rotor losses. Double-layer windings are selected since they allow lower rotor losses due to lower fundamental stator MMF harmonic waves and provide proved shorter end turns compared to single-layer windings [52].

The two external rotors of the selected machine topology accommodate surface-mounted permanent magnets. The stator end windings of the AFPM synchronous motor are overlapped by the stator segments. A schematic figure of the motor illustrating the flux path is can be seen in Figure 3-5.

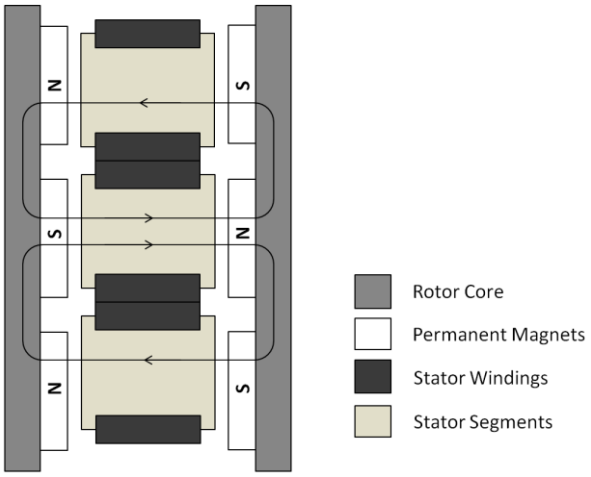

Figure 3-5 – Flux Path of the Yokeless AFPM Machine with Segmented Armature

4 AFPM MOTOR DESIGN AND ANALYSIS

Based on the defined motor specifications an AFPM motor is designed. This section describes the requirements, i.e. performance targets and constraints within the wheel of the aircraft MLG, as well as the design process that was conducted for the proposed AFPM machine.

4.1 Motor Requirements

4.1.1 Voltage Limitation

4.1.1.1 DC Link Voltage (Aircraft Standards)

As described earlier, the aircraft industry is moving into the direction of a More Electric Aircraft (MEA), aiming a replacement of existing on-board power sources in aircrafts by electrical systems. In this context, a new HVDC standard with DC link voltages of $\pm 270\,V$ is obtained for new system solutions containing a high voltage DC network aboard the aircraft, offering subsequent advantages regarding weight savings of the system overall [9]. Assuming a multi-source

system with two sources providing 270 V each, one obtains a total DC link voltage of 540 V. An equal voltage is also suggested in [53].

4.1.1.2 Maximum Motor Phase Voltage

For the inverter, a Space-Vector Pulse-Width Modulation (SVPWM) technique is assumed. The relation between the phase voltage of the electric machine and the DC link voltage of the inverter can be written as [54]

$$V_{phase} = V_{phase.RMS} = \frac{V_{dc}}{\sqrt{6}}. \tag{32}$$

The proposed motor is designed for the operational DC link voltage of 540 V. Thus, the maximum phase output rms voltage for a three phase inverter results in

$$V_{phase.RMS} = \frac{540\ V}{\sqrt{6}} = 220.454\ V. \tag{33}$$

The maximum phase peak voltage then becomes

$$V_{phase.peak} = V_{phase.RMS} \cdot \sqrt{2} = 311.769\ V. \tag{34}$$

4.1.2 Motor Dimensions

It is targeted to implement the electric taxiing system into the MLG of an Airbus A321. In order to prevent a complete redesign of the undercarriage a retrofitting into existing aircrafts is preferred. This is a critical task due to the extreme size constraints for each of the four proposed drive units, i.e. electric motor plus planetary gearbox with integrated clutch function, that need to be integrated into the rim of the aircraft wheel.

Two different possible motor locations and their respective envelope within each MLG wheel of an Airbus A320 are presented in [24]. Whereas the

front envelope is located inside the rim on the exterior part of the wheel, a motor in the back can be mounted to the rim on the interior side of the wheel beside the carbon brakes. The back envelope is considered more suitable for this application since it offers a larger outer diameter allowing an integration of an internal planetary gear reduction inside of the motor.

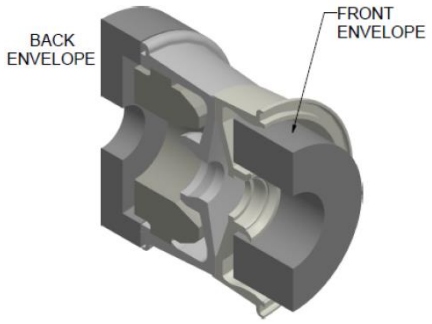

Figure 4-1 – Possible Locations of the Drive Unit within the MLG Wheel [24]

Table 4-1 – Size Constraints and Required Motor Dimensions

Parameter	**Value**
Available Space (Back Envelope)	
Outer Diameter [24]	600 mm
Inner Diameter [24]	151 mm
Axial Length [24]	Approx. 110 mm
Active Motor Dimensions	
Motor Outer Diameter [5]	510 mm
Motor Inner Diameter [6]	315 mm
Motor Axial Length [7]	100 mm

[5] Assumption: 15 % of the maximum available outer diameter is considered for motor housing and cooling.
[6] Assumption: Outer diameter of gearbox (300 mm) plus 5 % left for housing.
[7] Assumption: 10 % of the maximum available axial length is considered for motor housing and cooling.

Although the exact aircraft type is not specified in [24], similar dimensions are assumed for an Airbus A321 (Table 4-1). A gearbox located inside of the electric machine with an outer diameter of 300 mm is assumed. The resulting active motor dimensions, leaving appropriate space for housing and cooling for a conservative design of the motor, are summarized in Table 4-1.

4.1.3 Required Motor Characteristics

The required performance parameters of the motor were defined in section 0. Since the electric taxiing system evaluation on the basis of the developed simulation model showed a positive taxiing performance and thereby confirmed the results of the previous powertrain sizing, the required motor characteristics shown in Table 2-8 need to be satisfied. Besides, a peak efficiency of the motor of 95 % or higher is targeted.

4.2 Analytical Models

4.2.1 Windings

4.2.1.1 Pole-slot combination

The selected motor topology accommodates fraction-slot stator windings which in general suffer from rotor losses due to MMF space harmonic components [52]. Hence, it is required to choose a suitable pole-slot combination in order to minimize the effect of the space harmonics.

The ratio of the number of slots per phase and the number of poles is defined by [51]

$$q = N_s/(3 \cdot 2p) = N_s/6p \tag{35}$$

where p denotes the number of pole pairs and N_S the number of stator segments. Whereas the ratio q is an integer for conventional distributed windings, fractional-slot motor configurations yield a fractional number.

In order to minimize the negative effects of fractional-slot windings, the number of slots should be selected to be close to the number of poles [51], [55].

$$Q \approx 2p \tag{36}$$

Possible pole-slot combinations are:

$$N_s = 2p \pm 1 \text{ or } N_s = 2p \pm 2 \tag{37}$$

where N_S must be divisible by the number of phases m_1 [51], [55].

Besides, the phase shift angle in electrical degrees must equal $\pm 360k + 120$ where k is a positive integer [51]. For a three-phase machine, the phase shift is defined as

$$\theta_{ps} = t_1 \cdot \frac{N_s}{3} \cdot \frac{180}{\tau} \tag{38}$$

where τ corresponds to the average magnet pole pitch angle and $t_1 = 2p\tau/N_s$ to the average slot pitch angle [46]. This results in a phase shift of

$$\theta_{ps} = \frac{2p \cdot \beta_s}{N_s} \cdot \left(\frac{N_s}{3} \cdot \frac{180}{\beta_p} \right) = \frac{360 \cdot p}{3} \tag{39}$$

$2p = N_S \pm 2$ combinations are preferred over $2p = N_S \pm 1$ structures since they have smaller unbalanced magnetomotive forces acting on the stator. The reason for this is the existence of pairs for all coils which are displaced by half a mechanical revolution. $2p = N_S \pm 1$ suffer from stator vibrations and noise due to the asymmetry in the windings that causes unbalanced radial forces acting [56]. Besides providing a very balanced solution in terms of attracting forces,

$N_s = 2p \pm 2$ combinations are characterized by high torque density, low cogging torque and short end windings when coupled with non-overlapping stator windings, leading to low copper losses and high efficiency [57], [58]. Thus, a $N_s = 2p \pm 2$ pole-slot combination is selected for the AFPM machine design.

Double-layer concentrated windings are chosen as described in 3.3. This means that each coil is wound around one tooth. In double-layer windings the number of stator coils equals the number of stator slots, which in this case also equals the number of stator segments:

$$N_c = n_c m_1 = N_{slot} = N_S \tag{40}$$

where N_c corresponds to the number of stator coils, n_c to the number of coils per phase, m_1 is the number of phases and N_{slot} is the number of stator slots [46].

4.2.1.2 Winding factor

The winding factor is defined as the product of the distribution factor and the pitch factor. For the fundamental space harmonic this gives [46]:

$$k_{w1} = k_{d1} \cdot k_{p1} \tag{41}$$

The distribution factor for double-layer, non-overlap windings is expressed as [46]

$$k_{d1} = \frac{\sin\left(\frac{\pi}{2 \cdot m_1}\right)}{z \cdot \sin\left(\frac{\pi}{2 \cdot m_1 \cdot z}\right)}. \tag{42}$$

The number of coils in a coil group is defined by:

$$z = \frac{N_c}{m_1 \cdot F} = \frac{n_c}{F} \tag{43}$$

with the number of pole sections F (periodicity of the machine) which is the greatest common divisor (GCD) of the number poles and the number of coils [46]:

$$F = GCD(2p, N_c). \tag{44}$$

The pitch factor for double-layer slotted iron-cored non-overlap windings can be calculated as [46]

$$k_{p1} = sin\left(\frac{\pi \cdot 2p}{2 \cdot N_s}\right) = \sin\left(\frac{\theta_e}{2}\right) \tag{45}$$

where θ_e denotes the electrical slot pitch angle (also coil span angle in the case of double-layer windings), which is defined by the product of the mechanical slot pitch angle θ_m and the pole pair number [59].

$$\theta_e = \theta_m \cdot p = \frac{\pi \cdot 2p}{N_s} \tag{46}$$

4.2.2 Torque Production

Contrary to radial flux machine, in AFPM machines the torque is produced over a continuum of diameters rather than at a constant diameter. The electromagnetic torque for an idealized double-sided axial flux machine can be calculated from the elementary force which acts on the surface of the stator core:

$$dT_d = r \cdot dF_x \tag{47}$$

where r corresponds to the radius from the center of the machine [46].

The force acting on the machine in tangential direction is defined as

$$\boldsymbol{dF_x} = I \cdot (\boldsymbol{dr} \times \boldsymbol{B_g}) \tag{48}$$

where I denotes the line current, $\boldsymbol{dr}$ is one radius element and $\boldsymbol{B_g}$ is the vector of the magnetic flux density component perpendicular to the disc surface in

the air gap (axial direction). The forces acting in the AFPM machine are illustrated in Figure 4-2.

For an AFPM machine the magnetic flux density in the air gap $\boldsymbol{B_g}$ can be assumed to be constant since it practically does not vary over the the radius r. Thus,

$$dF_x = I \cdot dr \cdot B_{mg} \tag{49}$$

where dF_x expresses the force acting in tangential direction and B_{mg} is the magnetic field acting in axial direction [46].

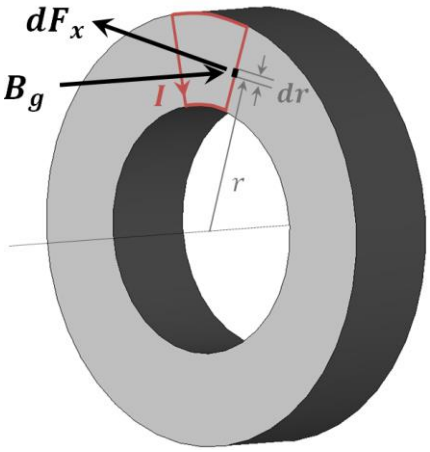

Figure 4-2 – Forces Acting in the AFPM Machine

Subsituting into eqn. (49) into eqn. (47) this gives the average electromagnetic torque

$$dT_d = r(k_{w1} \cdot I \cdot dr \cdot B_{avg}) \tag{50}$$

with $B_{avg} = B_{mg} \cdot \alpha_i$ where α_i is the ratio between the average value B_{avg} and the peak value of the magnetic flux density B_{mg}.

$$\alpha_i = \frac{B_{avg}}{B_{mg}} \tag{51}$$

The ratio α_i can also be expressed as the ratio of the pole width $b_p(r)$ and the pole pitch $\tau(r)$ [46]:

$$\alpha_i = \frac{b_p(r)}{\tau(r)} \tag{52}$$

with

$$\tau(r) = \frac{2\pi \cdot r}{2p} = \frac{\pi \cdot r}{p}. \tag{53}$$

$I_a dr$ can be defined as $A(r)dS$ where $A(r)$ stands for the rms line current density (also called electric loading). This is also a function of the radius r, and can be expressed as

$$A(r) = \frac{m_1 \cdot N \cdot I}{p \cdot \tau(r)} = \frac{m_1 \cdot N \cdot I}{\pi \cdot r}. \tag{54}$$

With the number of turns per phase N and the pole pitch $\tau(r)$ [46]:

$$dT_d = r \cdot \left[k_{w1} \cdot A(r) \cdot dS \cdot B_{avg}\right] \tag{55}$$

With $dS = 2\pi r \cdot dr$ this results in

$$dT_d = r \cdot k_{w1} \cdot A(r) \cdot B_{avg} \cdot 2\pi r \cdot dr \tag{56}$$

Substituting A(r) (eqn. (54)) into eqn. (56) results in

$$\begin{aligned} dT_d &= r \cdot k_{w1} \cdot \frac{m_1 \cdot N \cdot I}{\pi \cdot r} \cdot 2\pi r \cdot dr \cdot B_{avg} \\ &= 2 \cdot k_{w1} \cdot m_1 \cdot N \cdot I \cdot B_{avg} \cdot r \cdot dr \end{aligned} \tag{57}$$

4.2.3 Magnetic Flux

The magnetic flux excited by the PM per pole for a non-sinusoidal magnetic flux density is defined as [46]

$$d\emptyset_f = \int_{R_{in}}^{R_{out}} B_{avg} \cdot \frac{2\pi}{2p} \cdot r \cdot dr \tag{58}$$

An integration of equation (58) with respect to r from R_{in} to R_{out} gives:

$$\begin{aligned} \emptyset_f = B_{avg} \cdot \frac{\pi}{p} \cdot \left[\frac{r^2}{2}\right]_{R_{in}}^{R_{out}} \quad \emptyset_f &= B_{avg} \cdot \frac{\pi}{2p}\left[\left(\frac{D_{out}}{2}\right)^2 - \left(\frac{D_{in}}{2}\right)^2\right] \\ &= B_{avg} \cdot \frac{\pi}{8p} \cdot (D_{out}^2 - D_{in}^2) \end{aligned} \tag{59}$$

4.2.4 Electromagnetic Torque

The average electromagnetic torque is obtained by integrating eqn. (57) from $D_{in}/2$ to $D_{out}/2$ with respect to r.

$$\begin{aligned} T_d &= \int_{D_{in}/2}^{D_{out}/2} 2 \cdot B_{avg} \cdot k_{w1} \cdot m_1 \cdot N \cdot I \cdot r \cdot dr \\ &= 2 \cdot B_{avg} \cdot k_{w1} \cdot m_1 \cdot N \cdot I \cdot \left[\frac{r^2}{2}\right]_{R_{in}}^{R_{out}} \end{aligned} \tag{60}$$

Thus,

$$T_d = B_{avg} \cdot m_1 \cdot I \cdot N \cdot k_{w1} \cdot (R_{out}^2 - R_{in}^2) \tag{61}$$

By substitution the magnetic flux (eqn.(59)) into eqn. (61)**,** the average electromagnetic torque can be expressed by

$$T_d = \emptyset_f \cdot \frac{2p}{\pi} \cdot m_1 \cdot I \cdot N \cdot k_{w1}\,. \tag{62}$$

In order to calculate the rms torque for sinusoidal current and sinusoidal magnetic flux density, eqn. (62) is multiplied by $\pi/\sqrt{2}$:

$$T_{d.rms} = \frac{1}{\sqrt{2}} \cdot \emptyset_f \cdot p \cdot m_1 \cdot I \cdot N \cdot k_{w1} \tag{63}$$

A simplified approach in order to determine the average torque is to calculate the electromagnetic force as the product of the magnetic loading B_{avg}, the rms line current density (electric loading) A at the inner radius r_{in} and the active surface of the magnets S [46]:

$$F_x = B_{avg} \cdot A(R_{in}) \cdot S. \tag{64}$$

With $S = 2\pi \cdot (R_{out}^2 - R_{in}^2)$ for a double-sided AFPM machine[8], the average torque can be determined.

$$T_d = F_x \cdot R_{in} = B_{avg} \cdot A(R_{in}) \cdot 2\pi \cdot (R_{out}^2 - R_{in}^2) \cdot R_{in} \tag{65}$$

The ratio between the inner PM radius and the outer PM radius is defined as [46]

$$k_d = \frac{R_{in}}{R_{out}}. \tag{66}$$

Thus, the average electromagnetic torque can also be written as

$$T_d = B_{avg} \cdot A \cdot 2\pi \cdot R_{out}^3 (k_d - k_d^3). \tag{67}$$

The optimum ratio for maximum torque can be obtained by deriving this equation with respect to k_d and equating this term to zero.

$$0 = (B_{avg} \cdot A \cdot 2\pi \cdot R_{out}^3) \cdot (1 - 3k_d^2) \tag{68}$$

$$k_d = \sqrt{1/3} = 0.58 \tag{69}$$

[8] The factor two considers the surface of two rotors.

However, industrial applications show a maximum torque with $k_d \neq \sqrt{1/3}$ [46].

4.2.5 Back EMF

The back EMF can be expressed as

$$e_f = N \cdot k_{w1} \cdot \frac{d\emptyset_{f1}}{dt} = \omega \cdot N \cdot k_{w1} \cdot \emptyset_f \cdot \cos(\omega t) \tag{70}$$

where $\emptyset_{f1} = \emptyset_f \cdot \sin(\omega t)$ is the first harmonic of the magnetic flux waveform [46]. With the angular frequency $\omega = 2\pi \cdot f$ one obtains

$$e_f = 2\pi \cdot f \cdot N \cdot k_{w1} \cdot \emptyset_f \cdot \cos(\omega t). \tag{71}$$

The rms value of the back EMF can be calculated by

$$E_f = \pi \cdot \sqrt{2} \cdot f \cdot N \cdot k_{w1} \cdot \emptyset_f = \pi \cdot \sqrt{2} \cdot p \cdot n \cdot N \cdot k_{w1} \cdot \emptyset_f \tag{72}$$

with $f = p \cdot n$ where f is the frequency in Hz, p is the number of pole pairs and n is the rotational speed in s^{-1} [46].

4.2.6 Permanent Magnet Length

The magnetic flux density in the air gap can be approximated by [46]

$$B_{mg} \approx \frac{B_{r,pm} \cdot l_{pm}}{l_{pm} + \mu_{r,pm} \cdot l_g} = \frac{B_{r,pm}}{1 + \frac{\mu_{r,pm} \cdot l_g}{l_{pm}}} \tag{73}$$

where $B_{r,pm}$ denotes the remanence of the magnets, l_{pm} is the axial length of the magnets, l_g is the axial length of the air gap, $\mu_{r,pm}$ is the relative permeability of the PM, which is the ratio between the magnetic permeability of the PM μ_{pm} and the magnetic permeability of free space/air μ_0.

$$\mu_{r,pm} = \frac{\mu_{pm}}{\mu_0} \tag{74}$$

The required axial length of the PM l_{pm} can be derived from eqn. (73).

$$l_{pm} = \frac{\mu_{r,pm} \cdot l_g}{\frac{B_{r,pm}}{B_{mg}} - 1} \tag{75}$$

4.2.7 Rotor Core Length

By neglecting leakage flux and induced flux, the magnetic flux acting in the rotor can be calculated by

$$\emptyset_{rc} = B_{rc} \cdot A_r = B_{rc} \cdot l_{rc} \cdot \frac{D_{out} - D_{in}}{2} \tag{76}$$

where B_{rc} is the magnetic flux density in the rotor core, A_r is the cross-sectional area of the rotor core in x-direction and l_{rc} is the axial length of the rotor core (Figure 4-3).

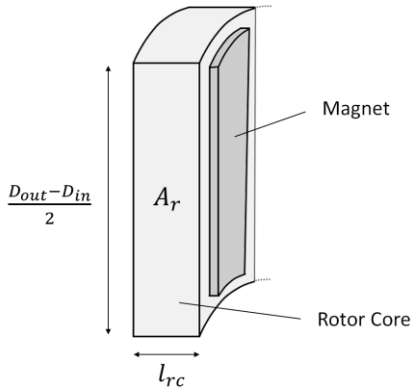

Figure 4-3 – Rotor Dimensions

By re-arranging eqn. (76) the length of the rotor can be determined.

$$\emptyset_{rc} = B_{rc} \cdot A_r = B_{rc} \cdot l_{rc} \cdot \frac{D_{out} - D_{in}}{2} \tag{77}$$

Since half of the magnetic flux in the air gap travels through the rotor core in positive x- direction and the other half in negative x- direction (Figure 3-5), the magnetic flux in the rotor core can be determined by

$$\emptyset_{rc} = \frac{\emptyset_f}{2} \tag{78}$$

where $\emptyset_f$ is the air gap flux per pole. Thus,

$$l_{rc} = \frac{\emptyset_f}{B_{rc} \cdot (D_{out} - D_{in})} \tag{79}$$

Similar to eqn. (59), the magnetic flux in the air gap $\emptyset_f$ can be written as

$$\emptyset_f = B_{avg} \cdot A_{pole} = B_{avg} \cdot \frac{\pi}{8p} \cdot (D_{out}^2 - D_{in}^2) \tag{80}$$

where the area of one pole is $A_{pole} = \frac{\pi}{8p}(D_{out}^2 - D_{in}^2)$. Substituting this into eqn. (79) with $B_{avg} = B_{mg} \cdot \alpha_i$ (eqn. (51)) this gives

$$l_{rc} = \alpha_i \cdot \frac{B_{mg}}{B_{rc}} \cdot \frac{\pi}{8p} \cdot D_{out}(1 + k_d) \tag{81}$$

4.2.8 Stator Segment Dimensions

The stator of the AFPM machine is represented by twelve stator segments. Each stator segments contains out of one central bar and two stator shoes. The windings are wound around the central bar, whereas the purpose of the stator shoes is to increase the active area of the coils, i.e. maximize the active air gap area. Hence, the shoes are wider in both the radial and tangential direction in

order to overlap the windings. A schematic figure of a stator segment is shown in Figure 4-4.

Such geometries can be realized by using soft magnetic composite (SMC) material. By pressing SMC, complicated shapes of the stator segments can be created which allows an ease of manufacturing and a reduction of iron material in the stator [46], [60]. The material selection for the stator segments and the advantages of using SMC for the selected motor topology are discussed more detailed in section 4.3.3.

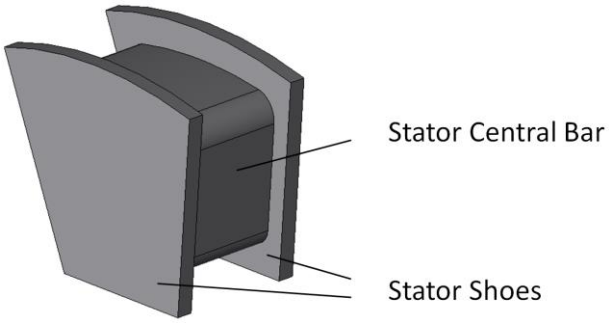

Figure 4-4 – Components of a Stator Segment

4.2.8.1 Stator Central Bar Dimensions

The magnetic flux in the central bar of one stator segment can be expressed by

$$\emptyset_s = B_s \cdot A_{sc} \tag{82}$$

where B_s denotes the magnetic flux density in the stator and A_{sc} is the cross-sectional area of the stator central bar. Since the magnetic flux in the stator central bar should equal the magnetic flux in the air gap (eqn. (72)) it can be assumed that

$$\emptyset_s = \emptyset_f = B_{avg} \cdot \frac{\pi}{8p} \cdot (D_{out}^2 - D_{in}^2) = B_{mg} \cdot \alpha_i \cdot \frac{\pi}{8p} (D_{out}^2 - D_{in}^2) \quad (83)$$

This results in the required cross-sectional area of the stator central bar:

$$A_{sc} = \frac{\emptyset_s}{B_s} = \alpha_i \cdot \frac{B_{mg}}{B_s} \cdot \frac{\pi}{8p} \cdot D_{out}^2 (1 - k_d^2) \,. \quad (84)$$

Due to the absence of the stator core yoke in the selected topology the length of the stator central bar is dependent on the required amount of copper in the motor. Hence, the length of the central bar can be obtained by the axial length of the stator windings.

$$l_{sc} = l_w \quad (85)$$

4.2.8.2 Stator Winding Dimensions

The winding area A_w can be expressed as

$$A_w = w_w \cdot l_w \quad (86)$$

where w_w expresses the width and l_w the axial length of the winding (Figure 4-5).

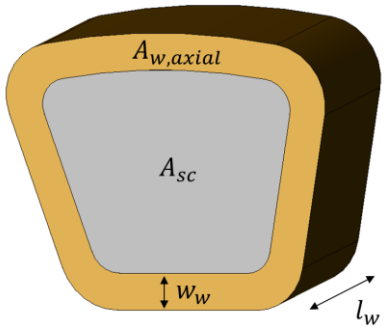

Figure 4-5 – Geometry of Stator Winding and Central Bar

The copper fill factor is defined by the ratio between the required copper area A_{cu} and the area that is available A_w for the stator windings.

$$K_{cu-fill} = \frac{A_{cu}}{A_w} \tag{87}$$

where A_{cu} is the total (required) copper area of the stator windings [52]. The copper area can be expressed as

$$A_{cu} = N \cdot \pi \cdot r_{c,bare}^2 = N \cdot \frac{\pi}{4} \cdot d_{c,bare}^2 \tag{88}$$

where N denotes the number of conductors (or turns) and $d_{c,bare}$ is the bare diameter of the conductors, i.e. diameter without insulation.

4.2.8.3 Cross-Sectional Area of Stator Segments

The total cross-sectional area of each stator segment A_s, i.e. stator central bar area A_{sc} plus axial winding area $A_{w,axial}$, needs to be smaller than the area available for each stator segment.

$$A_s = A_{sc} + A_{w,axial} \leq A_{stator\ pole} = \frac{A_{gap}}{N_s} = \frac{\pi}{4 \cdot N_s} \cdot (D_{out}^2 - D_{in}^2) \tag{89}$$

Here, the axial cross-sectional area of the windings is dependent on the shape of the stator central bar and the winding width.

4.2.9 Motor Length

The total axial length of the motor can now be determined by

$$l_{tot} = 2 \cdot (l_{rc} + l_{pm}) + 2 \cdot l_g + 2 \cdot l_{shoe} + l_{sc} \tag{90}$$

where l_{shoe} is the length of one stator shoe.

4.2.10 Efficiency

In order to assess the efficiency of the AFPM machine the losses need to be calculated. The motor efficiency is defined by

$$\eta = \frac{P_{out}}{P_{in}} \tag{91}$$

where P_{out} and P_{in} are the output power (shaft power) and the input power (electrical power) of the motor, respectively [46].

The input power is calculated by adding the losses to the output power:

$$P_{in} = P_{out} + \Delta P_{loss} \tag{92}$$

The total motor losses ΔP_{loss} can be determined as follows:

$$\Delta P_{loss} = \Delta P_w + \Delta P_{1Fe} + \Delta P_{2Fe} + \Delta P_{PM} + \Delta P_e + \Delta P_{rot} \tag{93}$$

where ΔP_w expresses the winding losses (copper losses), ΔP_{1Fe} are the stator core losses, ΔP_{2Fe} are the rotor core losses, ΔP_{PM} are the losses in the PMs, ΔP_e are the eddy current losses in the stator conductors and ΔP_{rot} are the rotational losses [46].

In general, eddy current losses induced in the conductors should be considered for slotless AFPM machines. However, they can be neglected for slotted AFPM machines [46]. Thus,

$$\Delta P_e = 0 \tag{94}$$

The electromagnetic torque P_{elm} is the torque that is generated by the electromagnetic forces in the machine, whereas the output torque P_{out} considers additional mechanical losses (rotational losses) that are caused by friction losses in the bearings and windage losses due to the viscosity of the cooling fluid [46].

The shaft power (mechanical power) P_{out} can be determined by subtracting the rotational losses ΔP_{rot} from the electromagnetic output power P_{elm} [46].

$$P_{out} = P_{elm} - \Delta P_{rot} \tag{95}$$

The electromagnetic power P_{elm} is calculated as the product of the average of the electromagnetic torque and the rotational motor speed.

$$P_{elm} = T_{elm} \cdot \omega = T_{elm} \cdot 2\pi \cdot n \tag{96}$$

where ω denotes the angular velocity and n is the rotational velocity.

4.2.10.1 Iron Losses

Iron losses occur in the stator iron and in the rotor iron. They are further classified in

- Eddy current losses
- Hysteresis losses
- Excess losses

Eddy current losses (or Joule losses) are caused by eddy currents in the iron material. Hysteresis losses on the other hand are the losses produced by magnetic hysteresis. Excess losses, i.e. additional core losses that can be present due to magnetic anomaly, are neglected.

Hence, the iron losses in stator and rotor ΔP_{1Fe} and ΔP_{2Fe} can be calculated by the sum of the hysteresis losses $\Delta P_{Fe,h}$ and eddy current losses $\Delta P_{Fe,e}$.

$$\Delta P_{1Fe} = \Delta P_{1Fe,e} + \Delta P_{1Fe,h} \tag{97}$$

$$\Delta P_{2Fe} = \Delta P_{2Fe,e} + \Delta P_{2Fe,h} \tag{98}$$

Predicting iron losses can become a very complex topic. Many analytical methods have been developed in order to analyse iron losses for AFPM machines, for instance in [46]. In this thesis, the iron losses are computed with three-dimensional finite element analysis (3D FEA).

4.2.10.2 Copper Losses

Stator winding losses, also called copper losses, are the losses generated by Joule heating in the stator windings. They are dependent on the current I flowing in the conductor the resistance of the conductor R_1 and the number of phases m_1:

$$\Delta P_w = m_1 \cdot I^2 \cdot R_1 \approx m_1 \cdot I^2 \cdot R_{1,dc} \cdot k_1 \tag{99}$$

where $R_1 \approx R_{1,dc} \cdot k_1$ is the winding resistance which considers the skin-effect coefficient k_1, that compensates for temperature and the content of harmonics [46]. Neglecting the skin-effect for the stator coils one obtains [46]:

$$R_1 \approx R_{1,dc} \tag{100}$$

The stator winding resistance is given by

$$R_{1,dc} = \frac{N \cdot l_{avg}}{a_p \cdot a_w \cdot \sigma \cdot A_c} \tag{101}$$

in which N_1 is the number of turns per stator winding, l_{avg} denotes the average length of the conductors, a_p is the number of current paths in parallel, a_w is the number of conductors in parallel, σ is the electric conductivity of the conductor and also the inverse of the electric resistivity ($\sigma = 1/\rho$), and A_c is the cross-sectional area of the conductor [46].

The change of resistance due to temperature increased during the motor operation can be determined by

$$R(T) = R_0 \cdot [1 + \alpha\,(T - T_0)] \tag{102}$$

where α is the temperature coefficient, T_0 is the reference temperature and R_0 is the resistance at temperature T_0 [61].

4.2.10.3 Permanent Magnet Losses

Eddy currents are induced in the magnets due to the interaction between the moving rotor field and the stationary field of the stator [49]. The reason for the eddy current losses in the magnets is that the stator produces higher harmonic magnetic fields than the magnets itself. The electric conductivity of copper conductors is only 4 to 9 times higher than that of rare earth PMs. Hence, the losses in conductive magnets need to be considered as well [46]. The eddy current losses in the PM material can be determined by using FEA.

4.2.10.4 Rotational Losses

Rotational losses (or mechanical losses) in an electric machine refer to mechanical friction between motor components causing losses. These include friction losses (bearing losses) that are induced in the bearings and windage losses which are defined as the resistance between the cooling fluid and rotating motor parts [61].

$$\Delta P_{rot} = \Delta P_{fr} + \Delta P_{wind} \tag{103}$$

The windage losses are defined as [46]

$$\Delta P_{wind} = \frac{1}{2} c_f \rho (2\pi n)^3 \left(R_{out}^5 - R_{in}^5\right) \tag{104}$$

where c_f denotes the coefficient of friction (friction coefficient), ρ the specific density of the cooling medium and R_{in} and R_{out} express the inner and outer radius of the rotor disc, respectively.

The coefficient of friction for turbulent flow can be determined by [46]

$$c_f = \frac{3.87}{\sqrt{Re}}. \tag{105}$$

The Reynolds number for a rotating disc can be written as [46]

$$Re = \rho \frac{R_{out} \cdot v}{\mu} = \frac{2\pi n \rho R_{out}^2}{\mu} \tag{106}$$

where μ is the dynamic viscosity of the fluid and $v = 2\pi R_{out} n$ is the linear velocity at the outer radius and n is the rotational speed.

Assuming air cooling in the rotor the dynamic viscosity and the density of the cooling medium parameters become [46]:

$$\mu_{air}(20°C) = 1.8 \cdot 10^{-5} Pa \cdot s \tag{107}$$

$$\rho_{air}(20°C) = 1.2 \frac{kg}{m^3}. \tag{108}$$

The friction losses in bearings (bearing losses) are negligible small compared to other available losses. Thus, in this work they are assumed as

$$\Delta P_{fr} \approx 0 \tag{109}$$

4.2.11 Sizing Equations

The rms line current density $A(r)$ was already introduced in eqn. (54). The peak line current density can be determined by [46]

$$A_m(r) = \sqrt{2} \cdot A(r) = \frac{\sqrt{2} \cdot m_1 \cdot N \cdot I}{\pi \cdot r}. \tag{110}$$

In order to calculate the peak line current density at the average radius, the radius in the equation above can be replaced by the average radius which is defined as

$$R_{avg} = \frac{R_{out} + R_{in}}{2} = \frac{D_{out} + D_{in}}{4}. \tag{111}$$

Thus,

$$A_m(R_{avg}) = \frac{4 \cdot \sqrt{2} \cdot m_1 \cdot N \cdot I}{\pi \cdot D_{out}(1 + k_d)}. \tag{112}$$

Substituting the magnetic flux (eqn. (59)) into the rms value of the back EMF per phase in each in winding (eqn. (72)), the back EMF can be expressed as

$$E_f = \frac{\pi^2}{8} \cdot \sqrt{2} \cdot n \cdot N \cdot k_{w1} \cdot B_{avg} \cdot D_{out}^2(1 - k_d^2). \tag{113}$$

The apparent electromagnetic power for a double-sided AFPM machine with a single-stator is defined by [46]

$$S_{elm} = m_1 \cdot E_f \cdot I. \tag{114}$$

Substituting E_f (eqn. (113)) into eqn. (114) this gives

$$S_{elm} = \frac{\pi^3}{32} \cdot k_{w1} \cdot n \cdot A_m \cdot \alpha_i \cdot B_{mg} \cdot D_{out}^3(1 + k_d)(1 - k_d^2). \tag{115}$$

The electromagnetic torque T_d can be calculated based on the active power and the rotational motor speed.

$$T_d = \frac{P_{elm}}{2\pi \cdot n} \tag{116}$$

The active power is defined by

$$P_{elm} = S_{elm} \cdot cos\Psi \tag{117}$$

where Ψ is th angle between the stator current and EMF E_f [46]. This also shows that the active power is maximized (equals the apparent power) if the stator current and E_f are aligned.

Consequently, the torque equation becomes

$$T_d = \frac{\pi^2}{64} \cdot k_{w1} \cdot A_m \cdot \alpha_i \cdot B_{mg} \cdot D_{out}^3 (1 + k_d)(1 - k_d^2) \cdot cos\Psi \, . \qquad (118)$$

4.3 Analytical Design

The design of the AFPM machine is structured into the following two general steps:

- Step 1: Analytical design
- Step 2: Design and analysis by using three-dimensional finite element analysis (3D FEA)

Due to the complex 3D effects of the magnetic flux paths in the AFPM machine, 3D FEA is required to analyse the machine performance accurately. However, 3D FEA requires a lot of computing time. Hence, the previously presented analytical models are used to determine the main dimensions of the AFPM machine in order to reduce the number of time consuming FEA simulations. In the subsequent FEA analysis (section 4.4) the designed motor geometry is evaluated and improved to increase the motor performance.

In this section the analytical design procedure for the proposed AFPM machine is described.

4.3.1 Selection of Number of Pole Pairs and Stator Segments

The advantages of the selected $N_s = 2p \pm 2$ pole-slot combination have been presented in section 4.2.1.1. In particular, a topology with 12 stator segments and 5 pole pairs is chosen.

$$N_S/2p = 12/10 \tag{119}$$

Based on eqn. (41), the winding factor of the selected motor topology becomes

$$k_{w1} = 0.933\,. \tag{120}$$

4.3.2 Winding Configuration

Based on eqn. (39) the slot pitch angle (or coil span angle) can be calculated, which yields the phase displacement of the induced back EMF in the stator windings (electrical degrees):

$$\theta_e = \frac{\pi \cdot 2p}{N_s} = 2.618\ [rad] \equiv 150°. \tag{121}$$

The phase displacement of the induced back EMF can also be obtained by plotting the derivative of the magnetic flux in each winding. The space vector plot of the induced back EMF in the stator windings are displayed in Figure 4-6.

The windings are connected in series. The vectors are grouped into a three-phase set and arranged into a winding scheme that provides the greatest magnitude of the back voltage per phase. Figure 4-7 the shows vector sum of the voltages in each of the twelve coils. In the selected winding scheme, the two coils that form a pair are displaced by 180 mechanical degrees ($\theta_e = 180°$), providing a solution with balanced axial attracting forces. The winding arrangement of the selected configuration is displayed in Figure 4-8.

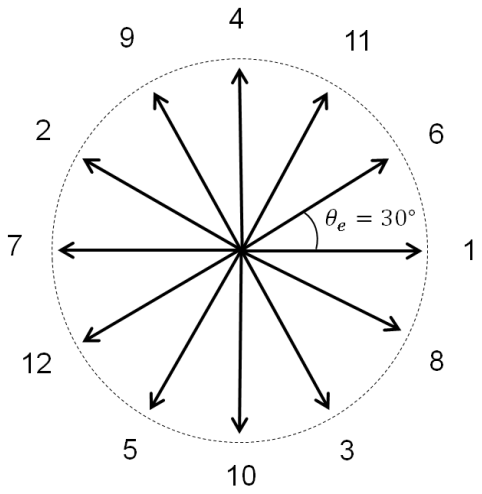

Figure 4-6 – Phase Displacement of the Induced Back EMF – Space Vector Plot

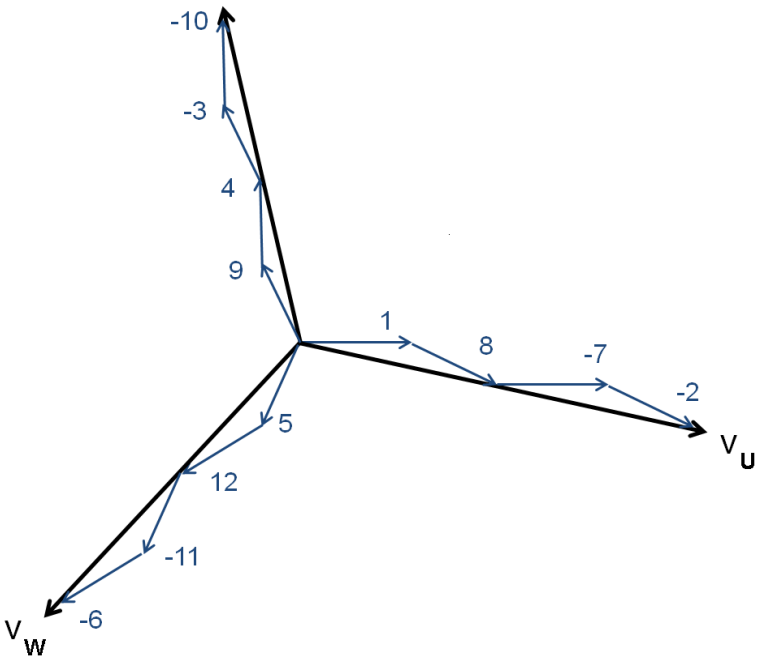

Figure 4-7 – Vector Sum of the Voltages in Each Coil

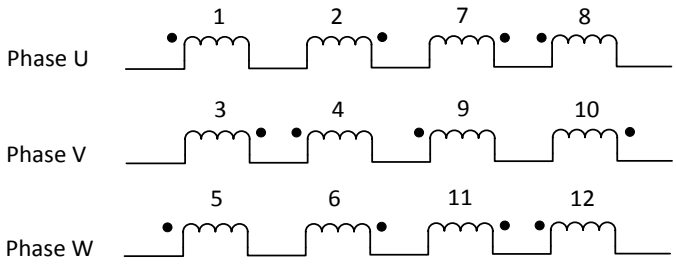

Figure 4-8 – Stator Winding Arrangement

4.3.3 Material Selection

4.3.3.1 Stator Segments

As described in section 4.2.8, the complicated geometry of the stator segments, i.e. stator central bar and shoes, can be manufactured by the use of pressed SMC material [46] [60]. This is important since steel laminations for AFPM machines are more difficult to manufacture than those for RFPM machines. Also, by using powdered iron material, the stator shoes can overlap the windings to maximize the active area of the air gap. Thus, the amount of iron material can be reduced yielding a high torque density [46], [49], [62].

SMC is advantageous particularly at medium- or high-speed applications due to low losses since low eddy currents are generated at higher frequencies [63]. Another advantage over laminated steel is that SMC allows an arbitrary flux distribution can be developed within the magnetic core (isotropic characteristic) [64]. This is very important for the proposed design since the flux in the stator segments is distributed in three-dimensional directions. Whereas the flux paths in the stator central bars occurs mainly in axial direction only, the stator shoes experience a three-dimensional flux distribution in axial, radial and tangential direction which can be realized an SMC material with isotropic characteristics. The three-dimensional effects of the flux distributed in the stator segments are visualized in Figure 4-18. In order to simplify the production process (avoid

bonding of two different materials), SMC is selected for the entire stator segments, i.e. stator central bar and shoes.

The B-H curve of the chosen iron material, Somaloy 550 from "Höganäs AB" ("Somaloy 550+0.6 %-LB1-WC-800 MPa" in particular), is shown in Figure 4-9. This SMC is produced under a high compacting pressure of 800 MPa and 500°C treating temperature, resulting in high magnetic flux densities [65], [66].

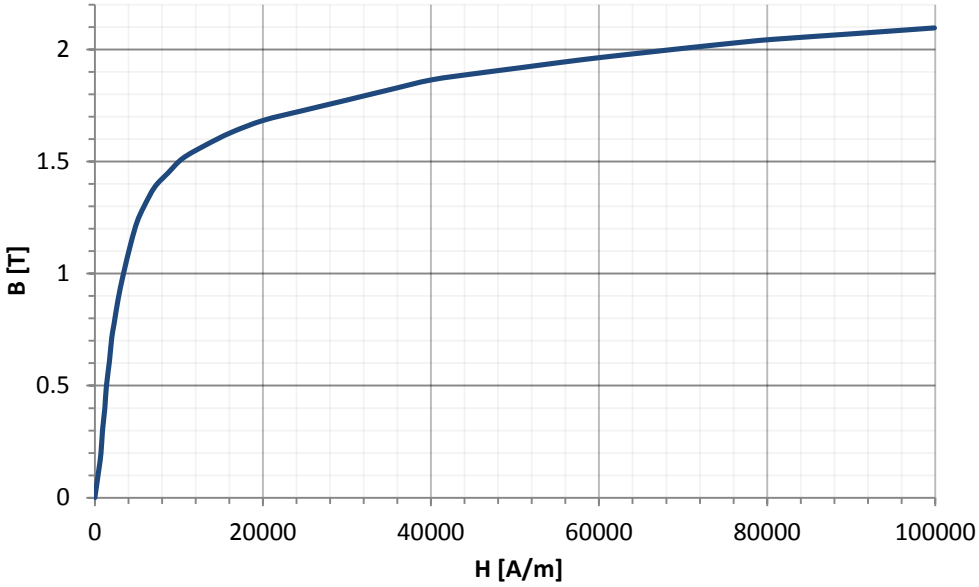

Figure 4-9 – B-H Characteristics of SMC Material (Somaloy 550)

4.3.3.2 Rotor Core

Since the three-dimensional effects of the flux distribution in the rotor core are negligibly low in the rotor core the rotor disc can be made out of conventional laminated steel or SMC. The main drawback of SMC is the lower permeability and lower saturation flux density comparing to laminated steel [48], [52]. AFPM motors with segmented SMC stator segments and rotor discs accommodating steel laminations are presented in [49] and [67]. It was shown that

high torque capabilities can be achieved with such solutions. A comparison of AFPM machines with different rotor back core materials is presented in [68] and [69]. It was found that the use of a laminated steel rotor used for the same topology with a SMC stator provides a higher torque density than a SMC rotor. Furthermore, it was found that steel laminations provide less eddy current losses than SMC material leading to a higher motor efficiency.

In this thesis, 50JN400 steel (JFE steel) is selected for the steel laminations in the rotor. In particular, cylindrical laminations (also called spiral laminations) are chosen since they allow very low eddy currents [47], [70]. Thereby, the iron losses in the rotor can be reduced.

4.3.3.3 Permanent Magnets

Axially magnetized sintered Neodymium-Iron-Boron (NdFeB) permanent magnets are used that are mounted on the surface of the rotor core. The chosen material NEOMAX-42-AH (Hitachi Metals) offers good B-H characteristics, in particular high magnetic loadings.

4.3.4 Design of Geometry for Maximum Torque

4.3.4.1 Motor Outer Dimensions (Diameter Ratio)

The maximum allowable outer dimensions (size constraints) of the AFPM machine were given in Table 4-1. As shown previously, a maximum torque can theoretically be obtained with a ratio between the inner and outer machine diameter of $k_d = 0.58$ (eqn. (69)). Several studies have been done in order to achieve the optimum ratio for the highest torque density [70]. In this thesis, the maximum available dimensions will be used for the design to maximize the torque capability of the proposed AFPM motor. The resulting diameter ratio is close to the optimum value based on the theory:

$$k_d = \frac{315\ mm}{510\ mm} = 0.62 \tag{122}$$

4.3.4.2 Design for Maximum Electromagnetic Torque

To obtain the motor's maximum possible electromagnetic torque or power, respectively, eqns. (115) and (118) should be maximized. This is done by maximizing the product of the magnetic loading B_{mg} and the electric loading A_m. However, since both magnetic flux density and current density are limited due to saturation, a high utilization of the iron material and the copper in the stator windings is aimed to increase the performance of the motor.

4.3.4.3 Design Constraints

The magnetic loading and the electric loading are constrained by the saturation limit of the selected iron material and the maximum current density, respectively.

The saturation limit of the chosen SMC material in the stator segments (Somaloy 550) according to Figure 4-9 is

$$B_{SMC,sat} = 2.1\ T\ . \tag{123}$$

For sizing the main dimensions, a maximum magnetic flux density within the saturation limit is chosen:

$$B_{SMC,max} = 1.9\ T. \tag{124}$$

The saturation limit of the steel used for the laminations in the rotor back iron (50JN400) has a similar saturation limit $\left(B_{steel,sat} \approx 2.1\ T\right)$ as the chosen SMC material. Thus, the maximum flux density for the design is selected as

$$B_{steel,max} = 1.9\ T. \tag{125}$$

The magnetic air gap flux density for AFPM machines is relatively small compared to their radial flux counterparts due to the large air gap between stator and rotor [46]. The maximum flux density in the air gap needs to be obtained by using three-dimensional finite element analysis. This makes the sizing process of the main components of the motor an iterative process since the air gap flux density is not known prior to the machine design. The air gap flux density for the final geometry was calculated as

$$B_{avg} = 0.6\,T\,. \tag{126}$$

The current density in the stator is defined as

$$J = \frac{I}{a_w \cdot A_{cu,wire}} \tag{127}$$

where a_w is the number of conductors in parallel and A_c is the cross-sectional area of the stator conductor (one wire).

An aggressive cooling is needed to match the high torque density requirements of the motor for the electric taxiing system. The coolant, which could be water, oil or any other cooling fluid, is not specified in this thesis. The maximum current density is assumed as

$$J = 16\frac{A}{mm^2} \tag{128}$$

An equal current density was used for a similar AFPM motor topology in [49].

4.3.4.4 Copper Fill Factor

The copper fill factor is the ratio between the required copper area A_{cu} and the available area A_w (eqn. (87)). It has a significant impact on the main dimensions of the design, in particular the dimensions of the stator segments. The

copper slot fill factor needs to be selected small enough to ensure that the stator can be wound. In general, segmented stator structures with fractional-slot concentrated windings have higher slot fill factors than conventional machines [52]. It has been presented in [52] and [71] that machines accommodating a SMC stator can enable very high copper fill factors of up to 78 %, for instance by using prepressed windings. For a conservative design a fill factor of $K_{cu-fill} = 60$ % is selected for the proposed AFPM machine.

4.4 Finite Element Analysis

4.4.1 Model and Implementation

The AFPM motor is modeled and investigated with a transient magnetic field analysis in 'JMAG-Designer' [66]. A three-dimensional (3D) simulation model is used for the designed motor. 3D analysis is more accurate than 2D FEA analysis and analytical design since it uses integral or partial differential equations, which allows solving complicated problems. This is required to take into account the complex three-dimensional effects of the magnetic flux paths available in the AFPM machine as described in section 4.3.3.1.

4.4.1.1 Symmetry Conditions

To safe computation time one half of the motor is reduced by symmetry conditions. From eqn. (44) the greatest common divisor of $2p = 10$ and $N_s = 12$ is known as 2. Thus, by using an antiperiodic condition, i.e. the magnetic flux reverses, the full motor model with the chosen pole-slot combination can be represented while decreasing simulation time. The analysis model is shown in Figure 4-10.

The reduced motor model has been verified by using the complete motor model to ensure the fidelity of the obtained analysis results.

4.4.1.2 Stator Windings

For simplification purposes the windings in the stator are modeled as solid objects rather than modeling each wire separately. In this context, it is assumed that each turn in the coils carries the same current. In the cross section of the windings, a surface area is defined where the current is equally induced in normal direction. Thus, the current density is evenly distributed over the entire cross-sectional area of each winding.

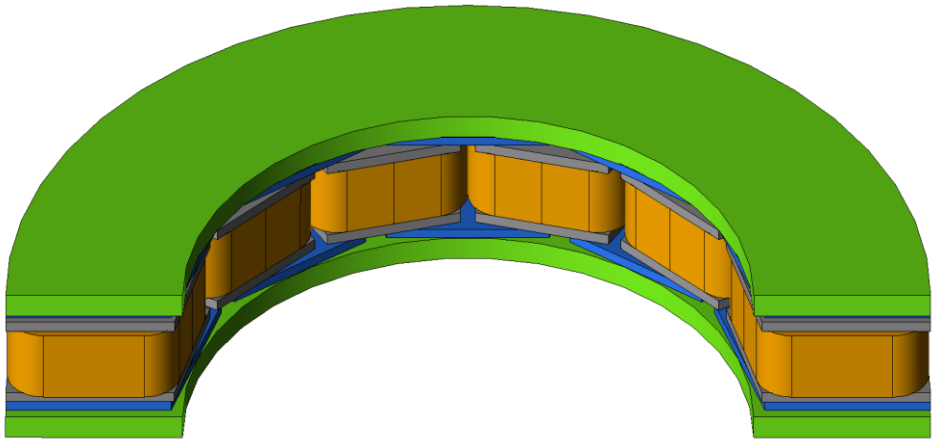

Figure 4-10 – Reduced 3D-Simulation Model

4.4.1.3 Materials

The materials for each component are selected as presented in section 4.3.3. The material properties for each of those materials are already defined in JMAG-Designer. Thus, no additional editing of existing B-H-curves or loss characteristics needs to be done.

The behavior of the NdFeB magnets is distinctly influenced by the available temperature. An operation temperature of 100°C is assumed for the AFPM motor. This yields a relative permeability of $\mu_{r,pm} = 1.2$ and a coercivity of $H_c = 910\ kA/m$. [66].

4.4.2 Design of Geometry for Maximum Performance

4.4.2.1 Electromagnetic Torque and Power

Similar to the analytical design (section 4.3.4) the aim of the design process by using FEA is the finding of the geometry providing a maximum torque and power respectively under consideration of the given constraints. After analytically determining the main dimensions in stator and rotor, the geometry is evaluated and improved to increase the performance of the AFPM machine without exceeding the limits of the chosen materials.

Besides achieving the maximum possible torque and power, a decreased torque ripple is aimed during the design process to ensure an optimum motor performance for the electric taxiing system.

Transient simulations are performed to investigate the motor performance for various operation points. Thereby, the torque vs. speed curve can be generated, providing the maximum torque and maximum power envelope of the AFPM machine as shown in section 4.5.1.7. In the field weakening region the phase voltage is controlled by varying the excitation angle (phase shift) in the current source which allows operating the motor at high speeds beyond the rated speed without exceeding the given phase voltage.

4.4.2.2 Losses and Efficiency

Besides achieving a high torque and high power output, the losses in stator and rotor are an important factor affecting the design process. For various operation points within the torque and power limits the losses and the resulting efficiency are obtained with transient simulations. The joule losses in magnets and copper can directly be evaluated from a 3D transient magnetic field analysis. The iron losses in stator and rotor (joule loss and hysteresis loss) are assessed in a further loss study based for the respective operation frequency. In combination

with the analytically calculated rotational losses, the efficiency map of the motor can be generated (Figure 4-26).

4.4.2.3 Permanent Magnet Laminations (Rotor Eddy Currents)

Eddy currents losses are induced in the surface-mounted magnets in the rotor. To reduce these losses it is required to add laminations which cut the eddy current paths inside the magnets. Thus, separated magnets are implemented which are electrically isolated with an insulation epoxy (coating). In the FEA model the magnets are modeled as solid bodies. The effect of PM laminations is modeled in JMAG by using an insulation condition applied on the surface between two adjacent magnets. This condition prevents the eddy current from flowing between the respective magnets. Several designs with different laminations have been compared and are presented in section 4.5.1.1.

4.5 Results and Discussion

4.5.1 Results

4.5.1.1 Eddy Currents in Permanent Magnets

It has been found that the magnet losses induced by eddy currents in the permanent magnets are very large, leading to heat generation in the rotor. The analysis results show that the magnet losses can be significantly decreased by adding PM laminations, i.e. separating the magnets into electrically isolated segments. Various designs with different numbers of magnet laminations have been evaluated. The distribution of the eddy currents at 450 A rms current at 3000 rpm for three different designs, in particular a design without PM laminations, one with 4 laminations (5 magnet segments) and one with 19 laminations (20 segments), is presented in Figures 4-11 to 4-13, respectively. It is noticeable that the eddy current density can be decreased significantly. For instance, the

maximum eddy current density with 19 laminations is about 50 % lower than without laminations (Figure 4-13).

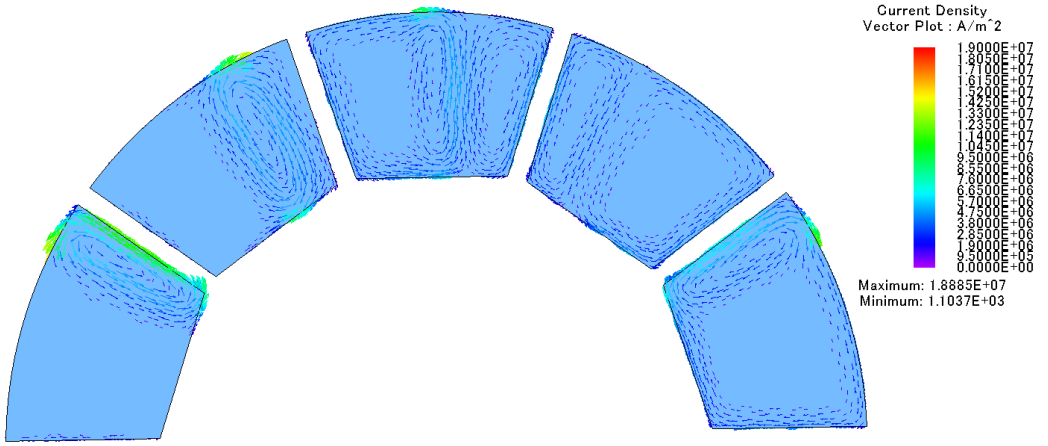

Figure 4-11 – Eddy Current Density Distribution in Magnets – No Laminations

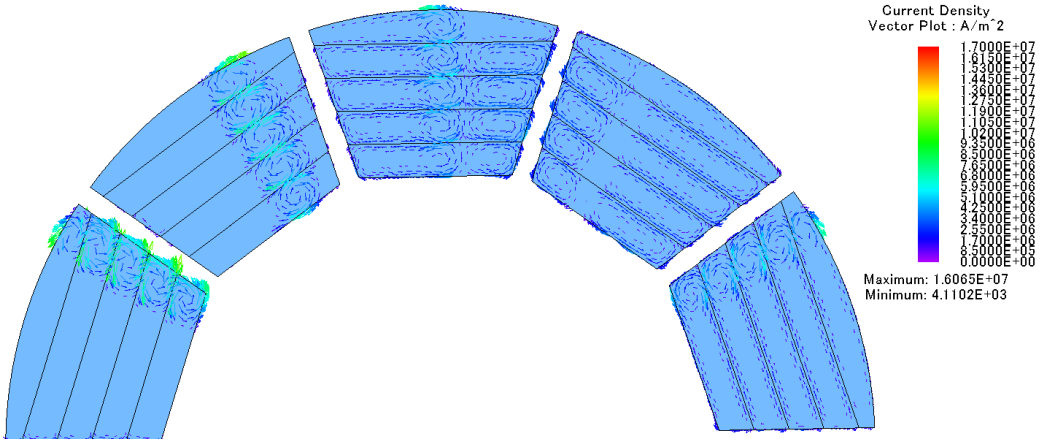

Figure 4-12 – Eddy Current Density Distribution in Magnets – 4 Laminations

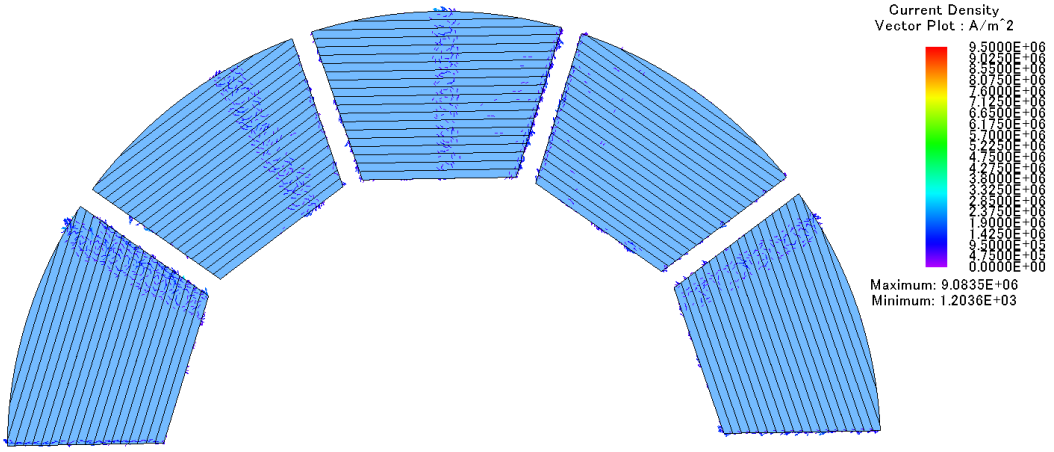

Figure 4-13 – Eddy Current Density Distribution in Magnets – 19 Laminations

The highest eddy current losses in the magnets are generated at maximum speed (3000 rpm) and maximum current (450 A rms). An investigation of different segmentation methods with varied PM segment shapes has shown that the lamination in radial direction as presented in Figure 4-13 has the greatest impact on the reduction of eddy current losses, rather than laminations in circumferential direction or the combination of radial and circumferential segmentation.

Due to the reduced eddy currents, the losses in the rotor can be decreased drastically. Whereas the non-laminated design (massive magnets) yields a total magnet loss of 59.393 kW for the two rotors, the losses can be reduced to about 781 W by splitting each of the magnets into 40 segments (Figure 4-14). However, a segmentation of the magnets attached to the rotor core is limited due to manufacturing processes. High numbers of PM laminations might lead to assembling difficulties. Thus, designs with numbers of segments higher than 20 are not further considered in this work. A final rotor design with 20 separate magnet segments in each of the 10 magnets per rotor is selected. This solution allows a reduction of the magnet losses down to 1957.23 W, i.e. 978.62 W per

rotor. The manufacturing of the laminations for this solution is considered as feasible.

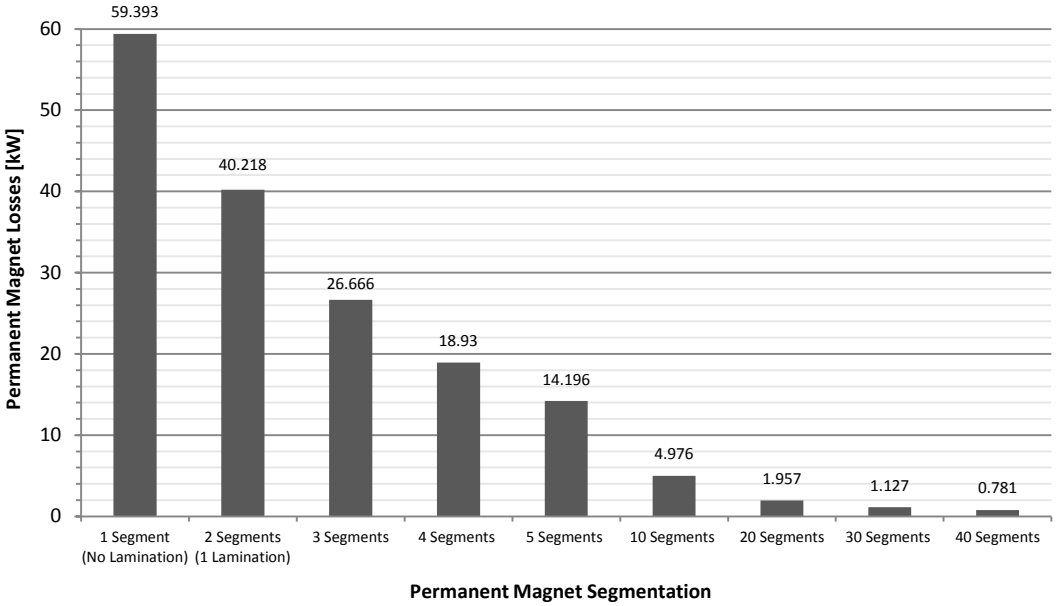

Figure 4-14 – Eddy-Current Loss in Permanent Magnets

4.5.1.2 Final Geometry

The geometry of the final AFPM motor is summarized in Table 4-2. The analysis results presented in the following refer to this proposed design.

Table 4-2 – Final AFPM Motor Geometry

Parameter	**Value**
Outer Diameter (D_{out})	510 mm
Inner Diameter (D_{in})	315 mm
Machine Length (l_{tot})	100 mm
Number of Pole Pairs (p)	5
Number of Stator Segments (N_s)	12
Air Gap Length (l_g)	1.5 mm
Permanent Magnet Length (l_{pm})	6 mm
Rotor Core (Back Iron) Length (l_{rc})	14.4 mm
Stator Shoe Length (l_{shoe})	6.5 mm
Stator Central Bar Length (l_{sc})	43.2 mm
Width of Stator Winding (w_w)	13 mm
Number of Turns in Stator Windings (N)	17
Number of Stator Conductors in Parallel	6
Diameter of Stator Conductors [9] (AWG-12) [72]	2.053 mm
Copper Fill Factor	60 %
Phase Resistance in Stator Windings [10]	5.2 mΩ
Weight of Active Components [11]	About 94 kg

4.5.1.3 Back EMF

The back EMF waveforms for the three-phase motor are computed without current excitation at rated speed (960 rpm). Figure 4-15 shows the back EMF for the three phases.

[9] AWG-12 wire diameter without insulation (bare copper)
[10] The phase resistance in the stator windings is calculated based on eqn. (101).
[11] Approximated weight of motor components: Rotor core: 14.24 kg, magnet: 0.54 kg, stator segment: 2.76 kg, coil: 1.83 kg

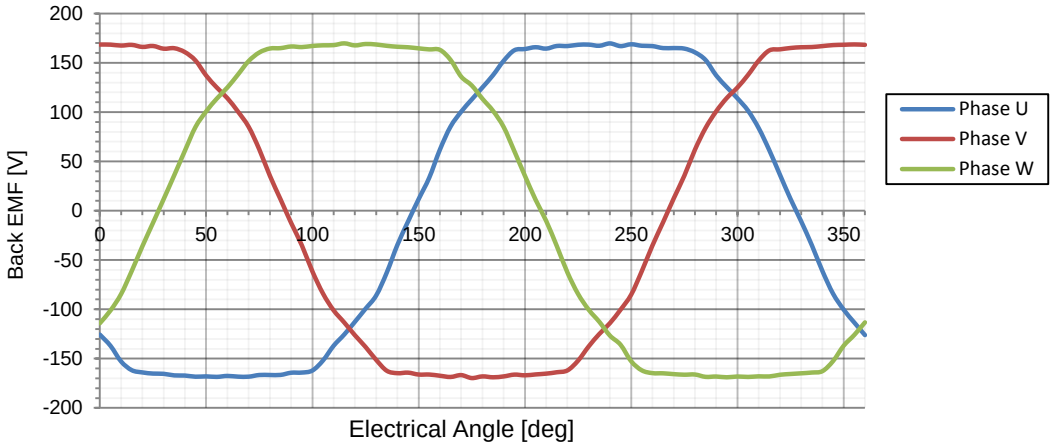

Figure 4-15 – Three-Phase Back EMF at Rated Speed (960 rpm)

4.5.1.4 Magnetic Flux Distribution

Figure 4-16 shows the magnetic flux distribution in the AFPM machine at rated speed when maximum current is applied. It is noticeable that the maximum magnetic flux density is available in the stator segments, in the stator shoes in particular. This is due to the flux traveling three-dimensional through the very small surface of the stator shoes creating a high flux density. The flux density contours in the stator shoes is shown in Figure 4-17. The flux path in stator and rotor is illustrated in Figure 4-18.

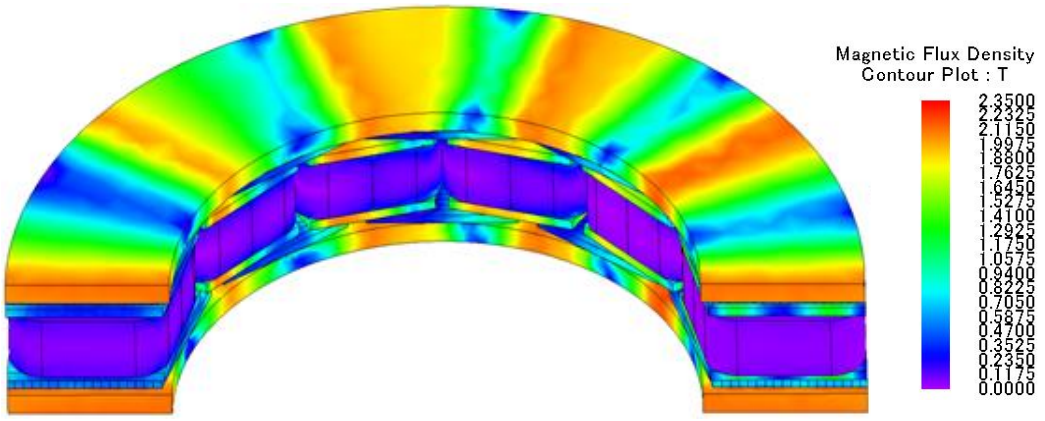

Figure 4-16 – Flux Density Distribution in AFPM Motor

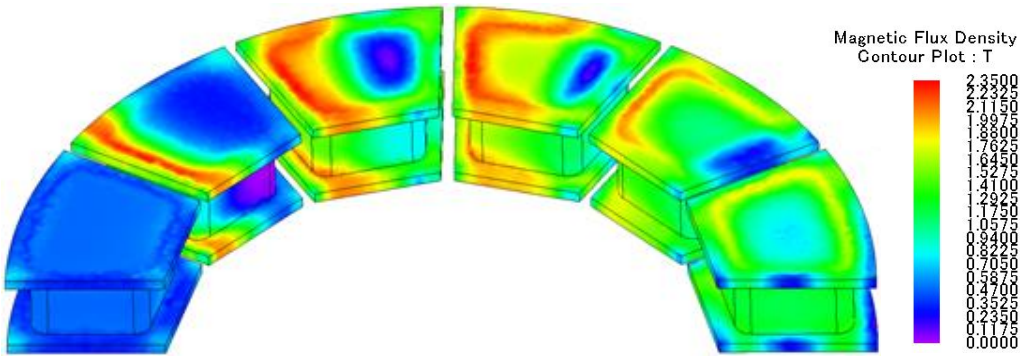

Figure 4-17 – Flux Density Distribution in Stator Teeth

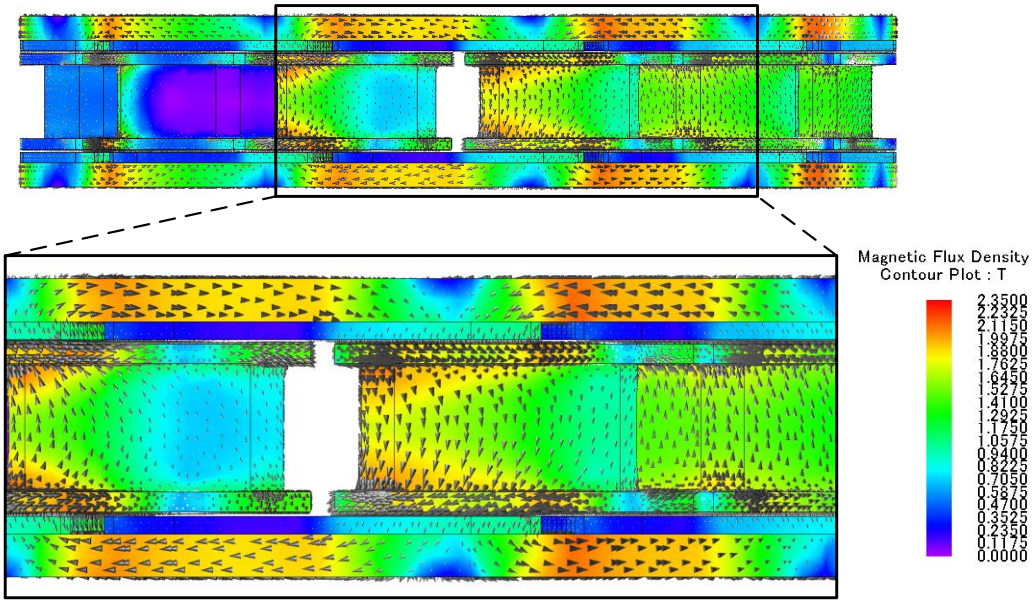

Figure 4-18 – Flux Path in Stator and Rotor

4.5.1.5 Torque Ripple

The maximum torque is achieved in the constant torque region at maximum current. The torque over two electrical revolutions (144 mechanical degrees) at rated speed when applying maximum current is visualized in Figure 4-19. The average torque becomes 1262.59 Nm. The range between the maximum

and minimum available torque (1299.6 Nm and 1232.41 Nm, respectively) indicates the torque ripple band. This gives a torque ripple of 5.32 %.

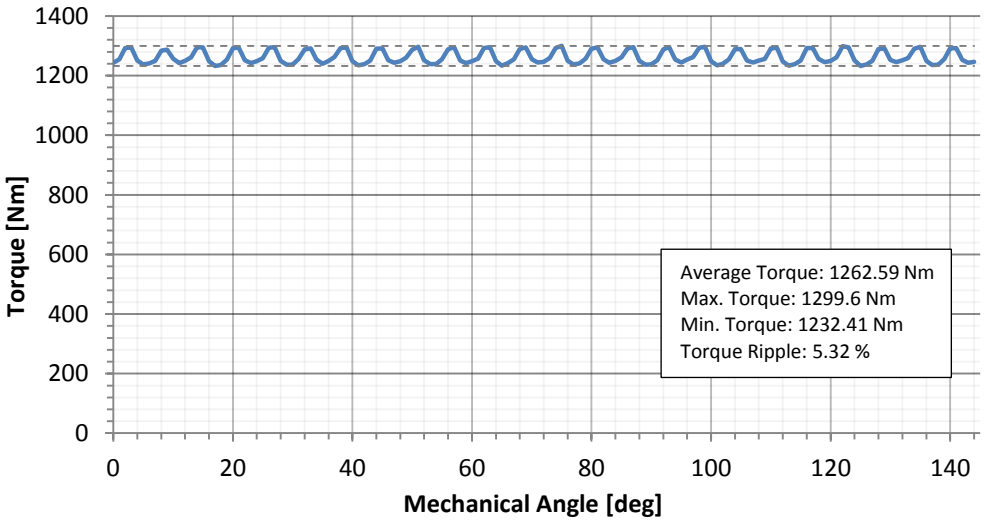

Figure 4-19 – Torque at Rated Speed and Maximum Current

4.5.1.6 Cogging Torque

Cogging torque can be computed when no excitation current is applied in the stator windings. It is dependent on the interaction between the rotor and the stator geometry. Cogging torque is caused by the magnet's tendency to align themselves in the minimum reluctance path [47]. One cogging torque revolution is shown in Figure 4-20. The peak value is 25.93 Nm which corresponds to 2.05 % of the average torque (Figure 4-20).

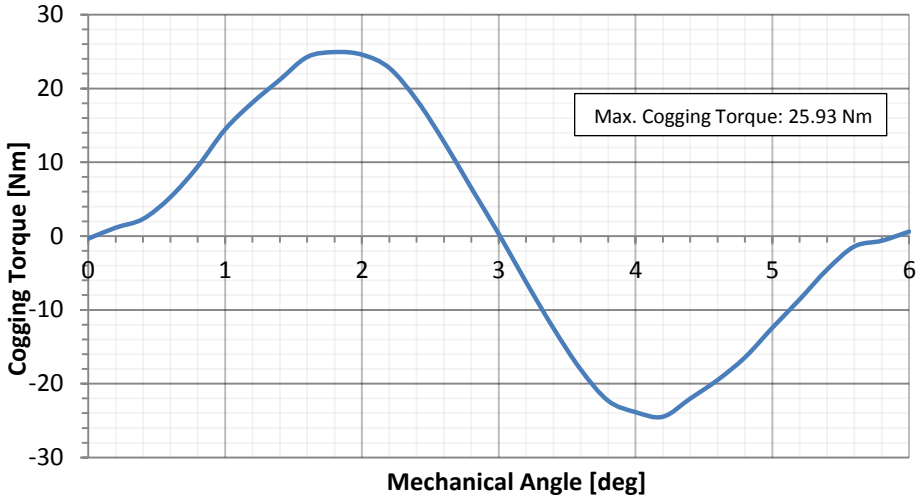

Figure 4-20 – Cogging Torque

4.5.1.7 Losses and Efficiency

The 3D FEA model is used to accurately calculate the motor losses. The copper losses in the stator windings increase when applying higher currents. A quadratic increase is expected in consideration of eqn. (99). Thus, the maximum copper loss occurs at maximum current of 318 A rms (450 A phase peak current). Due to the proportionality between current and torque the copper loss increases with rising torque in the constant torque region. However, this behavior does not apply in the field weakening region beyond the rated speed since the torque declines with increasing motor speed. Figure 4-21 visualizes the three-dimensional copper loss behavior for varying speed and torque.

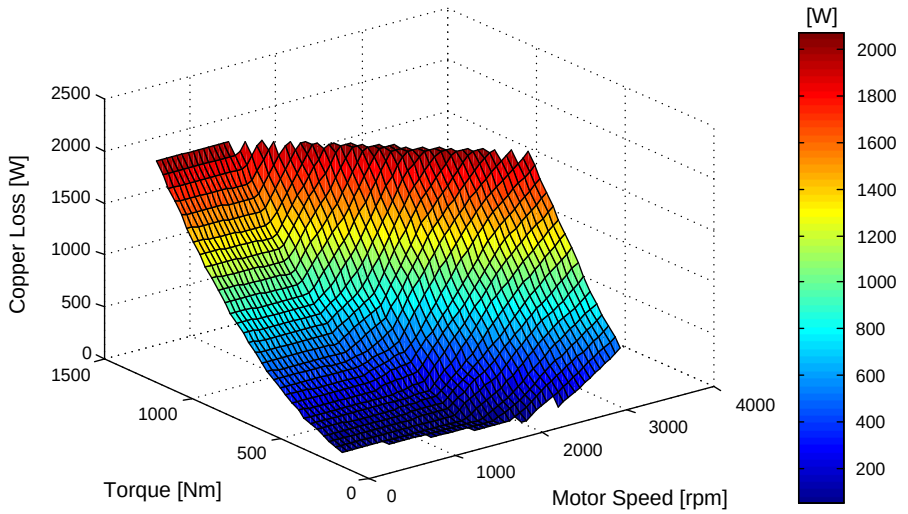

Figure 4-21 – Copper Losses

The iron losses in both stator and rotor and the eddy current losses in the magnets rise with increased speed. The maximum losses are available at maximum speed when maximum current is applied. The total iron losses (stator and rotor combined) and the PM losses are illustrated in Figure 4-22 and Figure 4-23, respectively.

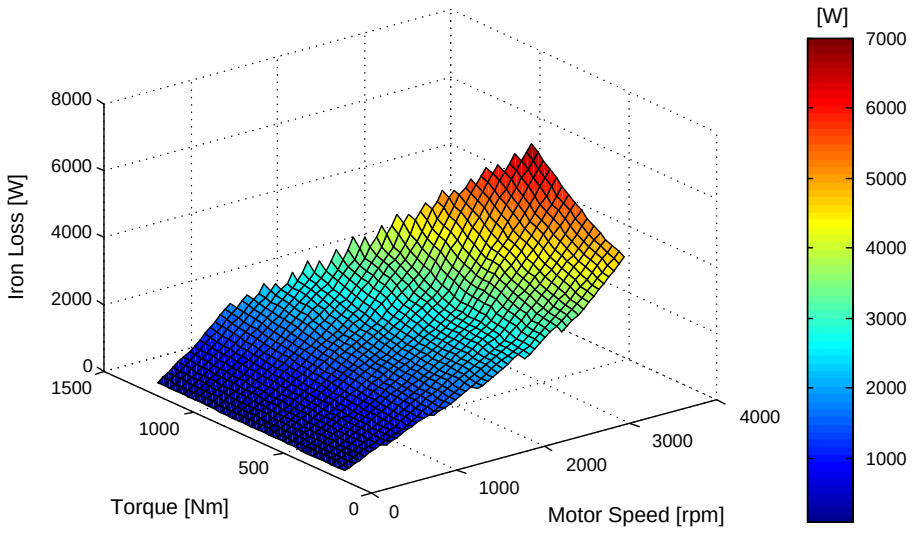

Figure 4-22 – Iron Losses

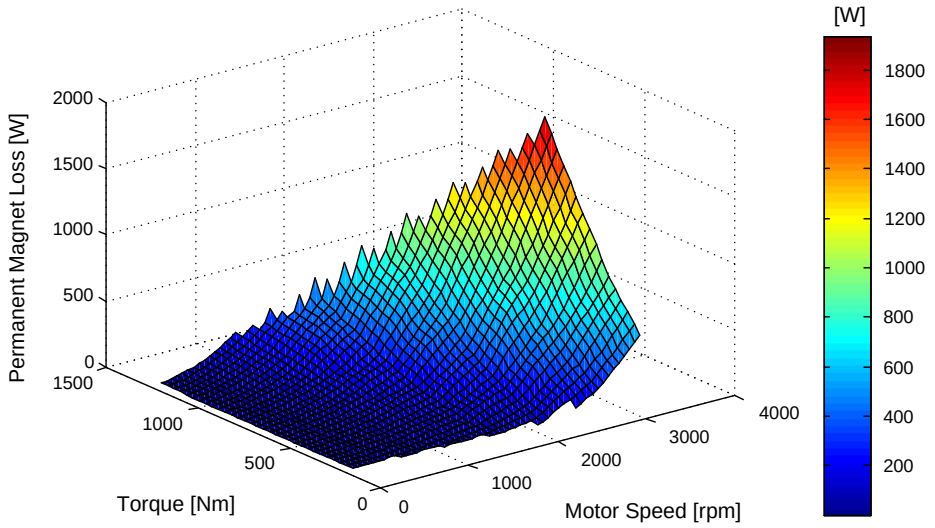

Figure 4-23 – Permanent Magnet Losses

The windage losses (rotational losses), generated by the interaction between the rotating rotor discs and the cooling fluid (air) are calculated based on eqn. (104). Contrary to the copper, iron and magnet losses, the windage losses are solely dependent on the motor speed. When increasing the rotational speed, the windage losses rise exponentially (Figure 4-24).

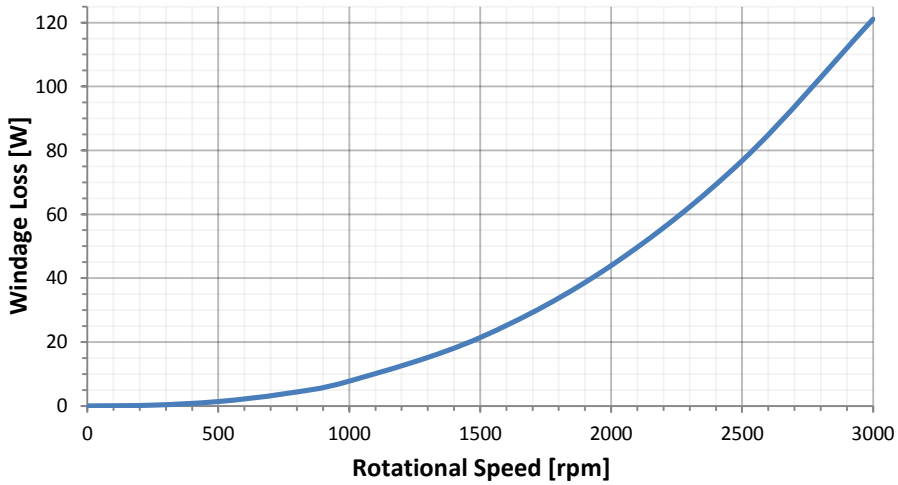

Figure 4-24 – Windage Losses vs. Motor Speed

All losses combined and their percentages in regard to the total losses at two different operation points are shown in Figure 4-25 and Table 4-3. It can be seen that the losses overall increase significantly with rising rotational speed. Furthermore, it is noticeable that the iron losses, particularly in the stator, have the greatest influence on the losses at high speeds. This is due to the high magnetic flux applied in the SMC stator segments. On the other hand, at rated speed the copper loss and iron loss are nearly equal.

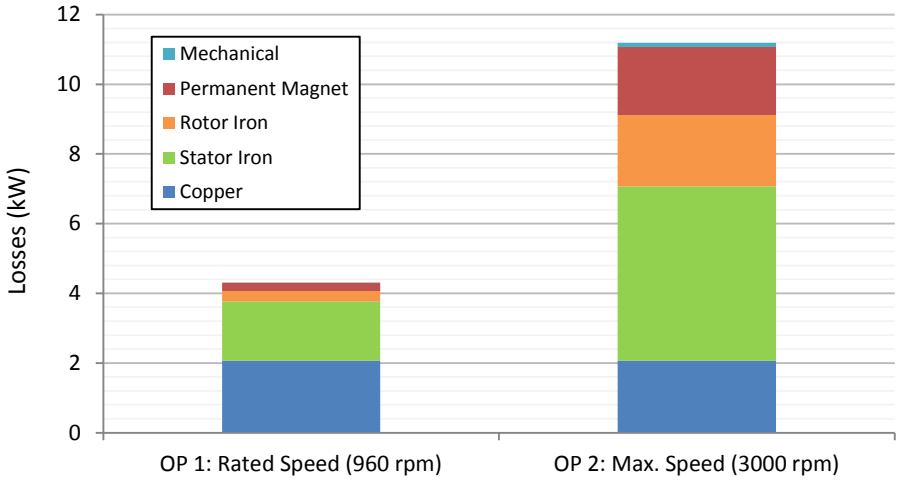

Figure 4-25 – Loss Distribution at Maximum Current

Table 4-3 – Loss Distribution

Loss Component	**Loss Distribution at Maximum Current**	
	Rated Speed (960 rpm)	Maximum Speed (3000 rpm)
Copper	48.12 % (2071.86 W)	18.51 % (2071.88 W)
Stator Iron	39.48 % (1699.93 W)	44.6 % (4991.45 W)
Rotor Iron	6.67 % (287.34 W)	18.31 % (2049.48 W)
Permanent Magnet	5.57 % (239.85 W)	17.49 % (1957.23 W)
Mechanical	0.16 % (7.01 W)	1.08 % (121.08 W)
Total	100 % (4.306 kW)	100 % (11.191 kW)

However, this comparison shows only two operation points, i.e. two different speeds at maximum current. When lowering the applied current the copper losses would decrease which would change the loss distribution.

The motor efficiency is calculated from the sum of all generated losses. The torque-speed map with efficiency contours is shown in Figure 4-26. The peak efficiency of the AFPM machine is 97 % which is higher than the targeted value (95 %). It can be seen that the motor efficiency is very high at speeds between about 400 and 2000 rpm. It was found that the highest efficiency occurs at around 1000 rpm at torque values between 700 Nm and 1000 Nm. At rated speed at maximum current the efficiency is 96.7 %. The efficiency decreases with rising speed in the field weakening area which is mainly caused by high iron losses and magnet losses.

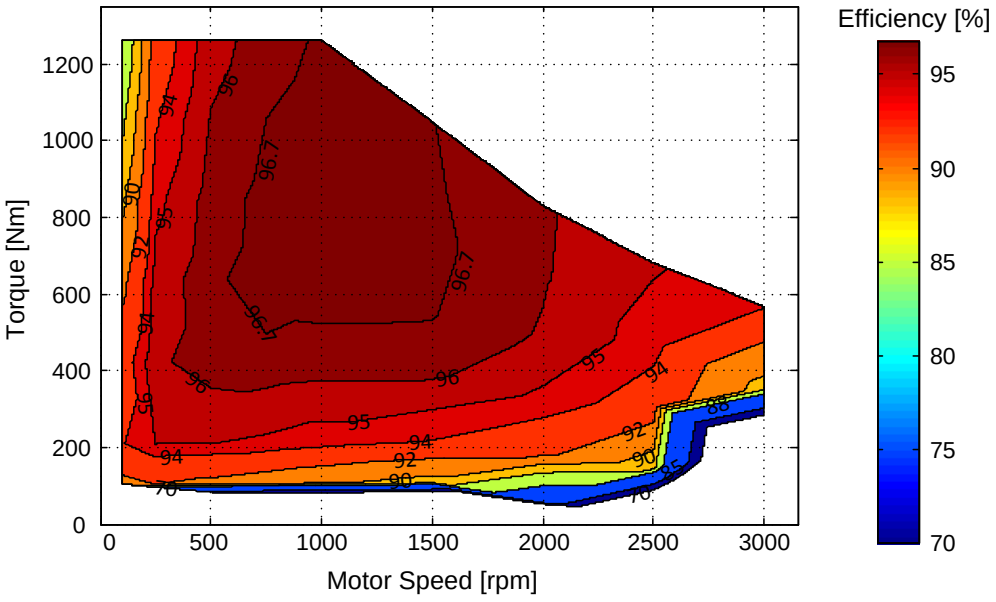

Figure 4-26 – Efficiency Map

The distribution of the efficiency levels is very suitable for the targeted application since the drive cycle analysis results showed that the electric taxiing system operates more frequently at speeds below 2000 rpm rather than at higher speeds. The required motor would be operating with high rotational speeds of up to 3000 rpm only during very demanding taxiing maneuvers with high on-ground velocities. The high speed region beyond 2000 or 2500 rpm would be solely used for very demanding taxiing maneuvers with high on-ground velocities. It is expected that the AFPM motor for the electric propulsion system would mostly operate in the more efficient area. It can also be seen that the constant motor efficiency of 92 % assumed for the electric taxiing system (Table 2-10) was a conservative assumption.

4.5.1.8 Summary Motor Characteristics

The characteristics of the final motor are summarized in Table 4-4. The designed AFPM machine fulfills the defined performance requirements while providing a high peak efficiency. The peak torque and peak power output values with 1262.59 Nm and 126.93 kW, respectively, are even higher than required for the electric taxiing system (see also Table 2-8).

Table 4-4 – AFPM Motor Characteristics

Parameter	**Value**
Peak Torque	1262.59 Nm
Peak Power	126.93 kW
Maximum Speed	3000 rpm
Rated Speed	960 rpm
Peak Efficiency	97 %
Torque Ripple (at Rated Speed)	5.32 %
Maximum Phase Peak Voltage	311 V
Maximum Current	450 A (318 A rms)

4.5.2 Discussion

4.5.2.1 Material Selection

In the proposed design powdered iron steel was used for the stator core due to the complicated geometry and the three-dimensional flux path in the stator. By doing that, the active area of the air gap was maximized. However, as described in section 4.3.3, SMC suffers from lower permeability than laminated steel leading to lower torque density capabilities. In general, laminated steel provides a wider linear region before it reaches its non-linear region and ultimately the saturation limit. Hence, an alternative to the use of SMC for the stator core could be using steel laminations, which was done in [64] and [73]. By simplifying the stator segment geometry a machine with laminated steel in the stator could be designed. This might allow an increase of the motor torque capabilities and a decrease of the iron losses, as well as reduced cost since steel laminations are less expensive than SMC material [64], [73].

The AFPM motor could also be improved by using SMC with higher magnetic loading capabilities. The material chosen in this thesis, Somaloy 550, is only a baseline material of the company Höganäs. This one was selected due to the lacking of access to B-H curves and loss characteristics of superior SMC materials. More recent materials such as Somaloy 700 or Somaloy 1000, offering higher strength and higher permeability or lower losses respectively, could be used for future designs which would improve the machine performance [65]. Similarly, the steel laminations in the rotor core could be replaced by superior laminated steel, i.e. with better B-H characteristics than 50JN400, to increase the magnetic loading of the machine, resulting in a higher torque density, or decrease the machine weight, respectively.

4.5.2.2 Copper Fill Factor

For the selected design a copper fill factor of 60 % was assumed. This is a conservative assumption that can be optimized if possible. Fill factors of up to 78 % have been presented in [52] and [71]. By increasing the fill factor the machine size can be reduced significantly. This might be an important step in optimizing the designed AFPM machine since the highest possible torque density is desired for a motor that is implemented into the wheel of an aircraft. As an example, increasing the copper fill factor from 60 % to 70 % would enable a decrease of the total active machine length by 6 % (from 100 mm to 94 mm).

4.5.2.3 Motor Efficiency

The efficiency of the motor is computed based on the presented losses. Considered are copper losses, magnet losses, iron losses and windage losses. As the mechanical design is out of scope of this thesis, the friction losses in the bearings are not included in the analysis since the location and size of the bearings are not specified. However, these losses are expected to be relatively low. Moreover, the windage losses are calculated analytically for an air-cooled rotor design, although the required cooling mechanism in the rotor is not designed in this work. These assumptions need to be considered when comparing the proposed design with other electric machines.

4.5.2.4 Performance Requirements

The proposed electric taxiing system was sized to achieve a similar on-ground performance as conventional taxiing, leading to very demanding motor requirements, in particular high torque characteristics. If wanted, the system could be downsized to match less demanding taxiing drive cycles only. This would result in a limited taxiing performance, but the motor requirements could be reduced significantly. The result would be a less challenging AFPM motor design. However, it has to be considered that a limited taxiing performance would cause

longer on-ground operation times within the LTO cycle. Since the aim in this thesis was to achieve a similar driving performance as conventional taxiing to reduce taxiing times, the electric propulsion system and thereby the AFPM motor were sized to match the majority of the available drive cycles.

4.5.2.5 Planetary Gearbox and Clutch Mechanism

The proposed motor design is based on the assumption that a planetary gearbox with the chosen gear ratio fits inside the AFPM motor. Besides, the final electric taxiing design requires an additional clutch mechanism for high-speed operations during takeoff and touchdown as described in section 2.3.5.7. This clutch mechanism can potentially be integrated into the planetary gearbox similar to a solution presented by the German Aerospace Center in [22].

4.5.2.6 Limitations of Electric Taxiing System

As described in section 1.2.2, using an electric taxiing system is not beneficial for every flight operation since the extra mass added to the aircraft increases the fuel consumption while flying. In this work, a short haul aircraft has been selected since the taxiing phase covers a large percentage of the overall flight mission, elevating the benefits of an on-board electric taxiing system. Further limitations of electric taxiing systems such as the one presented in this thesis are discussed in [36].

5 CONCLUSIONS AND FUTURE WORK

5.1 Conclusions

In this thesis, the requirements for an electric taxiing system have been investigated. Self-recorded real-life taxiing drive cycles, including takeoff and landing cycles, have been used to analyse conventional on-ground movements of state-of-the art commercial aircrafts.

An electric powertrain concept has been developed to increase the conventional taxiing process in terms of operation cost, time and environmental pollution. Based upon the system requirements analysis the powertrain components have been sized and evaluated with a self-developed simulation model that allows testing the powertrain with the different drive cycles to ensure a similar driving behavior to conventional taxiing. The simulation results confirmed the assumptions, made for the powertrain sizing, in particular the electric motor characteristics.

Based on the determined system requirements, an axial flux permanent magnet (AFPM) machine with yokeless and segmented armature has been selected and designed to meet the very demanding combination of required motor specifications. The electromagnetic design and analysis process has been carried out by using analytical models and three-dimensional finite element analysis (3D FEA) in which it was mainly focused on 3D FEA. Here, the limiting factors have been the saturation limits of the chosen core materials and the assumed current density in the stator windings.

The results have shown that the SMC material used to compensate the three-dimensional flux path in the stator segments performs well. Laminations in the permanent magnets have been implemented to reduce the high eddy current losses generated in the magnet material, resulting in a good motor performance with a peak efficiency of 97 %.

Torque ripple (5.32 % at rated speed and maximum current) and cogging torque (2.05 %) have been calculated using the 3D FEA model. An evaluation of the torque-speed characteristics has shown that the proposed AFPM motor design providing 127 kW peak power, 1262.6 Nm peak torque and 3000 rpm maximum speed was successful since it fulfills the given performance requirements.

5.2 Future Work

If necessary, the performance of the AFPM motor could be further increased by optimizing the motor geometry with varying parameters such as stator segment, winding, air gap and permanent magnet dimensions. In particular, the shape of the stator segments can be improved since the selected shapes of the stator shoes and central bar were selected on the basis of existing designs of AFPM machines with a similar topology and due to simplicity in the 3D FEA model. More rounded contours might allow reducing the flux density which is caused by the three-dimensional magnetic flux traveling through small cross-sectional areas in the stator shoes. Furthermore, superior materials for stator segments, rotor core and magnets could be evaluated as described in section 4.5.2.1.

To reduce the rotor losses, PM laminations have been implemented to cut the eddy currents generated in the magnets. As described in 4.5.1.1, an insulation condition has been used in the FEA model to represent the electrical insulation between the PM segments. Since the selected insulation condition assumes no interference of the eddy currents between the segments, potential deviations from the calculated magnet losses can be expected in reality. Thus, it could be of interest to further analyse the eddy currents in the magnets. Besides, the shape of the magnet segments could be improved to simplify the manufacturing process.

The scope of this thesis was the electromagnetic design of the AFPM machine rather than a mechanical design. A detailed mechanical analysis is recommended to evaluate the structural rigidity of the motor components and the toughness of the entire assembly. Furthermore, the motor housing could be designed ensuring the coupling to the wheel assembly in the undercarriage of the aircraft.

A potential cooling strategy has not been addressed in this study. Thus, it is also recommended to investigate the thermal behavior of the machine. Although the total losses have been significantly decreased by implementing PM segmentation and steel laminations in the rotors, a detailed thermal analysis is required to evaluate the heat generation, followed by the design of an appropriate cooling mechanism to realize the needed heat dissipation.

Another limit that has been analysed only marginal in this thesis is the fabrication of the motor. This could be of interest, in particular regarding the stator segments made out of SMC material and the permanent magnets. Since the PM lamination for the proposed design includes a complex segmentation of the magnets, the manufacturing of those needs to be analysed or even tested to ensure the practicability of the proposed machine.

Finally, a prototype of the AFPM motor for the electric taxiing system could be built and evaluated on a test bench to assess the performance achieved in reality, and ultimately be implemented into the wheel of an aircraft.

REFERENCES

[1] O. Grigore-Muler and M. Barbelian, "Regenerative braking for aircraft landing roll phase using an electric machine," in *13th International Conference on Optimization of Electrical and Electronic Equipment (OPTIM)* , Brasov, 2012 .

[2] B. Sarlioglu and C. T. Morris, "More Electric Aircraft – Review, Challenges and Opportunities for Commercial Transport Aircraft," *IEEE Transactions on Transportation Electrification,* vol. 1, no. 1, pp. 54-64, 2015.

[3] F. Re, "Assessing Environmental Benefits of Electric Aircraft Taxiing through Object-Oriented Simulation," *SAE International Journal Journal of Aerosace,* pp. 503-512, 2012.

[4] A. Tenconi and P. W. Wheeler, "Introduction to the Special Section on The More Electric Aircraft: Power Electronics, Machines, and Drives," *IEEE Transactions on Industrial Electronics,* vol. 59, no. 9, pp. 3521-3522, Sept 2012.

[5] A. Emadi, Advanced Electric Drive Vehicles, CRC Press, 2014.

[6] B. Bilgin and A. Emadi, "Electric Motors in Electrified Transportation: A step toward achieving a sustainable and highly efficient transportation system," *IEEE Power Electronics Magazine,* vol. 1, no. 2, pp. 10-17, 2014.

[7] B. Bilgin, P. Magne, P. Malysz, Y. Yang, V. Pantelic, M. Preindl, A. Karobkine, W. Jiang, M. Lawford and A. Emadi, "Making the Case for Electrified Transportation," *IEEE Transaction on Transportation Electrification,* vol. 1, no. 1, pp. 4-17, 2015.

[8] International Civil Aviation Organization, "ICAO Environment Report 2010," Environmental Branch of the International Civil Aviation Organization (ICAO), 2010.

[9] X. Roboam, B. Sareni and A. Andrade, "More Electricity in the Air: Toward Optimized Electrical Networks Embedded in More-Electrical Aircraft," *IEEE Industrial Electronics Magazine,* vol. 6, no. 4, pp. 6-17, 2012.

[10] W. Cao, B. C. Mecrov, G. J. Atkinson, J. W. Bennett and D. J. Atkinson, "Overview of Electric Motor Technologies Used for More Electric Aircraft (MEA)," *IEEE Transactions on Industrial Electronics,* vol. 59, no. 9, pp. 3523-3531, 2012.

[11] F. Re, "Viability and State of the Art of Environmentally Friendly Aircraft Taxiing Systems," in *Electrical Systems for Aircraft, Railway and Ship Propulsion (ESARS)*, 2012.

[12] M. Heinrich, F. Kelch, P. Magne and A. Emadi, "Investigation of Regenerative Braking on the Energy Consumption of an Electric Taxiing System for a Single Aisle Midsize Aircraft," in *IECON 2014 - 40th Annual Conference of the IEEE Industrial Electronics Society*, Dallas, TX , 2014.

[13] EGTS International, "EGTS Environmental Benefits (Overview)," Safran S.A. and Honeywell Aerospace, 2014.

[14] TaxiBot, "TaxiBot Product Homepage," TaxiBot, 2013. [Online]. Available: http://www.taxibot-international.com/. [Accessed 05 2015].

[15] Lufthansa Technik AG, "Innovative TaxiBot now used in real flight operations (press release)," Lufthansa Technik AG, 20 02 2015. [Online]. Available: http://www.lufthansa-technik.com/. [Accessed 05 2015].

[16] Lufthansa LEOS, "Lufthansa LEOS," [Online]. Available: http://www.lufthansa-leos.com/taxibot-downloads. [Accessed 15 06 2015].

[17] Lufthansa Technik AG, "Lufthansa LEOS signs development contract for eSchlepper - Trend-setting electromobility concept presented," Lufthansa AG, [Online]. Available: http://www.lufthansa-technik.com. [Accessed 06 2015].

[18] Airbus, "The Future by Airbus - Smarter Skies - Low Emission Ground Operations," Airbus S.A.S., 2015. [Online]. Available: http://www.airbus.com/innovation/future-by-airbus/smarter-skies/low-emission-ground-operations/. [Accessed 06 2015].

[19] WheelTug plc, "WheelTug Homepage," WheelTug plc, 2014. [Online]. Available: http://www.wheeltug.gi/. [Accessed May 2015].

[20] Delos Aerospace, "Delos Aerospace, L.L.C. Announces Technology to Reduce Aircraft Fuel Burn Reducing Greenhouse Gas Production and Increase Airport and Aircraft Capacity Utilization," Delos Aerospace L.L.C., 2007. [Online]. Available: http://delosaerospace.com/Press_Room.html. [Accessed 06 2015].

[21] Delos Aerospace, "Delos Aerospace Homepage," Delos Aerospace, L.L.C., 2011. [Online]. Available: http://delosaerospace.com/. [Accessed May 2015].

[22] M. Schier, F. Rinderknecht and H. Hellstern, "Electric Wheel Hub Motor for Aircraft Application," *International Journal Of Renewable Energy Research (IJRER),* vol. 1, pp. 298-305, 2011.

[23] DLR, "DLR Airbus A320 ATRA taxis using fuel cell-powered nose wheel for the first time," German Aerospace Center DLR, 12 07 2011. [Online]. [Accessed 06 2015].

[24] T. Raminosoa, T. Hamiti, M. Galea and C. Gerada, "Feasibility and Electromagnetic Design of Direct Drive Wheel Actuator for Green Taxiing," in *IEEE Energy Conversion Congress and Exposition (ECCE)*, Phoenix, AZ, 2011.

[25] Z. Xu, C. Tighe, M. Galea, T. Hamiti, C. Gerada and a. S. J., "Thermal design of a permanent magnetic motor for direct drive wheel actuator," in *IEEE International Conference on Electrical Machines (ICEM)*, Berlin, 2014.

[26] Honeywell Aerospace and Safran/ Messier-Bugatti-Dowty, "Electric Green Taxiing System (EGTS) Homepage," Honeywell International Inc. and Safran S.A., [Online]. Available: http://www.greentaxiing.com/. [Accessed May 2015].

[27] EGTS International, "Electric Green Taxiing System, demonstration aircraft, EGTS International (Honeywell, Safran)," 2013, Paris Air Show. [Online]. Available: https://upload.wikimedia.org/wikipedia/commons/0/05/Safran_Honeywell_EGTS_Airbus_A320-212_F-HGNT_PAS_2013_01.jpg. [Accessed June 2015].

[28] Magnet Motor, "GreenTaxi," L-3 Magnet Motor, 2015. [Online]. Available: http://www.magnet-motor.de/. [Accessed 06 2015].

[29] WheelTug, "WheelTug - Driving Aerospace," WheelTug, 2014. [Online]. Available: http://www.wheeltug.com/. [Accessed 06 2015].

[30] International, EGTS (Honeywell Aerospace and Safran), "Electric Green Taxiing Systems," Honeywell and Safran, 2014. [Online]. Available: www.greentaxiing.com. [Accessed 19 02 2014].

[31] M. T. E. Heinrich, "On the Concept of Electric Taxiing for Midsize Aircraft: A Power System and Architecture Investigation," Master's Thesis, McMaster University, Hamilton, Canada, 2015.

[32] A. Teo, K. Rajashekara, J. Hill and B. Simmers, "Examination of Aircraft Electric Wheel Drive Taxiing Concept," in *Power Systems Conference*, SAE Technical Paper 2008-01-2860, Bellevue, WA, 2008.

[33] U.S. Drive, "Electrochemical Energy Storage Technical Team Roadmap," U.S. Department of Energy, June 2013. [Online]. Available: http://energy.gov/. [Accessed 06 2015].

[34] U.S. Drive, "Electrical and Electronics Technical Team Roadmap," U.S. Department of Energy, June 2013. [Online]. Available: http://energy.gov/. [Accessed June 2016].

[35] Airbus S.A.S., "Airbus - Leading Aircraft Manufacturer," 2015. [Online]. Available: http://www.airbus.com/. [Accessed 06 2015].

[36] M. Heinrich, F. Kelch, P. Magne and A. Emadi, "Regenerative Braking Capability Analysis of an

Electric Taxiing System for a Single Aisle Midsize Aircraft," *IEEE Transactions on Transportation Electrification (TTE)*, vol. PP, no. 99, p. 1, 2015.

[37] B. Hainline, B. Sellereite and K. and Swanke, "Powered Wheels - A Concept for Parking and Taxiing of Commercial Transport Airplanes," in *SAE Technical Paper 710446*, 1971.

[38] M. Ehsani, Y. Gao, S. E. Gay and A. Emadi, Modern Electric, Hybrid Electric, and Fuel Cell Vehicles - Fundamentals, Theory, and Design, CRC Press, 2005.

[39] A. A. Al roqi and W. Wang, "Torque of Rotating Device Prior an Airplane Landing," *International Journal of Engineering Research and General Science (IJERGS)*, vol. 2, no. 2, pp. 214-222, 2014.

[40] F. De Gernon, M. La Vecchia and A. Rigaldo, "Performance and Design of the Airbus A320 – Analysis of a Subsonic Aircraft," Department of Aerospace and Vehicle Engineering, Royal Institute of Technology, Stockholm, Sweden, 2009.

[41] Transport Canada - Air Navigation System Requirements Branch, "Aerodrome Standards and Recommended Practices - 4th Edition," March 1993. [Online]. Available: http://www.tc.gc.ca/. [Accessed June 2015].

[42] R. G. Budynas and J. K. Nisbett, Shigley's Mechanical Engineering Design, 8th Edition, McGraw-Hill, 2006.

[43] W. Steinhilper and B. Sauer, Konstruktionselemente des Machinenbaus 2- Grundlagen von Maschinenelementen für Antriebsaufgaben (in German), 5th Edition, Berlin Heidelberg: Springer-Verlag , 2005.

[44] The MathWorks, *Mathworks Version R2012b*, [Software], 2012.

[45] A. Emadi, Energy-Efficient Electric Motors: Selection and Applications, New York: Marcel Dekker, 2004.

[46] J. Gieras, R.-J. Wang and M. Kamper, Axial Flux Permanent Magnet Brushless Machines - 2nd Edition, Springer Science + Business Media B.V., 2008.

[47] S. Kahourzade, A. Mahmoudi, H. W. Pink and M. N. Uddin, "A Comprehensive Review of Axial-Flux Permanent-Magnet Machines," *Canadian Journal of Electrical and Computer Engineering*, vol. 37, no. 1, pp. 19-32, 2014.

[48] H. Vansompel, P. Sergeant, L. Dupre and A. Van den Bossche, "Evaluation of a Simple Lamination Stacking Method for the Teeth of an Axial Flux Permanent-Magnet Synchronous Machine With Concentrated Stator Windings," *IEEE Transactions on Magnetics*, vol. 48, no. 2, pp. 999-1002, 2012.

[49] T. Woolmer and M. McCulloch, "Analysis of the Yokeless And Segmented Armature Machine," *IEEE International Electric Machines & Drives Conference*, vol. 1, pp. 704-708, 2007.

[50] F. Capponi, G. De Donato, G. Rivellini and F. Caricchi, "Fractional-Slot Concentrated-Winding Axial-Flux Permanent-Magnet Machine With Tooth-Wound Coils," *IEEE Transactions on Industry Applications*, pp. 2446-2457, 2014.

[51] J. Wang, V. Patel and W. Wang, "Fractional-Slot Permanent Magnet Brushless Machines with Low Space Harmonic Contents," *IEEE Transactions on Magnetics*, vol. 50, no. 1, 2013.

[52] A. EL-Refaie, "Fractional-Slot Concentrated-Windings Synchronous Permanent Magnet Machines: Opportunities and Challenges," *IEEE Transactions on Industrial Electronics*, vol. 57, no. 1, pp. 107-121, 2009.

[53] A. A. AbdElhafez and A. J. Forsyth, "A Review of More-Electric Aircraft," in *13th International Conference on Aerospace Sciences & Aviation Technology*, Cairo, Egypt, 2009.

[54] Z. Yu, "Space-Vector PWM With TMS320C24x/F24x Using Hardware and Software Determined Switching Patterns," Texas Instruments, 1999.

[55] E. Fornasiero, L. Alberti, N. Bianchi and S. Bolognani, "Considerations on Selecting Fractional-Slot Nonoverlapped Coil Windings," *IEEE Transactions on Industry Applications*, vol. 49, no. 3, pp. 1316-1324, 2013.

[56] Z. Zhu, M. Mohd Jamil and L. Wu, "Influence of Slot and Pole Number Combinations on Unbalanced Magnetic Force in PM Machines With Diametrically Asymmetric Windings," *IEEE Transactions on Industry Applications*, vol. 49, no. 1, pp. 19-30, 2013.

[57] S. Jafari-Shiadeh and M. Ardebili, "Analysis and Comparison of Axial-Flux Permanent Magnet Brushless-DC Machines with Fractional-Slot Concentrated-Windings," in *Power Electronics, Drive Systems and Technologies Conference (PEDSTC)*, Tehran, 2013.

[58] D. Ishak, Z. Zhu and D. Howe, "Comparative study of permanent magnet brushless motors with all teeth and alternative teeth windings," in *Second International Conference on Power Electronics, Machines and Drives (PEMD 2004)*, Edinburgh, UK, 2004.

[59] Hanselman, Brushless Motors - Magnetic Design, Performance, and Control, E-Man Press LLC, 2012.

[60] J. Cros, P. Viarouge, Y. Chalifour and J. Figueroa, "A new structure of universal motor using soft magnetic composites," *IEEE Transactions on Industrial Applications*, vol. 40, no. 2, pp. 550-557, 2004.

[61] W. Tong, Mechanical Design of Electric Motors, Boca Raton: CRC Press - Taylor & Francis Group,

2014.

[62] C. Du-Bar, "Design of an axial flux machine for an in-wheel motor application," Master of Science Thesis, Chalmers University of Technology, Göteborg, Sweden, 2011.

[63] F. Marignetti, G. Tomassi, P. Cancelliere, V. Delli Colli, R. Di Stefano and M. Scarano, "Electromagnetic and Mechanical design of a Fractional-slot-windings Axial-flux PM synchronous machine with Soft Magnetic Compound Stator," in *Industry Applications Conference, 41st IAS Annual Meeting*, 2006.

[64] W. Fei and P. C. K. Luk, "An Improved Model for the Back-EMF and Cogging Torque Characteristics of a Novel Axial Flux Permanent Magnet Synchronous Machine With a Segmental Laminated Stator," *IEEE Transactions on Magnetics,* vol. 45, no. 10, pp. 4609-4612, 2009.

[65] Hoganas AB, "Hoganas," 2015. [Online]. Available: https://www.hoganas.com/. [Accessed April 2015].

[66] JSOL Corporation, *JMAG-Designer Version 13.1,* [Software], 2014.

[67] Y. Huang, T. Zhou, J. Dong, H. Lin, H. Yang and M. Cheng, "Magnetic Equivalent Circuit Modeling of Yokeless Axial Flux Permanent Magnet Machine With Segmented Armature," *IEEE Transactions on Magnetics,* vol. 50, no. 11, 2014.

[68] F. Marignetti, V. Delli Colli and S. Carbone, "Comparison of Axial Flux PM Synchronous Machines With Different Rotor Back Cores," *IEEE Transactions on Magnetics,* vol. 46, no. 2, pp. 598-601, 2010.

[69] S. M. A. Shark and M. T. N. Mohammad, "Axial Field Permanent Magnet DC Motor With Powder Iron Armature," *IEEE Transactions on Energy Conversion,* vol. 22, no. 3, pp. 608-613, 2007.

[70] A. Mahmoudi, S. Kahourzade, N. Rahim and W. Hew, "Design, Analysis, and Prototyping of an Axial-Flux Permanent Magnet Motor Based on Genetic Algorithm and Finite-Element Analysis," *IEEE Transactions on Magnetics*, vol. 49, no. 4, pp. 1479-1492, 2012.

[71] A. Jack, B. Mecrow, P. Dickinson, D. Stephenson, J. Burdess, N. Fawcett and J. Evans, "Permanent-Magnet Machines with Powdered Iron Cores and Prepressed Windings," *IEEE Transactions on Industry Applications,* vol. 36, no. 4, pp. 1077-1084, 2000.

[72] ASTM International, "ASTM B258 - 14 Standard Specification for Standard Nominal Diameters and Cross-Sectional Areas of AWG Sizes of Solid Round Wires Used as Electrical Conductors," West Conshohocken, 2014.

[73] W. Fei, P. Luk and K. Jinupun, "A new axial flux permanent magnet Segmented-Armature-Torus machine for in-wheel direct drive applications," in *IEEE Power Electronics Specialists Conference (PESC)*, Rhodes, 2008.

APPENDIX

Kinematic Drive Cycle Analysis – Further Results

Table A-1 – Kinematic Drive Cycle Analysis – Further Results – Taxi-Out Cycles

Parameter [Unit]	**Taxi-Out (Takeoff) Drive Cycles (Part 1)**				
	Berlin (a)	Berlin (b)	London (a)	London (b)	Frankfurt
Total Taxiing Distance [km]	2.29	1.987	3.41	4.125	2.07
Max. Velocity [km/h]	30.7	41.1	48.1	48.2	48.4
Max. Acceleration [m/s^2]	0.445	0.306	0.749	0.417	1.027
Max. Net Traction Force [kN]	40.61	27.93	68.33	38.03	93.69
Max. Gross Traction Force [kN]	48.73	35.99	76.4	46.13	101.78
Max. Net Traction Power [kW]	260.56	158.97	268.84	190.14	584.52
Max. Gross Traction Power [kW]	312.69	231.93	330.62	265.21	679.8
Parameter [Unit]	**Taxi-Out (Takeoff) Drive Cycles (Part 2)**				
	Dallas (a)	Dallas (b)	Toronto (a)	Toronto (b)	Hamilton
Total Taxiing Distance [km]	3.22	3.26	4.7	4.123	3.3
Max. Velocity [km/h]	38.2	61.8	27.5	32.3	53.6
Max. Acceleration [m/s^2]	0.83	0.417	0.805	0.445	1.14
Max. Net Traction Force [kN]	76.06	38.03	73.48	40.6	103.99
Max. Gross Traction Force [kN]	84.15	46.14	81.57	48.7	112.08
Max. Net Traction Power [kW]	335.9	227.12	325.56	196.23	493.98
Max. Gross Traction Power [kW]	371.61	358.3	364.01	242.84	532.43

Table A-2 – Kinematic Drive Cycle Analysis – Further Results – Taxi-In Cycles

Parameter [Unit]	**Taxi-In (Landing) Drive Cycles (Part 1)**				
	Munich	Frankfurt (a)	Frankfurt (b)	Berlin	London
Total Taxiing Distance [km]	2.97	5.52	4.137	0.49	1.38
Max. Velocity [km/h]	67.6	52.4	32.4	24.3	45.4
Max. Acceleration [m/s^2]	1.083	0.916	0.389	0.278	0.584
Max. Net Traction Force [kN]	98.84	83.6	35.46	25.35	53.28
Max. Gross Traction Force [kN]	106.9	91.7	43.55	33.44	61.34
Max. Net Traction Power [kW]	363.38	499.19	179.27	117.63	102.68
Max. Gross Traction Power [kW]	447.65	547.64	227.27	170.24	143.84
Parameter [Unit]	**Taxi-In (Landing) Drive Cycles (Part 2)**				
	Toronto	Dallas (a)	Dallas (b)	Vancouver	Calgary
Total Taxiing Distance [km]	2.56	1.81	2.89	2.27	2.39
Max. Velocity [km/h]	41.3	35.2	53.9	43.8	60.1
Max. Acceleration [m/s^2]	0.69	0.86	0.36	0.224	0.417
Max. Net Traction Force [kN]	63.38	78.44	33.1	20.4	38.03
Max. Gross Traction Force [kN]	71.46	86.53	41.31	28.55	46.13
Max. Net Traction Power [kW]	234.09	365.97	345.49	164.77	209.13
Max. Gross Traction Power [kW]	318.61	403.72	431.43	253.81	253.7